

A FATIGUE MODEL FOR SHAPE OPTIMIZATION BASED ON CONTINUUM DAMAGE MECHANICS

zur Erlangung des akademischen Grades eines
DOKTORS DER INGENIEURSWISSENSCHAFTEN
von der Fakultät für Maschinenbau der
Universität Karlsruhe

genehmigte
DISSERTATION
von

Dipl.-Phys. Jürgen E. Grunwald
aus Ettlingen/Baden

Tag der mündlichen Prüfung: 25.01.96

Hauptreferent: Prof. Dr.-Ing. E. Schnack
Korreferenten: Prof. Dr. rer. nat. M. Brokate
Prof. Dr. G. I. N. Rozvany, Ph.D.
Prof. Dr.-Ing. Wriggers

Abstract

Most engineering parts contain some changes in cross section or boreholes. There is a stress concentration at these points and the parts will probably fail there. Almost all machine parts are dynamically loaded. The most important failure mode is fatigue.

Fatigue is observed at load levels below the yield stress. On a macroscopic scale the structural behavior is elastic, but on a microscale plasticity is found at inclusions and other material weakness.

During fatigue lifetime, a stress redistribution is observed in the structure, due to the material deterioration. It is possible to model fatigue behavior accurately with a Continuum Damage Mechanics Model. The history of loading is taken into account and also the stress redistribution is modelled. On the basis of this modellization two new cost functions for shape optimization considering fatigue are determined.

The optimization results show a remarkably increased lifetime in comparison to a classical shape in calculation as well as in experiment. The difference to the statically optimized shape is small.

Acknowledgements:

The reported work was done during my employment as a research assistant at the Institute of Solid Mechanics at Karlsruhe University.

I would like to thank Professor Schnack not only for the opportunity to do this work but also for the encouragement to work with the Continuum Damage Mechanics Models.

It was very helpful for me to discuss the whole work also with the other reviewers Professor Brokate, Professor Rozvany and Professor Wriggers. Their remarks and their background informations really improved this work.

I also thank Professor Babuska and Professor Lemaitre for their interest and the encouraging discussions. Both of them left a deep impression on me.

Such a work is never the work of one single person. It was very interesting and a great pleasure for me to work with so many people from different countries with different thinking and backgrounds. Here I express my special thanks to my good friend Dr. Mohamed Fanni. I would like to thank all my other colleagues and “my” students for all the discussions. There is no way to knowledge - not only in science - without discussion.

I would like to express my special thanks to the persons of the workshop, especially the foreman, Mr. Mayer, and Mr. Stober. It was really interesting and helpful for me to collaborate with them.

Finally let me express my hope while leaving this institute also to have left a bit of my thinking, of my ideas and my ideals there.

Karlsruhe, July 1996

Jürgen Grunwald

L 'essentiel est invisible pour les yeux, répéta le petit prince, afin de se souvenir.

Antoine de Saint-Exupéry

Remarks to the Notation:

Scalars are written in normal font. Vectors and matrixes are written **bold face**. If tensor notation is used *Einsteins sum convention* is adopted, this means if a subscript appears twice, than the sum over this index is taken.

A comma as a subscript means partial differentiation.

The meaning of all other uncommon symbols is explained at the first appearance in the text.

Contents

1	Introduction	1
2	Fatigue	4
2.1	Phases of Fatigue Life	4
2.2	Main Features of Fatigue	7
2.2.1	History of Loadings	7
2.2.2	Three Dimensional Effects	9
2.2.3	Mean Stress	9
2.2.4	Frequency	10
2.2.5	Size Effect and Scattering	10
2.3	Engineering Lifetime Calculation	11
2.3.1	Lifetime Calculation in LCF and HCF	11

2.3.2	Damage Accumulation	13
2.4	Discussion	14
3	Static Shape Optimization Problem	15
3.1	Continuous Optimization Problem	15
3.1.1	Boundary Value Problem in Linear Elasticity	16
3.1.2	Nonlinear Optimization Problem	17
3.2	Discretized Static Shape Optimization Problem	22
3.2.1	Structure Analysis	22
3.2.2	Formulation of the Discretized Static Shape Optimization Problem	24
3.2.3	Optimizer	25
3.2.4	Constraints	29
3.3	Efficient Algorithms and Implementation	32
3.3.1	Sparse Storing and Iterative Solver	32
3.3.2	Design Variables	33
3.3.3	Sensitivity Analysis	37
4	Damage Mechanics	41

4.1	Introduction to Damage Mechanics	41
4.1.1	Introduction of a Damage Variable	42
4.1.2	Concept of Effective Stress	43
4.1.3	Strain Equivalence Principle	44
4.2	Thermodynamical Description	44
4.2.1	State Potential	45
4.2.2	Potential of Dissipation	48
4.2.3	Triaxiality and Damage Equivalent Stress	52
4.3	Modelling Fatigue	53
4.3.1	Two Scale Model	54
4.3.2	Damage Threshold and Critical Damage	56
4.3.3	Constitutive Equations	58
4.3.4	Numerical Procedure	58
4.4	Further Developments	64
4.4.1	Anisotropic Damage	64
4.4.2	Deterministic/Probabilistic Theory	66

5 Numerical Tools and Results	67
5.1 Simple Error Indicator	67
5.2 Substructuring and Mesh Refinement	69
5.2.1 Substructuring	70
5.2.2 Mesh Refinement	71
5.3 Successive Strategies	72
5.4 Numerical Example	72
5.5 Statically Optimized Shape	73
5.5.1 Numerical Results	73
5.5.2 Discussion	74
5.6 Damage Analysis	76
5.6.1 Testing the Algorithm	76
5.6.2 Comparison of Circularly Notched and Statically Optimized Part	78
5.6.3 Discussion	79
5.7 Dynamically Optimized Shape	80
5.7.1 Damage Optimization	82

5.7.2	Damage Equivalent Stress	83
5.7.3	Discussion	85
6	Experimental Investigations	88
6.1	Material Properties	88
6.1.1	Preparation of the Specimens	89
6.1.2	Material Constants	90
6.2	Photoelastic Experiments	91
6.2.1	Camera Synchronization	93
6.2.2	Discussion of the Results	94
6.3	Lifetime Tests	94
6.3.1	Comparison of Experimental and Numerical Results	95
6.3.2	Statistical Analysis of Results	95
6.3.3	Experimental Comparison of Different Shapes	96
7	Conclusion	99
A	Damage Mechanics	101

A.1	Proportional Loading	101
A.2	Fatigue Crack Growth	101
A.3	Failure in Micro-Mesoscale	103
B	Experimental Results in Detail	105
B.1	Tension Tests	106
B.2	Fatigue Tests	106
B.2.1	Damage Constants in VLCF	106
B.2.2	Fatigue Tests for Different Shapes	108
B.3	Photoelastic Pictures	110

Chapter 1

Introduction

In our times there is an increased sensitivity regarding resources and energy. More and more components are required not only to be functional but also to be a somewhat optimal solution (e.g. minimum of weight).

New management strategies such as Simultaneous Engineering take these demands into account. Design and calculation are no longer separated procedures. The calculation engineer nowadays is already involved in the design process. Therefore, he or she needs tools which help her/him not only in the design process of the whole part but also to get improvements of detail problems.

Almost any machine part includes places with changes in cross section, boreholes or notches. These places are always connected with a stress concentration which will determine the strength of the whole machine part. To optimize the more or less free boundary of these places will always improve the strength of the whole part, because the weakest link of the machine part will vanish.

Here, determination of this free boundary is called shape optimization (In [39] a more general definition including topology and parameter optimization is given). From a mathematical point of view the question of an optimally shaped structure is called an inverse problem. Instead of the calculation of the structural behavior for a given structure, given loads and supports, here the somewhat optimal shape of the structure itself is asked [28]. Shape optimization methods have been developed over the last 30 years [10, 12, 35, 40, 86] and the principal problems are solved. Present research work is the combination of shape optimization and topology optimization [11, 73, 77, 89], the other important branch of structural optimization. Now, first applications of shape and/or topology optimization are found in industry [7, 16, 28, 61, 78]. But nearly all the developed procedures are dealing with static optimization whereas almost any machine part is dynamically loaded. If dynamical loadings are considered the main interest is either in resonance [7, 29], or very simple engineering concepts are used [19, 62] to describe fatigue behavior.

In [30, 31] there is a first attempt of a systematical investigation of shape optimization for dynamical loadings. The following cases are taken into account: fatigue, multiaxial out-of-phase loadings and resonance fatigue.

Fatigue is modelled using different fatigue notch factor hypotheses (fatigue notch factor K_f : quotient of fatigue strength of smooth specimen and fatigue strength of notched specimen.)

In his conclusion *Fanni* found almost no difference between static optimization and K_f -optimization for all studied hypotheses. It was only in the case of the “weakest-link” model (statistical approach [15]) with a small statistical parameter (e.g. ceramics, with high scattering in the length of initially existing cracks), that not the static optimum was not achieved (FSD=fully stressed design: The von Mises stress is constant along the free boundary until the separation point is reached. See [86] and Fig. 1.1 and Fig. 1.2).

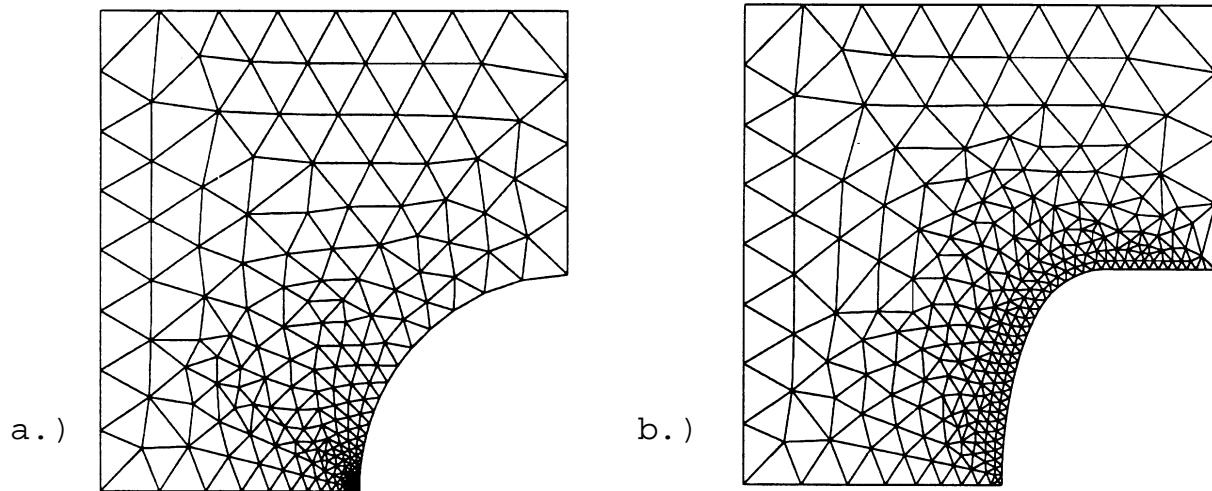


Figure 1.1: Static shape optimization of a notched tension bar. A quarter of the structure is discretized: a.) meshed start shape, b.) meshed optimized shape.

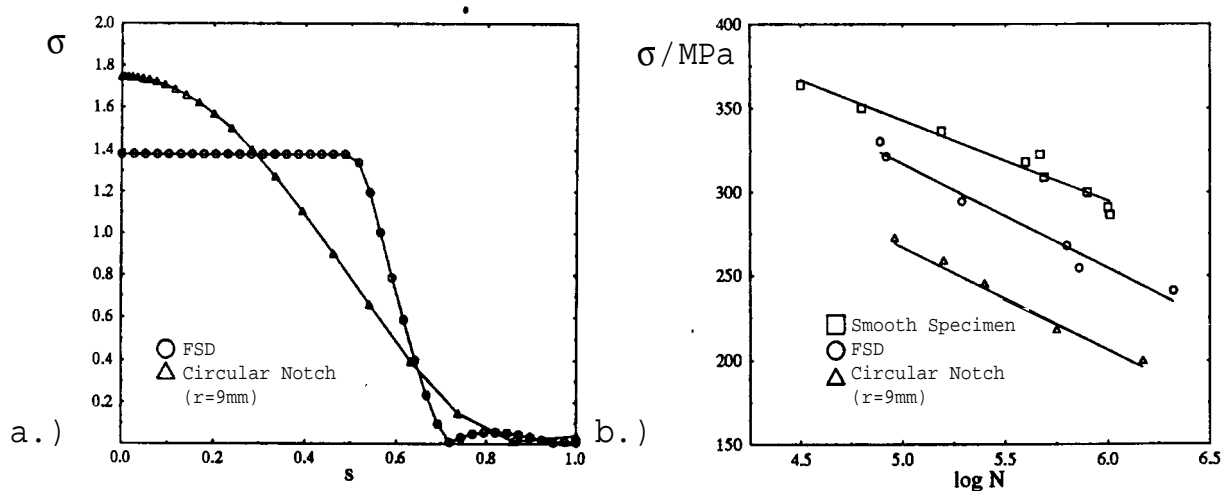


Figure 1.2: Static shape optimization of a notched tension bar. a.) Stress along the free boundary (σ : normalized von Mises stress), b.) experimental S-N-diagrams.

Two things must be pointed out:

- **Static Analysis**

The whole dynamic degeneration process is analyzed for fatigue in [30, 31] by just one single static FE-calculation. In Chapter 6 we will see that there is a stress redistribution due to damage accumulation during the fatigue process which is not mentioned in this modellization.

- **Experimental Results**

The experimental results (See Fig. 1.2) show a remarkably increased lifetime if a part with statically optimized shape is used instead of the circularly notched part. They are encouraging for further studies.

The aim of this work is to analyze the fatigue behavior, which is the most important and also the most dangerous failure mode in dynamical load cases, more carefully and to present an adequate optimization procedure. In conclusion the results of this procedure will be compared with the static optimization results.

After these introductory words in the first chapter, in the second chapter the main microscopic mechanisms and the main features of fatigue are described briefly, and the engineering procedure of lifetime calculation in LCF and HCF is summarized.

In Chapter 3, at first the continuous optimization problem is formulated and the procedure for the numerical solution of the discretized problem for a static load case is described. This is the basis for the “dynamical” optimization procedure.

In Chapter 4, a short introduction to Continuum Damage Mechanics (CDM) is given and a two scale model to characterize fatigue behavior within this CDM concept is described. The numerical damage analysis is very CPU-time intensive.

Therefore, in Chapter 5, at first some tools to save CPU-time and to get accurate results are introduced. In the second part of the chapter, damage evolution is studied for different shapes. In the end of the chapter, a dynamical optimization based on this CDM approach will be discussed.

In Chapter 6, the fatigue behavior is examined experimentally. Some concluding remarks are found in Chapter 7.

Chapter 2

Fatigue

Fatigue is the most important failure mode in material deterioration of dynamically loaded machine parts. Fatigue occurs at stress levels beyond the yield stress. This means, a part will probably fail under cyclic loading at a stress level which causes no remarkable damage in a single static load case.

Depending on the applied load level the following classification is often used:

- Very Low Cycle Fatigue (VLCF): $\frac{\Delta\varepsilon_p}{\Delta\varepsilon_e} \simeq 10..100$,
- Low Cycle Fatigue (LCF): $\frac{\Delta\varepsilon_p}{\Delta\varepsilon_e} \simeq 1..10$ and
- High Cycle Fatigue (HCF): $\frac{\Delta\varepsilon_p}{\Delta\varepsilon_e} \simeq 0$.

2.1 Phases of Fatigue Life

Fatigue life of dynamically loaded metallic parts can be divided into three sections:

- Crack initiation,
- Crack propagation,
 - State I,

- State II and
- Fracture residual.

The following short description of fatigue micromechanics is based on the work of [59, 60, 65].

At first, plastic deformations at a microlevel take place in the whole loaded structure. The amount and the number of grains containing these so-called fatigue slip bands increases with lifetime.

At first the dislocations are randomly distributed, this is called a debris structure. Later, depending on the crystal symmetry and the stacking fault energy (γ), different dislocation structures are built up.

Areas of high dislocation concentration are surrounded by areas of low dislocation concentration. In areas with high concentration, the dislocations interact and the possibility of slipping is reduced. Therefore, the plastic strain level at constant load decreases.

Normally, fatigue cracks occur at the surface of the parts. But in places of material inhomogeneities, e.g. cavities, large inclusions or in the case of surface hardening, crack initiation is also observed inside the part.

If there are no initial surface defects, microcracking is mostly observed in the fatigue slip bands. These slip bands form extrusion-intrusion pairs with high stress concentration at the surface of the part. These extrusion-intrusion pairs will appear at the same place, if the part is polished and loaded once more. Therefore, they are called persistent slip bands (PSB).

Often a lot of these microcracks appear, but only some are dominant and responsible for final failure.

State I crack propagation means the propagation of microcracks which may initially exist or which are built up in the crack initiation phase. Crack propagation of these microcracks is shear stress controlled. It will only occur in crystals with slip bands parallel to the highest shear stress (see Fig. 2.1). After the microcrack has grown over some crystals, state II of the crack propagation takes place.

State II crack propagation is connected with the propagation of the macroscopic crack ($l_0 = 0.1 \Leftrightarrow 1mm$).

The crack is following a path perpendicular to the applied load. To describe the velocity of macrocrack propagation is the task of Linear Elastic Fracture Mechanics (LEFM). The

simplest approach is achieved by *Paris* law:

$$\frac{da}{dN} = C\Delta K^m, \quad (2.1)$$

where

C , m : are material constants and K : is the stress intensity factor.

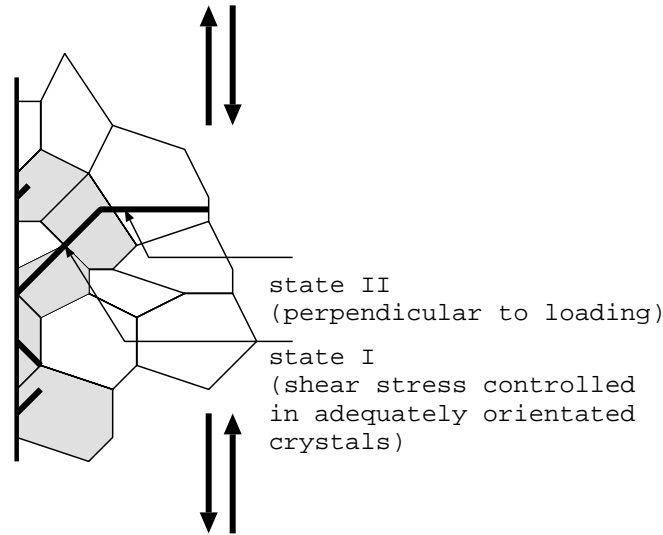


Figure 2.1: Schematic representation of state I and II crack propagation.

For medium crack propagation velocities ($10^{-5} \Leftrightarrow 10^{-3} mm/cycle$) the fractured surface often contains striations. The cleavage between them can be measured by an electron micrograph. This gives the movement of the crack-tip cycle by cycle.

The crack grows in this way until it reaches a critical size and becomes unstable.

Some people try to take the concepts of LEFM and to model with these concepts the growth of the microcracks (see e.g. [46]) in a probabilistic way. This procedure can become valuable particularly for materials with initial microcracks.

It is difficult to give practical criteria to distinguish the crack initiation phase and the crack propagation phase. So, it is usual to define the crack propagation phase just by the second state and to add the first state to the crack initiation phase.

With this classification more than 90% of the lifetime is in the crack initiation phase, especially for not too sharply notched parts with polished surfaces. Nevertheless, first microscopic cracks can be found after 0.1 % of the lifetime [88].

Therefore, we will focus our attention in this work on the maximization of the crack initiation phase.

An important difference of crack propagation under static and dynamical loadings are crack closure effects in the phase of compression. Their influence is known, but not completely understood until now [88].

2.2 Main Features of Fatigue

In the last section fatigue behavior was described on a microscopic scale. In this section the resulting macroscopic behavior is discussed.

2.2.1 History of Loadings

All factors influencing the lifetime can vary during fatigue life. As an example, the influence of changing the load level will be discussed below. Besides this, the material behavior - even if all influencing factors are constant - often changes during lifetime.

Effect of Strengthening and Softening

Depending on the heat treatment of the material, the microscopic mechanisms described in Section 2.1 lead to a strengthening and/or softening of the material during lifetime. In Fig. 2.2, in a normalized specimen at first a dislocation structure is built up, this is accompanied by softening. Then, there is an interaction between the highly concentrated dislocations accompanied by a strengthening of the material. For cold worked specimens, these effects of softening and strengthening are almost missing.

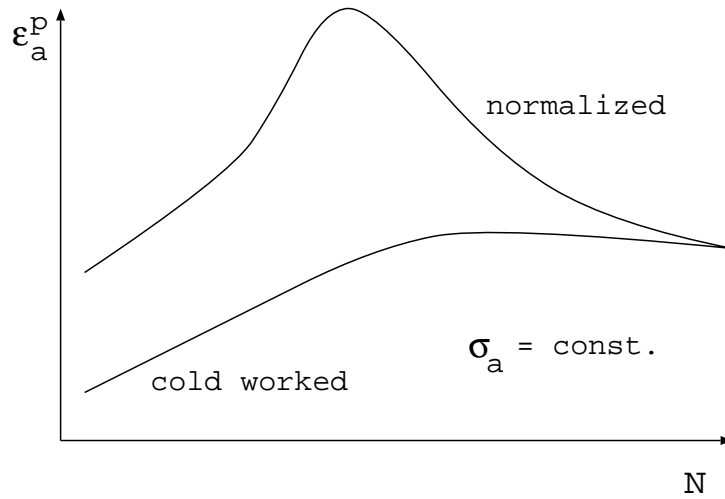


Figure 2.2: Schematic cyclic load-deformation curves, see [65].

Different Load Levels

It is well known [56, 88] that there is a great influence of the history of loading in case that load amplitude is not constant. If the sequence of the loading levels e.g. in a two level fatigue test is changed, there is a much longer lifetime if the lower load level is applied first, and a shorter lifetime if first the higher loading takes place. In Fig. 2.3 there are some examples for this behavior. For the chosen scaling of the axis, all results will be on a straight line connecting $P_1 = (1, 0)$ and $P_2 = (0, 1)$ if there is no influence of the load history.

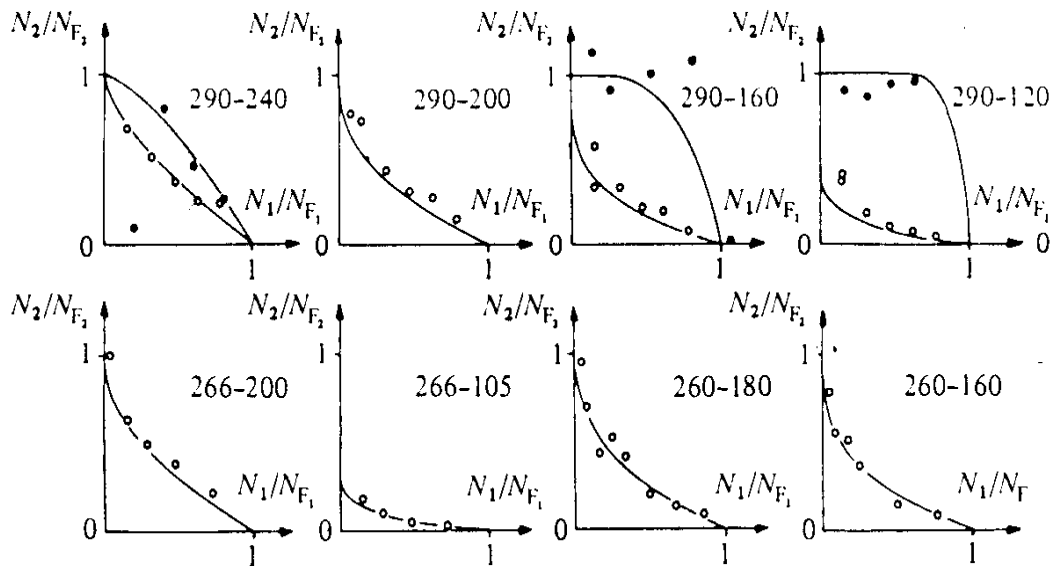


Figure 2.3: Two level fatigue tests for maraging steel at room temperature. ● Low load level first, ○ high load level first. Load amplitudes in *ksi*, see [57] for more details.

This training effect is also observed in [87] for 42CrMo4. The material behavior of 42CrMo4 is close to 30CrNiMo8 used here.

2.2.2 Three Dimensional Effects

Almost any fatigue tests are done for the case of a one-dimensional state of stress. If there is a multiaxial state of stress (e.g. a notch), this has to be transformed to the one-dimensional case. The problems caused by this transformation are well known also from plasticity [5]. For the isotropic case, the three invariants of the stress tensor are used to define a equivalent stress (E.g.: The von Mises equivalent stress based on the J_2 invariant is used often for the yield criterion by metals.). As mentioned in Section 2.1, at first fatigue cracks develop under 45° , i.e. they are shearstress orientated, and in state II they are normal to the applied load. Therefore we observe different anisotropic behavior during lifetime.

2.2.3 Mean Stress

In tension-compression tests, a positive mean stress will reduce lifetime, whereas a negative mean stress will improve lifetime. In Fig. 2.4 three Wöhler-Curves (or S-N-diagrams) with different mean stress are shown for 50% crack probability.

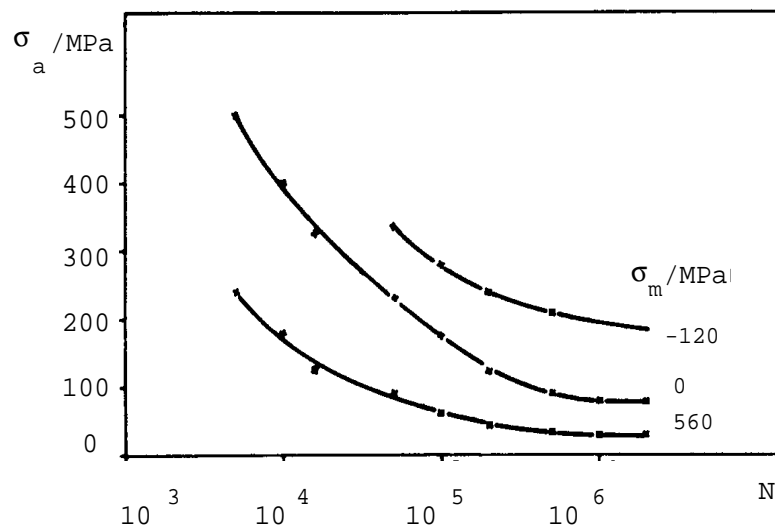


Figure 2.4: Wöhler-Curve for notched tension bars ($K_t=4.5$). Material: X2NiCoMo18 7 5, see [59].

Negative mean stresses have a greater influence on the fatigue limit than positive mean

stresses. The influence of mean stresses is assigned to the crack propagation phase. So, there is e.g. the interesting observation that, if there are great negative mean stresses, microcracking may occur, but will not develop, because a development is only possible under tension [59]. The influence of mean stresses is also dependent on the load case. There is a great influence in tension-compression tests as mentioned and only low or even no influence in torsion tests.

For lifetime calculations, the mean stress effect is usually considered by the use of *Smith* or *Haigh* diagrams.

2.2.4 Frequency

If the parts are well cooled and the frequency is low ($0.1 \leq f \leq 200Hz$), there is only a very small influence of the frequency [33]. In this case there is no need to take inertia forces into account.

If the load frequency is in the vicinity of the eigenfrequency of the part, certainly inertia forces have to be considered. In [30] e.g., there is an example showing that the use of a part with statically optimized shape can reduce the lifetime of the part. This can happen, because by optimization, the eigenfrequency of the part is changed and the new eigenfrequency is maybe closer to the load frequency than the eigenfrequency of the part with start shape.

2.2.5 Size Effect and Scattering

It is an inherent feature of life time tests that there is a large scattering of the results.

There is the observation that the lifetime will increase, if the broken parts of a specimen are used as specimens for the following tests. Another found effect is that the lifetime of a wire is increased by shortening the wire [42]. These effects are explained assuming some weakness of the material (inclusions, voids, surface inhomogenities) statistically distributed and the damage accumulation highly concentrated at these places.

The probability of a fail-down of the structure is increased with the number of possible places for the failure. In the first example the weakest link of the original specimen vanished, so the new parts will have longer lifetimes. In the second example the possibility of a weaker link increases with the length of the wire. The scatter of lifetime tests can be explained by the scatter of weakness distributed in the specimens.

2.3 Engineering Lifetime Calculation

A basis for the calculation of the lifetime of a notched specimen is the knowledge of the S-N-diagram for smooth specimens. Depending on the material, the notch has no influence (notch sensitivity $\eta = 0$, e.g. cast iron with lamellar graphite [60]) or some influence on the fatigue strength. Full influence ($\eta = 1$) means, the fatigue strength of the notched specimen is reduced by the notch factor K_t . This is not observed. Normally, there is some influence of the notch ($0 \leq \eta < 1$). The quotient of the fatigue strength of the smooth and the notched specimens is called fatigue notch factor:

$$K_f = \frac{\sigma_f}{\sigma_f^n}. \quad (2.2)$$

A relation between the notch sensitivity, the notch factor and the fatigue notch factor is given by the following equation:

$$\eta = \frac{K_f \Leftrightarrow 1}{K_t \Leftrightarrow 1}. \quad (2.3)$$

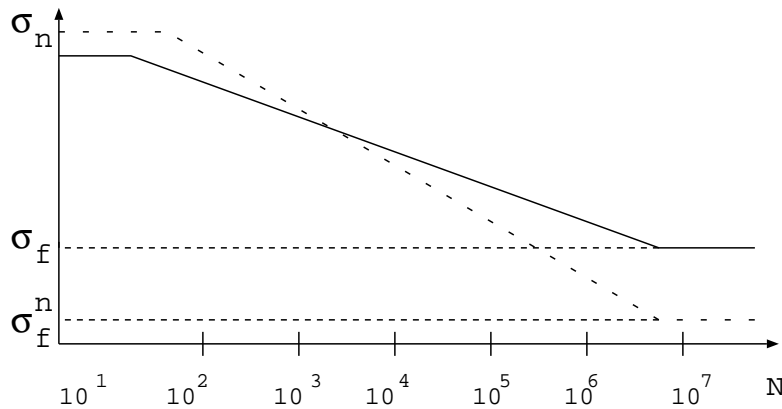


Figure 2.5: Schematic S-N-diagrams for smooth and notched specimens.

It is remarkable that the lifetime of the notched specimens in the VLCF is higher than the lifetime of the smooth specimen. Normally, the curves intersect at $N = 10^1 \Leftrightarrow 10^4$ cycles [60].

2.3.1 Lifetime Calculation in LCF and HCF

We assume that the load amplitude is constant during lifetime. In cases of a random load amplitude *Rainflow* counting is normally adopted [76]. If there is a sequence of different but constant load levels, often a linear damage accumulation is used (see next section).

In the past a lot of different lifetime-load relations were proposed fitting the experimental results [22]. In this work the approaches of *Wöhler*:

$$\lg N = a \Leftrightarrow b\sigma \quad (2.4)$$

and of *Basquin*

$$LgN = a \Leftrightarrow b \lg \sigma \quad (2.5)$$

will be used to describe this relation. These relations were worked out especially for HCF. In addition, a fatigue notch factor has to be chosen. "Neuber's" fatigue notch factor proposed on the basis of micro support caused by microplasticity has found wide application:

$$K_f = K_t \sqrt{\frac{R}{R + s\rho^*}} \quad (2.6)$$

with

R : is the notch radius, ρ^* : is a material parameter and s : is depending on loading conditions and specimen.

With the fatigue notch factor, as well as the knowledge of the S-N-diagram for the unnotched specimen, the chosen S-N relation and a determined intersection point of the S-N curve of the notched parts with the unnotched parts (compare Fig. 2.5) it is easy to calculate the lifetime of a notched part for any load level.

In this approach maximization of lifetime through shape optimization is realized by minimizing the fatigue notch factor [30, 31].

In LCF, plasticity has a dominating influence even on a macroscopic scale.

The experiments are often strain driven. If both axes are logarithmically scaled, a linear relation can be found (Fig. 2.6) The Coffin-Manson equation [56, 59] describes this relationship:

$$\Delta\varepsilon_p = \varepsilon_0 N_F^c \quad (2.7)$$

with

the material constants: c , ε_0 .

In this modellization, maximization of lifetime is connected with minimization of plastic strain.

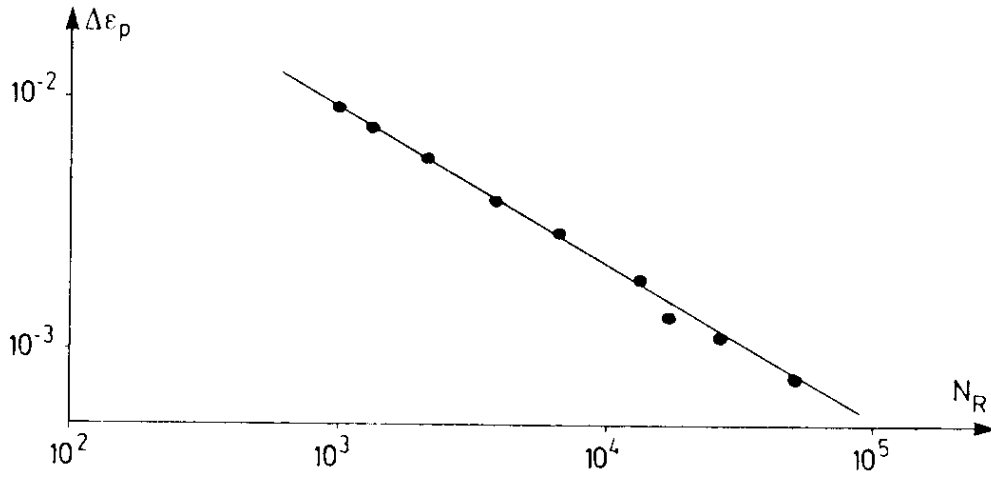


Figure 2.6: Lifetime-Strain relation in LCF for strainhardened steel: AISI 1010 at room temperature, see [51].

2.3.2 Damage Accumulation

In the last sections the determination of lifetime has been described for a constant load level (strain in LCF and stress in HCF). In the case that there are some load sequences with different but constant load level within a block, often linear damage accumulation according to *Miner's* rule is used:

$$D_i = \frac{N_i}{N_{fi}}, \quad (2.8)$$

where

- D_i : is the damage of a block with constant amplitude,
- N_i : is the number of cycle with this load amplitude and
- N_{fi} : is the number of cycle to failure for this load amplitude.

If D :

$$D = \sum_{i=1}^n D_i. \quad (2.9)$$

reaches one, failure will take place. In this approach only linear damage accumulation is regarded without any attention to the sequence of the loading.

2.4 Discussion

There are a lot of other factors influencing fatigue behavior (e.g. temperature, atmosphere, manufacturing process, in [60] an overview can be found), but it is out of the scope of this work to describe all these effects. It has been tried to keep all influencing factors constant for the fatigue tests to study the effect of designing the free boundary of the dynamically loaded part.

In the last sections, it was shown how to determine the lifetime of a part loaded in LCF or HCF. Nevertheless, these "engineering" descriptions give very poor results if the loading is complex [55]. The material parameters of the different fatigue notch factor hypotheses are not independent of the load case (see Eq. 2.6).

Besides this, in Section 2.2.1, it was shown that there is a history dependency. In Section 6.2 a stress redistribution is found. All these effects will be considered in a more detailed approach found within the Continuum Damage Mechanics Concept described in Chapter 4.

Chapter 3

Formulation and Solution of the Static Shape Optimization Problem

In this chapter, the static shape optimization problem is defined as the minimization of maximum stress. In general, the point of maximum stress can be within the considered solid body or on the surface. To find this point is not trivial. Generally, the point of maximum stress for notch problems is on the notch surface, but exception to this rule can be found in literature (e.g. [82]: plate with bilateral notched edges, loaded in pure shear). However, in this work we restrict ourselves to special notch problems, where the maximum stress for the undamaged material will always appear on the notch surface.

In the first section of this chapter the continuous problem is defined. In the second section the discretized static shape optimization problem is specified, and in the third section there are some remarks for the implementation of the numerically approximated solution of the discretized static problem.

3.1 Continuous Optimization Problem

In this section, the equations defining the field problem are summarized first. The solution of this problem will be approximately computed using the Finite Element Method (described in Section 3.2.1). After this, the optimization problem is formulated. The static optimization problem is specified in more detail for the discretized structure in Section 3.2.2.

3.1.1 Boundary Value Problem in Linear Elasticity

In the domain $\Omega \subset \mathcal{R}^3$ with a Lipschitz boundary surface Γ , the following set of equations given in a tensorial notation - referred to an orthogonal Cartesian coordinates system $\mathbf{x} = (x_1, x_2, x_3)$ - has to be fulfilled:

$$\tau_{km,k} = 0 \quad (\text{equilibrium condition}), \quad (3.1)$$

$$e_{km} = \frac{1}{2}(v_{k,m} + v_{m,k}) \quad (\text{kinematic relation}), \quad (3.2)$$

$$\tau_{km} = \frac{E}{1 + \nu} \left(e_{km} + \frac{\nu}{1 \Leftrightarrow 2\nu} \delta_{km} e_{qq} \right) \quad (\text{material law, linear elastic material}) \quad (3.3)$$

where

E : Young's modulus and
 ν : Poisson's ratio.

The displacement vector v_k has three independent components. Out of the displacement vector v_k the strain tensor e_{km} (six various components) is computed. These six components cannot be independent. They have to fulfill the compatibility equations additionally (see [41]):

$$e_{km,pq} + e_{pq,km} \Leftrightarrow e_{kp,mq} \Leftrightarrow e_{mq,kp} = 0. \quad (3.4)$$

By replacing the stresses in Eq. 3.1 with Eq. 3.2 and Eq. 3.3 the Navier equations:

$$v_{m,kk} + \frac{1}{1 \Leftrightarrow 2\nu} v_{k,km} = 0 \quad (3.5)$$

are derived. The Navier equations with the following mixed boundary conditions define the boundary value problem for a instantaneously fixed free boundary Γ^* :

$$\begin{aligned} v_k &= v_k^* & \text{on } \Gamma_k & \quad (\text{Dirichlet conditions}), \\ p_m &= p_m^* & \text{on } \Gamma_s & \quad (\text{Neumann conditions}). \end{aligned} \quad (3.6)$$

The whole boundary Γ , is decomposed into a kinematic and a static part (Fig. 3.1):

$$\Gamma = \Gamma_k \cup \Gamma_s \quad \text{and} \quad \Gamma_k \cap \Gamma_s = \emptyset \quad \text{with} \quad \Gamma_k \neq \emptyset. \quad (3.7)$$

The free boundary is a simply connected subset of the static boundary ($\Gamma^* \subset \Gamma_s$). It is assumed to be loadfree ($p_m|_{\Gamma^*} = 0$).

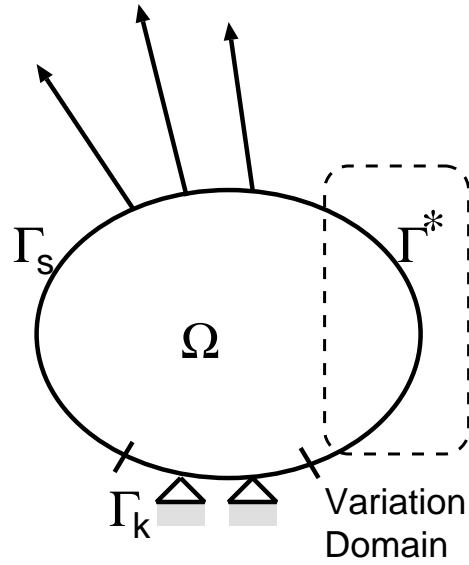


Figure 3.1: Shape optimization problem.

3.1.2 Nonlinear Optimization Problem

In this work we will deal with constrained optimization problems. Nevertheless, it is useful to define the unconstrained optimization problem and the conditions for a solution at first, because often constrained optimization problems are transformed into unconstrained problems.

Unconstrained Optimization Problem

An unconstrained optimization problem is defined by the following expression:

$$\mathcal{F} = \min_{\mathbf{t} \in \mathcal{U}} f(\mathbf{t}), \quad (3.8)$$

where

$f(\mathbf{t})$: is the cost function and
 \mathbf{t} : is the design vector (e.g. node coordinates of the free boundary).

$\mathbf{t}^* \in \mathcal{U}$ is a global minimum if:

$$f(\mathbf{t}^*) \leq f(\mathbf{t}) \quad \forall \quad \mathbf{t} \in \mathcal{U} \subset \mathcal{R}^n. \quad (3.9)$$

A local minimum is defined by the following expression:

$$f(\mathbf{t}^*) \leq f(\mathbf{t}) \quad \forall \quad \mathbf{t} \in \mathcal{U}_\epsilon(\mathbf{t}^*) \quad \{ \mathbf{t} \in \mathcal{U}_\epsilon(\mathbf{t}^*) \mid \| \mathbf{t} - \mathbf{t}^* \| \leq \epsilon \}. \quad (3.10)$$

If \mathbf{t}^* is a solution of the unconstrained optimization problem, it will fulfill the following necessary condition:

$$\nabla f(\mathbf{t}^*) = \left(\frac{\partial f}{\partial t_1}, \frac{\partial f}{\partial t_2}, \dots, \frac{\partial f}{\partial t_n} \right)_{\mathbf{t}^*} = \mathbf{0}. \quad (3.11)$$

We introduce the Hessian matrix to formulate a sufficient optimality criterion:

$$H(\mathbf{t}) = \left[\frac{\partial^2 f}{\partial t_i \partial t_j} \right]. \quad (3.12)$$

If \mathbf{t}^* is a local solution of the unconstrained problem, the Hessian matrix has to be positive definite in its vicinity.

Constrained Optimization Problem

The constrained optimization problem is defined as:

$$\mathcal{F} = \min_{\mathbf{t}} \{ f(\mathbf{t}) \mid \mathbf{h}(\mathbf{t}) = \mathbf{0}, \mathbf{g}(\mathbf{t}) \leq \mathbf{0} \}. \quad (3.13)$$

with

$\mathbf{h}(\mathbf{t})$: is a set of equality constraints and
 $\mathbf{g}(\mathbf{t})$: is a set of inequality constraints.

If the cost function and/or the constraints are nonlinear, Eq. 3.13 defines a nonlinear constrained optimization problem.

For static shape optimization, the maximum stress on the free boundary is often chosen as cost function (an overview of usual cost functions and constraints can be found in [96]). Therefore, the following problem results:

$$\min(f(\mathbf{t})) = \min \left(\max_{\Gamma^*}(\sigma_{eq}) \right), \quad (3.14)$$

where

σ_{eq} : is the von Mises equivalent stress.

The solution space $\mathcal{S} \subset \mathcal{R}^n$ is determined by the side constraints (for shape optimization problems: variation domain):

$$\mathcal{S} := \{\mathbf{t} | \underline{t}_i \leq t_i \leq \overline{t}_i\} \subset \mathcal{R}^n. \quad (3.15)$$

We introduce the Lagrange function to define the optimality conditions for the constrained optimization problem:

$$L(\mathbf{t}, \boldsymbol{\lambda}, \boldsymbol{\mu}) = f(\mathbf{t}) + \lambda_i g_i(\mathbf{t}) + \mu_j h_j(\mathbf{t}), \quad (3.16)$$

(Remark: Einstein's sum convention is adopted.)

where $\boldsymbol{\lambda} \in \mathcal{R}^{m_g}$ and $\boldsymbol{\mu} \in \mathcal{R}^{m_h}$ are Lagrange multipliers or dual variables.

Further more, we need the following definitions to determine necessary and sufficient conditions for the constrained optimization problem:

- Definition 1: $\mathcal{P} \subset \mathcal{S}$ includes all possible solutions of Eq. 3.13:

$$\mathcal{P} := \{\mathbf{t} | h_i(\mathbf{t}) = 0, i = 1, \dots, m_h; g_j(\mathbf{t}) \leq 0, j = 1, \dots, m_g\}. \quad (3.17)$$

- Definition 2: \mathcal{I} is called index set. It summarizes the active inequality constraints:

$$\mathcal{I}(\mathbf{t}) := \{j | g_j(\mathbf{t}) = 0, j = 1, \dots, m_g\}. \quad (3.18)$$

- Definition 3: The constraint qualification [13] is fulfilled, if the gradients of the equality constraints and the active inequality constraints are linear independent in $\mathbf{t}^* \in \mathcal{P}$:

$$\xi_i \nabla h_i(\mathbf{t}^*) + \xi_j \nabla g_j(\mathbf{t}^*) \neq 0 \quad \forall \boldsymbol{\xi} \neq \mathbf{0} \quad (3.19)$$

with

$$i = 1, \dots, m_g \text{ and } j \in \mathcal{I}(\mathbf{t}^*).$$

- Definition 4: A function $f : \mathcal{R}^n \rightarrow \mathcal{R}$ is called convex, if:

$$f(\zeta \mathbf{t} + (1 \Leftrightarrow \zeta) \mathbf{s}) \leq \zeta f(\mathbf{t}) + (1 \Leftrightarrow \zeta) f(\mathbf{s}) \quad (3.20)$$

$\forall \mathbf{t}, \mathbf{s} \in \mathcal{R}^n$ and $\zeta \in (0, 1)$. (The function is called concave if in Eq. 3.20 the " \leq " is replaced by a " \geq ".)

If the function is differentiable twice, ($f \in \mathcal{C}^2$) convexity and semi-definiteness of the Hessian matrix of f are equivalent.

Convexity is important for optimization algorithms, because mostly only in this special case convergence is ensured.

Duality theory shows that if \mathbf{t}^* , $\boldsymbol{\lambda}^*$ and $\boldsymbol{\mu}^*$ are a saddle point, i.e. if

$$L(\mathbf{t}^*, \boldsymbol{\lambda}, \boldsymbol{\mu}) \leq L(\mathbf{t}^*, \boldsymbol{\lambda}^*, \boldsymbol{\mu}^*) \leq L(\mathbf{t}, \boldsymbol{\lambda}^*, \boldsymbol{\mu}^*) \quad (3.21)$$

$$\forall \mathbf{t} \in \mathcal{R}^n, \forall \boldsymbol{\lambda} \in \mathcal{R}^{m_g} \text{ and } \forall \boldsymbol{\mu} \in \mathcal{R}^{m_h}$$

with $\lambda_i \geq 0$, $i = 1, \dots, m_g$; then \mathbf{t}^* is the global solution of Eq. 3.13 [79, 80].

This means, if the dual variables are known exactly ($\boldsymbol{\lambda}^*$, $\boldsymbol{\mu}^*$), an unconstrained problem results out of Eq. 3.13. Therefore in the past, the same effort was made to solve the dual problem as to determine \mathbf{t}^* directly.

If $f(\mathbf{t})$, $h_i(\mathbf{t})_{i=1, \dots, m_h}$, $g_j(\mathbf{t})_{j=1, \dots, m_g}$ are elements of \mathcal{C}^2 and the constraint qualifications

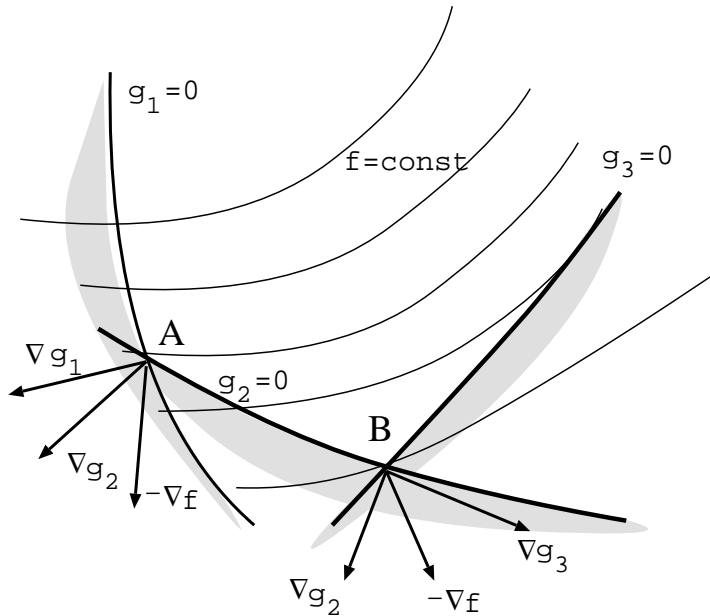


Figure 3.2: Kuhn-Tucker Conditions: Point A is not an optimal solution because there is no nonnegative linear combination of the gradients of the active constraints equal to the negative gradient of f . Point B is an optimal solution because there is no direction of descent in the solution space.

are fulfilled and \mathbf{t}^* is a local minimum, then $\boldsymbol{\lambda}^*$ and $\boldsymbol{\mu}^*$ will exist and the following relations are valid:

$$\begin{aligned} \nabla_{\mathbf{t}} L(\mathbf{t}^*, \boldsymbol{\lambda}^*, \boldsymbol{\mu}^*) &= \mathbf{0}, \\ h_j(\mathbf{t}^*) &= 0, \quad j = 1, \dots, m_h, \end{aligned}$$

$$\begin{aligned}
g_j(\mathbf{t}^*) &\leq 0, & j = 1, \dots, m_g, \\
\lambda_j^* g_j(\mathbf{t}^*) &= 0, & j = 1, \dots, m_g, \\
\lambda_j^* &\geq 0, & j = 1, \dots, m_g.
\end{aligned} \tag{3.22}$$

$$s_i \frac{\partial^2 L(\mathbf{t}^*, \boldsymbol{\lambda}^*, \boldsymbol{\mu}^*)}{\partial t_i \partial t_j} s_j \geq 0 \tag{3.23}$$

$\forall \mathbf{s} \in \mathcal{R}^n$ with $\frac{\partial h_i(\mathbf{t}^*)}{\partial t_j} s_j = 0, i \in \{1, \dots, m_h\}$ and $\frac{\partial g_k(\mathbf{t}^*)}{\partial t_j} s_j = 0, k \in \mathcal{I}(\mathbf{t}^*)$. The meaning of the Kuhn-Tucker conditions (first order conditions: Eq. 3.22) is that the gradient of the cost function and a positive linear combination of the gradients of the active constraints will vanish for a local minimum (see Fig. 3.1.2).

Point *A* in Fig. 3.1.2 is not an optimal solution because the gradient of the cost function does not belong to the subspace defined by the active constraints (all $\lambda_j \geq 0!$). Point *B* is an optimal solution, because there is no direction of descent in the solution space.

For convex problems the Kuhn-Tucker condition is not only a necessary but also a sufficient condition (see [39, 53] for further information).

The meaning of Eq. 3.23 is that the Lagrange function is positive semi-definite in the tangential subspace of the equality and active inequality constraints.

With the same preceptions as before it is also possible to determine sufficient optimality conditions. Besides the Kuhn-Tucker conditions the following relation has to be fulfilled:

$$s_i \frac{\partial^2 L(\mathbf{t}^*, \boldsymbol{\lambda}^*, \boldsymbol{\mu}^*)}{\partial t_i \partial t_j} s_j > 0 \tag{3.24}$$

$$\begin{aligned}
\forall \mathbf{s} \in \mathcal{R}^n, \text{ with } \mathbf{s} \neq \mathbf{0}, \frac{\partial h_i(\mathbf{t}^*)}{\partial t_j} s_j = 0, i \in \{1, \dots, m_h\} \text{ and } \frac{\partial g_i(\mathbf{t}^*)}{\partial t_j} s_j = 0, i \in \{1, \dots, m_g\}, \\
\text{where } \lambda_i^* > 0.
\end{aligned}$$

In this case \mathbf{t}^* is a local minima of f in \mathcal{P} . This means:

$$f(\mathbf{t}^*) < f(\mathbf{t}) \quad \forall \mathbf{t} \in U_\epsilon \cap \mathcal{P}. \tag{3.25}$$

The side constraints are considered as two inequality constraints here.

In the next section the structure analysis for the discretized structure Ω is described. On the basis of this structure analysis, the discretized free boundary value problem is formulated and a numerical method (SQP=Sequential Quadratic Programming) for solving the problem approximately is described.

3.2 Discretized Static Shape Optimization Problem

In this work we restrict ourselves to the 2D plane stress state. In the 2D case the stress and the strain tensor referred to a Cartesian orthogonal coordinate system can be written in the form:

$$\boldsymbol{\sigma} = (\tau_{xx}, \tau_{yy}, \tau_{xy})^T \quad \text{and} \quad \boldsymbol{\varepsilon} = (\varepsilon_x, \varepsilon_y, \gamma_{xy})^T, \quad (3.26)$$

with

$$\gamma_{xy} = 2\varepsilon_{xy}.$$

For homogeneous isotropic material, the matrix

$$\mathbf{D} = \frac{E}{1 \Leftrightarrow \nu^2} \begin{bmatrix} 1 & \nu & 0 \\ \nu & 1 & 0 \\ 0 & 0 & \frac{1-\nu}{2} \end{bmatrix} \quad (3.27)$$

describes linear elastic behavior according to the plane stress state. In this notation Eq. 3.3 can be written in the form:

$$\boldsymbol{\sigma} = \mathbf{D}\boldsymbol{\varepsilon}. \quad (3.28)$$

3.2.1 Structure Analysis

In this work a displacement approach of the FEM is used. For derivation of the method at first the following sets of kinematically admissible displacements are defined:

$$\begin{aligned} \mathcal{K}^* &= \left\{ \mathbf{v} : \Omega \rightarrow \mathcal{R}^2, \mathbf{v} = \mathbf{u}^* \text{ on } , k \right\} \text{ and} \\ \mathcal{K}^0 &= \left\{ \mathbf{v} : \Omega \rightarrow \mathcal{R}^2, \mathbf{v} = \mathbf{0} \text{ on } , k \right\}. \end{aligned} \quad (3.29)$$

The minimum principle of potential energy states: If there is a solution of the boundary value problem (Eq. 3.5 and Eq. 3.6) there is the following equivalence:

$$\mathbf{u} \in \mathcal{K}^* \text{ solution of Eq. 3.5 and Eq. 3.6} \quad \Leftrightarrow \quad \Pi(\mathbf{u}) \leq \Pi(\mathbf{u} + \mathbf{v}) \quad \forall \mathbf{v} \in \mathcal{K}^* \quad (3.30)$$

The total potential energy of the body in the case of vanishing volume forces is the sum:

$$\Pi(\mathbf{u}) = \frac{1}{2}Q(\mathbf{u}, \mathbf{u}) \Leftrightarrow \Phi(\mathbf{u}), \quad (3.31)$$

of the strain energy:

$$Q(\mathbf{u}, \mathbf{u}) = \int_{\Omega} \boldsymbol{\varepsilon}^T \mathbf{D} \boldsymbol{\varepsilon} d\Omega,$$

and the potential energy of the surface loads:

$$\Phi(\mathbf{u}) = \int_{\Gamma_s} \mathbf{p}^{*T} \mathbf{u} d, .$$

If a function \mathbf{u} minimizes the functional $\Pi(\mathbf{u})$, then the first variation of $\Pi(\mathbf{u})$ must vanish:

$$\delta\Pi = 0 = Q(\mathbf{u}, \mathbf{w}) \Leftrightarrow \Phi(\mathbf{w}) \quad \forall \quad \mathbf{w} \in \mathcal{K}^0. \quad (3.32)$$

(Remark: Eq. 3.32 can also be understood as a weak formulation of the equilibrium condition Eq. 3.1.)

At this point, the structure is divided into n_e triangular finite elements:

$$\Omega \approx \tilde{\Omega} = \bigcup_{e=1}^{n_e} \Omega^e. \quad (3.33)$$

For each element, we introduce the vector \mathbf{d}^e of nodal displacements and the matrix \mathbf{N}^e of shape functions, which contains the nodal basis functions of the approximating subspace. Thus, the approximation of \mathbf{u} in the element e has the form:

$$\mathbf{u}_h = \mathbf{N}^e(\mathbf{X}) \mathbf{d}^e. \quad (3.34)$$

The strains $\boldsymbol{\varepsilon}$ are derived by differentiation of Eq. 3.34:

$$\boldsymbol{\varepsilon}^e = \mathbf{B}^e \mathbf{d}^e \quad (3.35)$$

(Remark: For an elementwise linear approximation of the displacements the corresponding strains are constant in each element.)

Writing Eq. 3.32 for one element and introducing the displacement set-up (Eq. 3.34 and Eq. 3.35) leads to the following formula:

$$\delta\Pi^e(\mathbf{u}_h) = \delta \mathbf{d}^{eT} \left(\int_{\Omega^e} \mathbf{B}^{eT} \mathbf{D} \mathbf{B}^e d\Omega \right) \mathbf{d}^e \Leftrightarrow \delta \mathbf{d}^{eT} \left(\int_{\Gamma_s \cap \Gamma_e} \mathbf{p}^{*T} \mathbf{N}^e d, \right) = 0. \quad (3.36)$$

The element stiffness matrix is introduced by:

$$\mathbf{K}^e = \int_{\Omega^e} \mathbf{B}^{eT} \mathbf{D} \mathbf{B}^e d\Omega. \quad (3.37)$$

An affine linear transformation to triangular coordinates and explicit integration is performed to determine the element stiffness matrix (Eq. 3.37). The given loads are transformed into a nodal load vector:

$$\mathbf{F}^e = \int_{\Gamma_s \cap \Gamma_e} \mathbf{p}^{*T} \mathbf{N}^e d, . \quad (3.38)$$

Introducing the last two equations in Eq. 3.36 leads to:

$$\delta\Pi(\mathbf{u}_h) = \delta\mathbf{d}^{eT} (\mathbf{K}^e \mathbf{d}^e \Leftrightarrow \mathbf{F}^e) = 0. \quad (3.39)$$

$\delta\mathbf{d}^e$ is an arbitrary vector. Therefore the minimum of potential energy can only be achieved if the term in parentheses vanishes. Superposition of all elements Ω^e leads to the fundamental FE-equation for the whole structure:

$$\mathbf{K}\mathbf{d} = \mathbf{F}, \quad (3.40)$$

where

- \mathbf{K} : is the global stiffness matrix,
- \mathbf{d} : is the vector of (global) nodal displacements and
- \mathbf{F} : (global) nodal force vector.

If the nodal displacement vector is determined solving Eq. 3.40, the strains can be computed according to Eq. 3.35. With the strains, the stresses are computed element by element with Hooke's law. The stress components at a node are determined by averaging the stress components of the adjacent elements:

$$\sigma_{ij}^{node} = \frac{1}{n_e} \sum_{k=1}^{n_e} \sigma_{ij}^k, \quad (3.41)$$

where

n_e : is the number of elements containing the specified node.

3.2.2 Formulation of the Discretized Static Shape Optimization Problem

After the discretization of the structure ($\tilde{\Omega} \approx \Omega$), the FE-node coordinates on the free boundary are the natural design variables.

Therefore the constraints in a variation domain can be written as:

$$\begin{aligned} \underline{X}_i &\leq X_i \leq \overline{X}_i && \text{and} \\ \underline{Y}_i &\leq Y_i \leq \overline{Y}_i. \end{aligned} \quad (3.42)$$

Besides these constraints in variation domain, some other constraints are considered. They are described in detail in Section 3.2.4.

The proposed cost function:

$$\mathcal{F} : \min f_1(\mathbf{t}) = \min \left(\max_{i=1, \dots, m} (\sigma_{eq}^i) \right). \quad (3.43)$$

where

$(X_i, Y_i) \in \Omega^*$ and m : is the number of design nodes on the free boundary

implies the problem that during the optimization procedure, the node with maximum stress may change. Therefore, the cost function is not differentiable. However, this property is necessary because gradient methods of mathematical programming (MP) will be used to solve the problem. To overcome this problem, we introduce an additional design variable (see also [82]) β and the additional constraints:

$$\sigma_{eq}^i \Leftrightarrow \beta \leq 0 \quad i = 1, \dots, m. \quad (3.44)$$

The new cost function is:

$$f(\mathbf{t}) = \min \beta. \quad (3.45)$$

Now, the cost function is linear and depends only on the additional design variable. This additional design variable is forced to be greater than the highest stress on the free boundary by the additional constraints.

(Remark: Although the original cost function is now transferred into the set of constraint, we will call the function characterizing the fatigue behavior cost function further on.)

Another method to overcome this problem can be found in [92]. This second method was also tested and led to the same results as the method described above.

The cost function is linear now, but the constraints are nonlinear. So we also have a nonlinear constrained optimization problem.

3.2.3 Optimizer

A helpful overview of currently used optimization procedures can be found in [25, 31, 83]. In Fig. 3.3 a short summary is given.

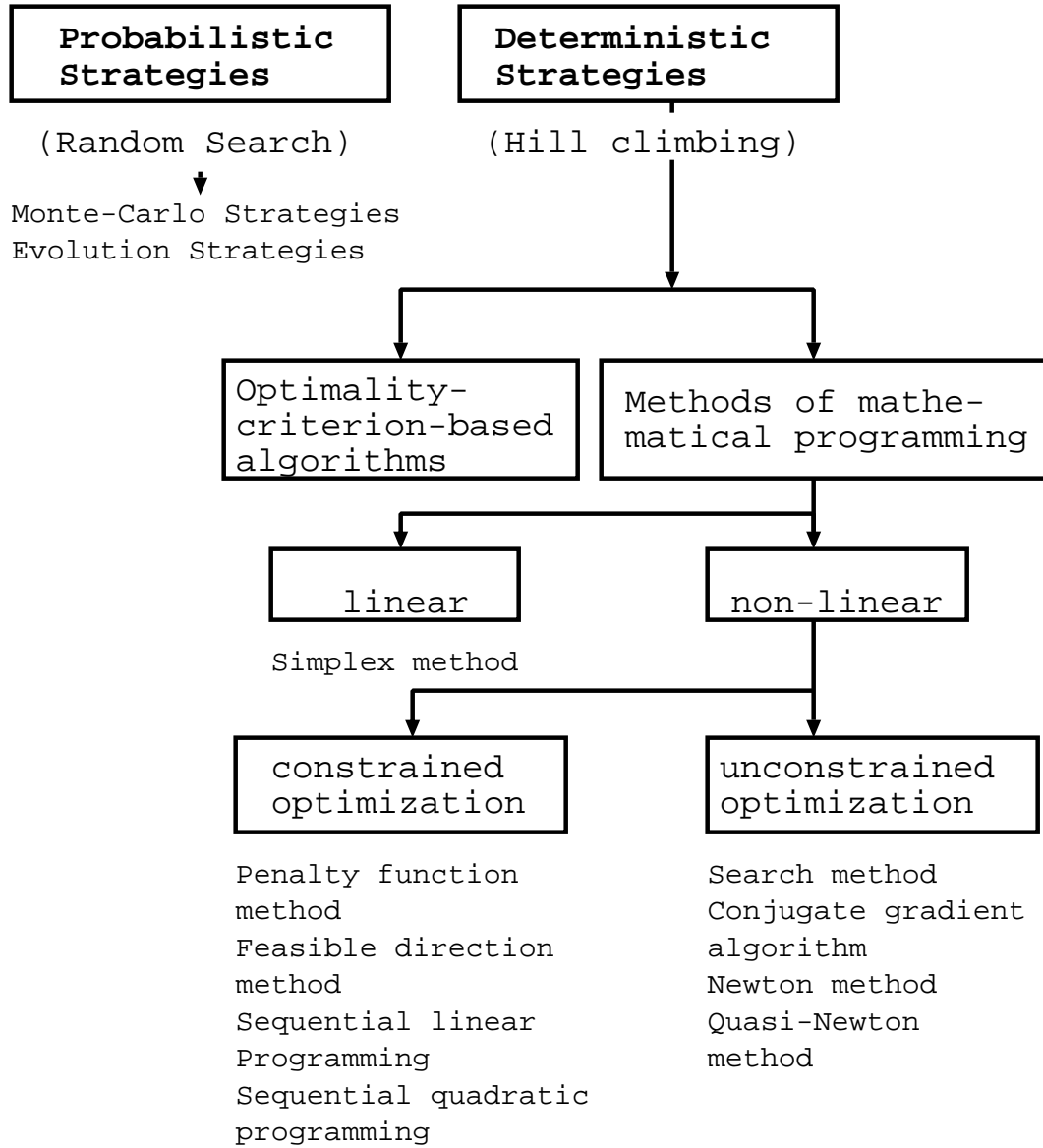


Figure 3.3: Summary: Most important optimization strategies [82].

Mathematical Programming versus OC-Methods

It is well known that Optimality Criteria Methods lead to very accurate optimization results in short CPU-time [64, 78, 82, 83, 84]. All OC-methods consist of two principal constituents:

The optimality criteria itself (mathematical formulation: e.g. Kuhn-Tucker conditions or intuitive criterion: e.g. strain energy density constant) and an algorithm to change the structure in such a way that the mentioned optimality criterion/criteria is/are achieved. As an example for an OC-Method *Schnack's* gradientless method is briefly summarized: *Schnack* has formulated the following two hypotheses on the basis of *Neuber's* [66] and *Baud's* [8] works as optimality criteria for plane and axisymmetric structures:

Let A and B be the end points of the free boundary, $$. If the free boundary is chosen so that the tangential stress σ_t is constant between A and B , then the stress concentration is minimized.*

If there is no $$ with constant tangential stress according to the first hypothesis available in the chosen variation domain, then the stress concentration is minimized if the length (Λ) with σ_t on $*$ is maximized and σ_t has no higher values on $*$.*

These hypotheses were extended in [45, 82, 83] to axisymmetric and 3-D-problems using von Mises equivalent stress instead of the tangential stress.

Remark: If several load cases are considered, the maximum equivalent stress of all load cases is used.

The optimization algorithm is based on the observation that the stress is locally increased by the reduction of the local curvature radius and vice versa.

In addition, there is the observation that increasing the stress minima also reduces the maxima in its vicinity (notch reaction law).

According to these two observations, the point of minimum equivalent stress is shifted by increasing the normalized local curvature, and the point of maximum equivalent stress is shifted by reducing the normalized local curvature. The points between these two points are interpolated.

In [64, 78] an extension of this algorithm can be found. In these papers the shift of the nodes is calculated not only for the points of minimum and maximum stress but for all points on the free boundary.

The advantage of these OC-methods is that a CPU-time intensive gradient calculation is not necessary.

The methods of mathematical programming are used in this work for two reasons: First, neither optimality criteria nor algorithms for the special cost functions considered here, exist. Second, in this work special constraints are added to the cost function, which are not allowed if OC-methods are used.

Sequential Quadratic Programming

In this work, Sequential Quadratic Programming (SQP) is used to solve the discretized optimization problem numerically, because SQP is well established for nonlinear structural optimization problems [30, 31, 79, 80], if the number of constraints and design variables is not too large (≤ 200). The advantages of this procedure are the global convergence and the local superlinear convergence rate. The procedure can be adopted for constrained, highly nonlinear optimization problems (see Fig. 3.3).

The disadvantages of SQP are the scale sensitivity (values of design variables, cost functions and constraints must be harmonized), during optimization the allowed solution space is often left and the convergence rate is dependent on the penalty factors and the merit function.

SQP belongs to the Lagrange methods. Lagrange methods solve the necessary optimality equations directly. The SQP method is based on the successive solution of quadratic subproblems (QP) of the constraint optimization problem Eq. 3.13. These QPs are derived by a quadratic approximation of the cost function and a linearization of the constraints:

$$\min \frac{1}{2} {}^k p_i {}^k B_{ij} {}^k p_j + \frac{\partial f({}^k \mathbf{t})}{\partial t_i} {}^k p_i \quad (3.46)$$

and

$$\begin{aligned} \frac{\partial h_i({}^k \mathbf{t})}{\partial t_j} {}^k p_j + h_i({}^k \mathbf{t}) &= 0 & \text{for } i = 1, \dots, m_h & \quad \text{and} \\ \frac{\partial g_i({}^k \mathbf{t})}{\partial t_j} {}^k p_j + g_i({}^k \mathbf{t}) &= 0 & \text{for } i = 1, \dots, m_g. & \end{aligned} \quad (3.47)$$

The bounds for this quadratic subproblem (QP) are:

$${}^k t_i \Leftrightarrow \underline{t}_i \leq {}^k p_i \leq \bar{t}_i \Leftrightarrow {}^k t_i \quad \text{for } i = 1, \dots, n. \quad (3.48)$$

The abbreviations have the following meanings: ${}^k \mathbf{t}$ is the k^{th} approximation of the solution, ${}^k \mathbf{B}$ is the k^{th} approximation of the Hessian matrix, it is determined only with first order

information on the basis of the method developed by Powell Han and Wilson (see [81]) and ${}^k\mathbf{p}^*$ is the solution of the k^{th} QP-subproblem Eq. 3.46.

If the optimal Lagrange multipliers are ${}^k\boldsymbol{\lambda}^*$ and ${}^k\boldsymbol{\mu}^*$, we can determine the next iteration step with the following expression:

$$\begin{Bmatrix} {}^{k+1}\mathbf{t} \\ {}^{k+1}\boldsymbol{\lambda} \\ {}^{k+1}\boldsymbol{\mu} \end{Bmatrix} := \begin{Bmatrix} {}^k\mathbf{t} \\ {}^k\boldsymbol{\lambda} \\ {}^k\boldsymbol{\mu} \end{Bmatrix} + \alpha_k \begin{Bmatrix} {}^k\mathbf{p}^* \\ {}^k\boldsymbol{\lambda}^* \Leftrightarrow {}^k\boldsymbol{\lambda} \\ {}^k\boldsymbol{\mu}^* \Leftrightarrow {}^k\boldsymbol{\mu} \end{Bmatrix}. \quad (3.49)$$

α_k is a step size parameter. It is determined by line search of the merit function (see [80]). The SQP-algorithm [79] requires of the user to choose the design variables (node coordinates or de-Boor ordinates of the B-spline approximation, see Section 3.3.2 and Section 5.5.1), to provide the cost function (see Chapter 4), the constraints (see next section) and the sensitivity analysis (see Section 3.3.3).

3.2.4 Constraints

Normally, one tries to keep the number of additional constraints small to save CPU-time. On the other hand it can also happen that the optimum is reached earlier by the introduction of additional constraints, because the solution space is reduced.

Here, three sets of constraints are introduced.

Distance Constraint

This set of constraints compares the distance to the previous and the following neighbor node on the free boundary. This distance is forced to be equal for all nodes on the free boundary:

$$\sqrt{(X_i \Leftrightarrow X_{i-1})^2 + (Y_i \Leftrightarrow Y_{i-1})^2} \Leftrightarrow \sqrt{(X_{i+1} \Leftrightarrow X_i)^2 + (Y_{i+1} \Leftrightarrow Y_i)^2} = 0, \quad (3.50)$$

$i = 2, \dots, m \Leftrightarrow 1$, where m is the number of nodes on the free boundary.

This constraint (Eq. 3.50) is used to keep the mesh regular and to avoid net deterioration. Obviously it cannot be used if the free boundary is described with B-splines.

Concave Constraint

For notch problems, the optimum shape is obviously concave. This is forced by the calculation of the area formed by three adjacent nodes on the free boundary:

$$2A_i = \begin{vmatrix} 1 & 1 & 1 \\ X_{i-1} & X_i & X_{i+1} \\ Y_{i-1} & Y_i & Y_{i+1} \end{vmatrix}, \quad (3.51)$$

where

$i = 1, \dots, m \Leftrightarrow 1$, for $i = 1$: $X_0 = X_2$ and $Y_0 = \Leftrightarrow Y_2$, because of the symmetry.

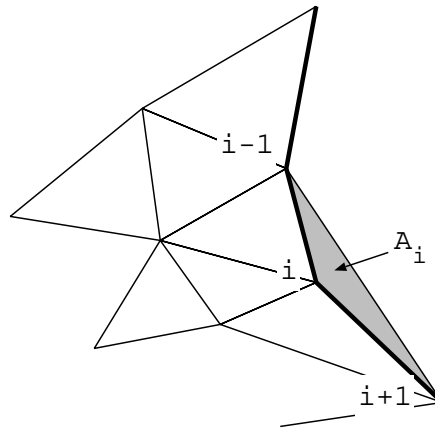


Figure 3.4: Area of the triangle formed by three adjacent nodes on the free boundary.

This set of constraints helps to avoid oscillations in the low stress area. In [86] this problem is mentioned in detail and an extension of this set of constraints can be found for the case that the whole free boundary can be decomposed in parts which are determined convex or concave a priori [31].

Manufacturing Constraint

The considered optimization example (see Section 5.4) is studied not only theoretically but also experimentally. In order to achieve that the optimum shape is producible with a CNC-milling cutting machine, the smallest local curvature radius has to be greater than the smallest cutter radius:

$$R_{min} \Leftrightarrow R_i \leq 0. \quad (3.52)$$

At first the center (X_{0i}, Y_{0i}) of the local curvature radius has to be determined. It is found at the intersection of the two mid-verticals (i-1, i and i,i+1, see Fig. 3.5):

$$X_{0i} = \frac{A + B}{N} = \frac{Z_1}{N} \quad \text{and} \quad Y_{0i} = \frac{C + D}{N} = \frac{Z_2}{N}, \quad (3.53)$$

where

$$\begin{aligned} A &= x_{i-1}^2 (y_{i+1} \leftrightarrow y_i) \leftrightarrow x_i^2 (y_{i+1} \leftrightarrow y_{i-1}) + x_{i+1}^2 (y_i \leftrightarrow y_{i-1}), \\ B &= (y_{i+1} \leftrightarrow y_{i-1}) (y_i \leftrightarrow y_{i-1}) (y_{i+1} \leftrightarrow y_i), \\ C &= (x_i \leftrightarrow x_{i-1}) (x_{i+1} \leftrightarrow x_{i-1}) (x_i \leftrightarrow x_{i+1}), \\ D &= x_{i-1} (y_{i+1}^2 \leftrightarrow y_i^2) + x_i (y_{i-1}^2 \leftrightarrow y_{i+1}^2) + x_{i+1} (y_i^2 \leftrightarrow y_{i-1}^2) \\ N &= 2[(x_{i-1} \leftrightarrow x_i) (y_{i+1} \leftrightarrow y_i) \leftrightarrow (x_i \leftrightarrow x_{i+1}) (y_i \leftrightarrow y_{i-1})]. \end{aligned}$$

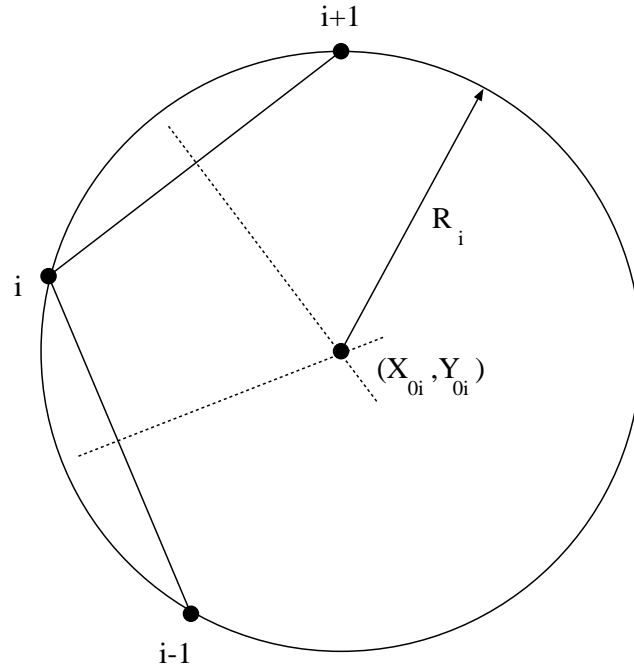


Figure 3.5: Determination of the local curvature radius.

The local curvature radius is:

$$R_i = \sqrt{(X_{0i} \leftrightarrow x_i)^2 + (Y_{0i} \leftrightarrow y_i)^2}. \quad (3.54)$$

There is no need to apply this constraint in every point of the free boundary. In a primary intelligent look on the notch surface, “dangerous points” are determined. The constraint is then only applied at these “dangerous points” near the separation point. (The optimization result depends sensitively on the value of the design variables in this area, see [31, 84].)

3.3 Efficient Algorithms and Implementation

The described optimization procedure for the numerical solution of the discretized static shape optimization problem will be used as a basis for the fatigue (dynamic behavior) optimization problem. Therefore it is necessary to analyze the stress-strain field several times (see Chapter 4) during lifetime. This leads to a rapidly increasing CPU-time. Therefore the optimization problem only can be solved if for the implementation efficient algorithms are used.

3.3.1 Sparse Storing and Iterative Solver

The chosen displacement method with linear elements requires a very fine FE-mesh to determine the stress-strain field accurately. This leads to a lot of nodes, i.e. a high degree of freedom (*DOF*). A sparse storing of the global stiffness matrix is therefore necessary to reduce computer memory consumption.

The stiffness matrix \mathbf{K} is symmetric and positive definite. Instead of the upper triangle of \mathbf{K} only the nonzeros of this triangle are stored in a vector \mathbf{k} . The row and column indices are kept by introducing two additional vectors. The nonzero elements of the stiffness matrix are put into \mathbf{k} row by row. The first added vector with dimension $n = \text{rank}(\mathbf{K})$ contains pointers to the main diagonal elements of \mathbf{K} in \mathbf{k} . The second vector with the same length as \mathbf{k} contains the column index of \mathbf{K} for every component of \mathbf{k} (see [72] for a more detailed description).

Instead of a direct solver (e.g. Cholesky-Method [30, 31]), in this work an iterative solver (preconditioned CG-method: SSORCG=Successive Symmetric Overrelaxed Conjugate Gradient Method) is used to solve the linear FE-equation system (Eq. 3.40.). It was found [72] by several - not too small ($\geq 1000\text{DOF}$) - numerical examples that the computation time for the solution of the linear FE-equation system is reduced by a factor $\approx 5 \cdot \cdot \cdot 10$, if the SSORCG is used instead of a Cholesky method.

Equivalent to solving the linear equation system $\mathbf{K}\mathbf{x} = \mathbf{b}$ is the minimization of the following quadratic functional:

$$f(\mathbf{x}) = \frac{1}{2}\mathbf{x}^T \mathbf{K}\mathbf{x} \Leftrightarrow \mathbf{b}^T \mathbf{x} + c. \quad (3.55)$$

If a start solution \mathbf{x}_0 is known, the residuum is calculated in the following form:

$$\mathbf{r}_0 = \mathbf{b} \Leftrightarrow \mathbf{K}\mathbf{x}_0. \quad (3.56)$$

Using $\mathbf{p}_0 = \mathbf{r}_0$ as a first direction of descent, the equations for the k^{th} iteration are:

$${}^k \alpha = \frac{{}^k \mathbf{r}^T {}^k \mathbf{r}}{{}^k \mathbf{p}^T \mathbf{K} {}^k \mathbf{p}},$$

$$\begin{aligned}
{}^{k+1}\mathbf{x} &= {}^k\mathbf{x} + {}^k\alpha {}^k\mathbf{p}, \\
{}^{k+1}\mathbf{r} &= {}^k\mathbf{r} + {}^k\alpha \mathbf{K} {}^k\mathbf{p}, \\
{}^k\beta &= \frac{{}^{k+1}\mathbf{r}^T {}^{k+1}\mathbf{r}}{{}^k\mathbf{r}^T {}^k\mathbf{r}} \quad \text{and} \\
{}^{k+1}\mathbf{p} &= {}^{k+1}\mathbf{r} + {}^k\beta {}^k\mathbf{p}.
\end{aligned} \tag{3.57}$$

It can be shown, that the exact solution is found after maximal $n = \text{rank}(\mathbf{K})$ iterations [1].

In practical use the iteration process is stopped, if a limit sufficiently small for the Euclidean norm of the residual vector is reached.

The derivation of the recursive equations and more details can be found in [1, 43].

A description of the preconditioning is found in [1, 50, 54].

The use of this iterative method becomes particularly valuable if a good start solution is available. In optimization the values of the last iteration are a very close approximation.

3.3.2 Design Variables

If a structure is approximated with finite elements, the natural design variables for shape optimization are the node coordinates of the free boundary.

With this choice there is a great number of design variables if accurate results in structure analysis are desired. Besides this, many authors mention a lot of problems with node coordinates in case methods of MP are used for optimization. Besides the large CPU-time due to the great number of design variables, there is e.g. the problem of nonsmooth boundaries in the area of low stresses. (The caused singularities are bad or even not approximated because of the rough discretization in this area.) This problem is overcome in this work by introducing the concave constraint. Another very important problem is that, according to the great number of design variables, a lot of CPU-time is necessary for the sensitivity analysis.

At the moment, one usually distinguishes between the design and the analysis model. Often the free boundary is described with Bezier or B-splines [26, 27, 63, 75] and the control parameter of these descriptions are the design variables.

The advantage of this description is that it is possible to describe a complicated boundary with only a few design variables.

If such a description is chosen, this is a second approximation of the structure. Or in other words, the solution space is constrained once more [31, 44].

In this work besides the node coordinates, B-splines will be used to describe the free boundary. With the use of B-spline control parameters as design variables, a good approximation of the solution will be calculated in a short time (see Section 5.5.1).

In the following subsections a brief introduction in B-(or basis) splines is given. For more

general information see [14, 32]. In brackets the actual chosen features are outlined.

Introduction to B-splines

There are parametric and nonparametric (used here) B-splines. A B-spline is determined by its polynomial degree n (here: $n = 3$), a sequence of nodes $u_0 \leq u_1 \leq u_2 \leq \dots \leq u_{L+2n-2}$ and the de-Boor ordinates d_i . The B-spline $s(u)$ is defined over the interval given by the domain nodes:

$$[u_{n-1}, u_{L+n-1}] \quad (\text{here: } [u_2, u_{L+2}]). \quad (3.58)$$

L is related to the node multiplicity (here: Every node in the interval of definition has the multiplicity $r_i = 1$. The first and last node have the multiplicity three. This ensures that these points are fixed and lie on the B-spline curve.):

$$L + 1 = \sum_{i=n-1}^{L+n-1} r_i, \quad \left(\text{here: } L + 1 = \sum_{i=2}^{L+2} 1 \right). \quad (3.59)$$

If all nodes inside the definition interval have the multiplicity one, L is the number of sections.

The B-spline is controlled by the control polygon. This is defined by the Greville abscissas and the de-Boor ordinates. The de-Boor ordinates are specified by the user. The Greville abscissas are calculated in the following form:

$$\xi_i = \frac{1}{n} (u_i + u_{i+1} + \dots + u_{i+n-1}) \quad \left(\text{here: } \xi_i = \frac{1}{3} (u_i + u_{i+1} + u_{i+2}) \right) \quad (3.60)$$

In Fig. 3.6 a B-spline with ten sections and polynomial degree $n = 3$ is shown. The node sequence is marked with a “o”. The first and last node of the sequence have the multiplicity three, all the others the multiplicity one. Greville abscissas are marked with a “ Δ ”, the points of the control polygon (Greville abscissa, de-Boor ordinate d_i) are marked by a “ \square ”.

The B-spline is defined by:

$$s(u) = \sum_{i=0}^{L+n-1} d_i N_i^n(u), \quad \left(\text{here: } s(u) = \sum_{i=0}^{L+2} d_i N_i^3(u) \right). \quad (3.61)$$

The basis functions N_i have local support:

$$\text{supp} N_i^n(u) = \{u \mid u \in [u_{i-1}, u_{i+n}]\}. \quad \left(\text{here: } \text{supp} N_i^3(u) = \{u \mid u \in [u_{i-1}, u_{i+3}]\} \right). \quad (3.62)$$

Therefore for a subsection $u \in [u_i, u_{i+1}]$ the following formula results:

$$s(u) = \sum_{j=i-n+1}^{i+1} d_j N_j^n(u) \quad \forall \quad u \in [u_i, u_{i+1}], \quad \left(\text{here: } s(u) = \sum_{j=i-2}^{i+1} d_j N_j^3(u) \right). \quad (3.63)$$

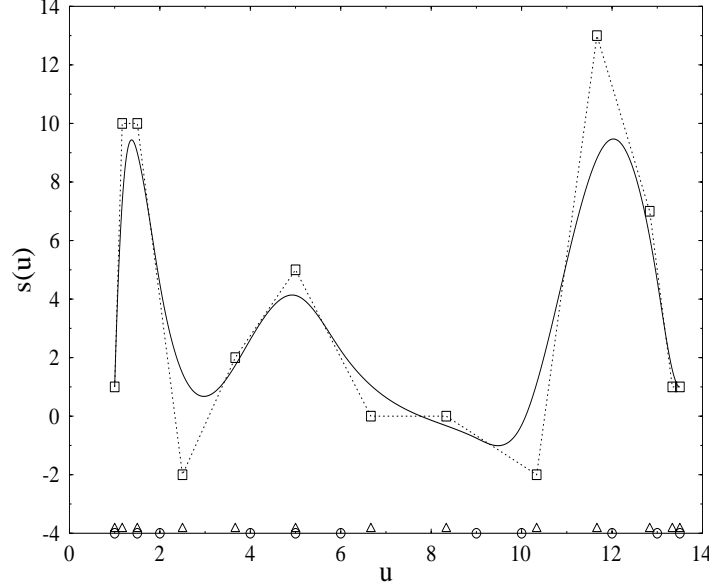


Figure 3.6: Example for the control polygon and the B-spline curve ($n = 3$, $L = 10$).

The basis functions can be derived by recurrence formulas. For this work the *Mansfield, de Boor and Cox* recursion was chosen. Alternative formulations can be found in [32].

$$N_i^n(u) = \frac{u \Leftrightarrow u_{i-1}}{u_{i+n-1} \Leftrightarrow u_{i-1}} N_i^{n-1}(u) + \frac{u_{i+n} \Leftrightarrow u}{u_{i+n} \Leftrightarrow u_i} N_{i+1}^{n-1}(u), \quad (3.64)$$

where

$$N_i^0(u) = \begin{cases} 1 & \text{if: } u_{i-1} \leq u < u_i \\ 0 & \text{else.} \end{cases} \quad (3.65)$$

For the special case considered here the following formula is derived:

$$\begin{aligned} s(u) = & (u_{i+1} \Leftrightarrow u)^2 \frac{d_{i-2} (u_{i+1} \Leftrightarrow u) + d_{i-1} (u \Leftrightarrow u_{i-2})}{(u_{i+1} \Leftrightarrow u_{i-2}) (u_{i+1} \Leftrightarrow u_{i-1}) (u_{i+1} \Leftrightarrow u_i)} \\ & + (u \Leftrightarrow u_i)^2 \frac{d_{i+1} (u \Leftrightarrow u_i) + d_i (u_{i+3} \Leftrightarrow u)}{(u_{i+3} \Leftrightarrow u_i) (u_{i+2} \Leftrightarrow u_i) (u_{i+1} \Leftrightarrow u_i)} \\ & + \frac{d_{i-1} (u_{i+2} \Leftrightarrow u) + d_i (u \Leftrightarrow u_{i-1})}{u_{i+2} \Leftrightarrow u_{i-1}} \left(\frac{u \Leftrightarrow u_{i-1}}{u_{i+1} \Leftrightarrow u_{i-1}} \frac{u_{i+1} \Leftrightarrow u}{u_{i+1} \Leftrightarrow u_i} + \frac{u_{i+2} \Leftrightarrow u}{u_{i+2} \Leftrightarrow u_i} \frac{u \Leftrightarrow u_i}{u_{i+1} \Leftrightarrow u_i} \right) \end{aligned} \quad (3.66)$$

$$\text{for: } u \in [u_i, u_{i+1}), \quad i = 2, \dots, L + 1.$$

Statements in the form “0/0” and not defined nodes (e.g. u_1) are set to zero formally.

Some B-spline properties:

- **Smoothness**

At the points of the node sequence there is \mathcal{C}^{n-r} (here \mathcal{C}^2) smoothness.

- **Local control**

Due to the local support of the basis functions, there is only a local control. A variation of d_i has an influence only in this area (see Fig. 3.7). This local influence makes the B-spline description attractive for shape optimization.

- **Node insertion**

Additional nodes can be inserted into the node sequence (successive strategy, see Section 5.3). In order to save CPU-time, a successive strategy introduced for node coordinates (increasing number of design variables) can be used in the case of a B-spline description of the free boundary, too.

- **Linear precision**

If $l(u)$ is a straight line of the form $l(u) = au + b$, and if we read off the Greville abscissas, the resulting B-spline curve reproduces the straight line. Therefore, for shape optimization, it is very easy to start with a “v”-notched shape.

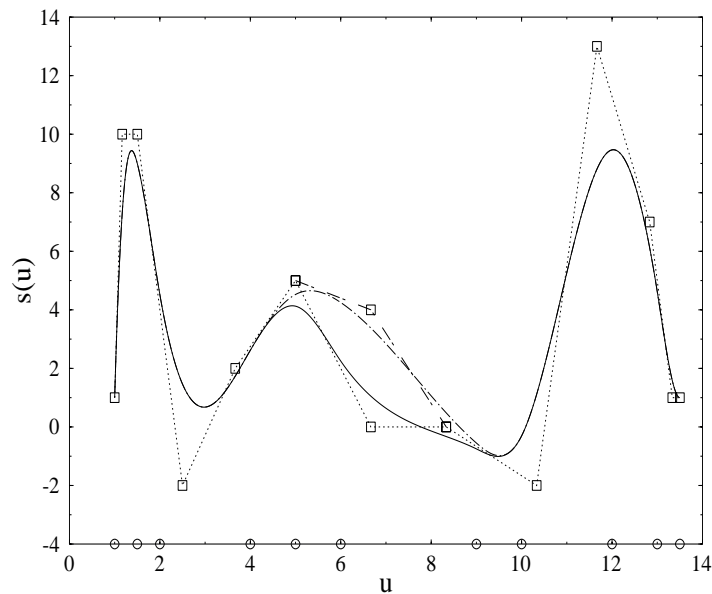


Figure 3.7: Local control of a B-spline curve.

For optimization the de-Boor ordinates are chosen as design variables. During one optimization slope the x -coordinates of the FE-nodes are constant. The distance constraint is

not used, if the free boundary is described with B-splines. After an optimization slope the FE-nodes are distributed equidistantly on the free boundary. The necessary integration, which determines the length of the free boundary, is carried out numerically [44].

At the beginning of the optimization procedure a coarse discretization is used. This means a rough approximation of the stress strain field, but allows a large variation of the free boundary without net deterioration. Successively, the number of FE-nodes is increased during optimization. If no further optimization success can be achieved, the number of control nodes of the B-spline is increased.

3.3.3 Sensitivity Analysis

Besides the values of the cost function and the constraints SQP demands the values of the gradients of the cost function and the constraints with respect to the design variables. This is called the sensitivity analysis.

With the chosen transformation of the cost function (Eq. 3.45) it is trivial to obtain its gradient:

$$\nabla f(\mathbf{t}) = (0, 0, \dots, 1)^T, \quad (3.67)$$

with

$$\begin{aligned} \mathbf{t} &= (X_1, X_2, \dots, X_n, Y_1, Y_2, \dots, Y_n, \beta)^T && \text{in the case of node coordinates as design variables and} \\ \mathbf{t} &= (d_1, d_2, \dots, d_n, \beta)^T && \text{in the case of de-Boor ordinates.} \end{aligned}$$

The gradients of the necessary additional stress constraints (Eq. 3.44) are approximated by finite differences:

$$\frac{\partial g_i}{\partial t_j} \approx \frac{\Delta \sigma_{eq}^i}{\Delta t_j}. \quad (3.68)$$

All of the other gradients are derived analytically. As an example for the gradients of the constraints in the following subsection, at first the gradients of the manufacturing constraints are determined with respect to the node coordinates. Next comes an explanation of which modifications are necessary, if B-splines are used instead of the node coordinates to describe the free boundary.

The derivative of any of the geometrical constraints with respect to the additional design variable is zero.

Gradients of Manufacturing Constraint with Respect to Node Coordinates

The gradients of the local curvature radius R_i (see also Eqs. 3.52-3.54) do not vanish only in case the derivative is done with respect to the last (X_{i-1}, Y_{i-1}) , the actual (X_i, Y_i) or the next (X_{i+1}, Y_{i+1}) node coordinates. It makes no difference if the actual curvature radius is determined as the difference between the center and the node $i \Leftrightarrow 1$, i or $i + 1$ (see Fig. 3.5) so in the code always the coordinates fitting to the actual design variable are used. The following expressions result:

$$\frac{\partial R_i}{\partial x_k} = \frac{(Z_1 \Leftrightarrow N x_k) (N Z_1' \Leftrightarrow Z_1 N' \Leftrightarrow N^2) + (Z_2 \Leftrightarrow N y_k) (N Z_2' \Leftrightarrow Z_2 N')}{N^3 R_i} \quad (3.69)$$

$$\text{with } \iota = \frac{\partial}{\partial x_k} \text{ where } k \in (i \Leftrightarrow 1, i, i + 1),$$

and

$$\frac{\partial R_i}{\partial y_k} = \frac{(Z_1 \Leftrightarrow N x_k) (N Z_1' \Leftrightarrow Z_1 N') + (Z_2 \Leftrightarrow N y_k) (N Z_2' \Leftrightarrow Z_2 N' \Leftrightarrow N^2)}{N^3 R_i}, \quad (3.70)$$

$$\text{with } \iota = \frac{\partial}{\partial y_k} \text{ where } k \in (i \Leftrightarrow 1, i, i + 1).$$

The used abbreviations have the following meanings:

$$\frac{\partial Z_1}{\partial x_{i-1}} = 2x_{i-1} (y_{i+1} \Leftrightarrow y_i), \quad \frac{\partial Z_1}{\partial x_i} = 2x_i (y_{i-1} \Leftrightarrow y_{i+1}), \quad \frac{\partial Z_1}{\partial x_{i+1}} = 2x_{i+1} (y_i \Leftrightarrow y_{i-1}),$$

$$\frac{\partial Z_1}{\partial y_{i-1}} = x_i^2 \Leftrightarrow x_{i+1}^2 \Leftrightarrow y_{i+1}^2 \Leftrightarrow y_i^2 + 2y_{i-1} (y_{i+1} \Leftrightarrow y_i),$$

$$\frac{\partial Z_1}{\partial y_i} = \Leftrightarrow x_{i-1}^2 + x_{i+1}^2 + y_{i+1}^2 \Leftrightarrow y_{i-1}^2 + 2y_i (y_{i-1} \Leftrightarrow y_{i+1}),$$

$$\frac{\partial Z_1}{\partial y_{i+1}} = x_{i-1}^2 \Leftrightarrow x_i^2 \Leftrightarrow y_i^2 + y_{i-1}^2 + 2y_{i+1} (y_i \Leftrightarrow y_{i-1}),$$

$$\frac{\partial Z_2}{\partial x_{i-1}} = \Leftrightarrow x_i^2 + x_{i+1}^2 + 2x_{i-1} (x_i \Leftrightarrow x_{i+1}) + (y_{i+1}^2 \Leftrightarrow y_i^2),$$

$$\frac{\partial Z_2}{\partial x_i} = x_{i-1}^2 \Leftrightarrow x_{i+1}^2 + 2x_i (x_{i+1} \Leftrightarrow x_{i-1}) + (y_{i-1}^2 \Leftrightarrow y_{i+1}^2),$$

$$\frac{\partial Z_2}{\partial x_{i+1}} = x_i^2 \Leftrightarrow x_{i-1}^2 + 2x_{i+1} (x_{i-1} \Leftrightarrow x_i) + (y_i^2 \Leftrightarrow y_{i-1}^2),$$

$$\begin{aligned}
\frac{\partial Z_2}{\partial y_{i-1}} &= 2y_{i-1} (x_i \Leftrightarrow x_{i+1}), & \frac{\partial Z_2}{\partial y_i} &= 2y_i (x_{i+1} \Leftrightarrow x_{i-1}), & \frac{\partial Z_2}{\partial y_{i+1}} &= 2y_{i+1} (x_{i-1} \Leftrightarrow x_i), \\
\frac{\partial N}{\partial x_{i-1}} &= 2 (y_{i+1} \Leftrightarrow y_i), & \frac{\partial N}{\partial x_i} &= 2 (y_{i-1} \Leftrightarrow y_{i+1}), & \frac{\partial N}{\partial x_{i+1}} &= 2 (y_i \Leftrightarrow y_{i-1}), \\
\frac{\partial N}{\partial y_{i-1}} &= 2 (x_i \Leftrightarrow x_{i+1}), & \frac{\partial N}{\partial y_i} &= 2 (x_{i+1} \Leftrightarrow x_{i-1}), & \frac{\partial N}{\partial y_{i+1}} &= 2 (x_{i-1} \Leftrightarrow x_i).
\end{aligned}$$

Special care was taken if $N = 0 \Leftrightarrow R_i = \infty$. More details concerning the coding can be found in [44].

Gradients of Manufacturing Constraint with Respect to de-Boor Ordinates

In principal there are two possibilities to determine the manufacturing constraint with respect to a B-spline description of the free boundary. At first it is possible to use the description based on the node coordinates introduced above. Besides this there is also the possibility to use the analytical expression for the curvature:

$$\frac{d^2 s(u)}{d u^2} = s''(u). \quad (3.71)$$

This gives the following expression for the curvature radius:

$$\rho = \frac{(1 + s'^2(u))^{\frac{3}{2}}}{s''(u)}. \quad (3.72)$$

The manufacturing constraint can be formulated by:

$$\rho \Leftrightarrow R_{min} \geq 0, \quad u \in [u_2, u_{L+2}]. \quad (3.73)$$

In this work the first approach using three adjacent nodes on the free boundary is used further on. For the gradient calculation the chain rule has to be adopted. It has to be pointed out that the position of the x -coordinate of the nodes is fixed during one optimization cycle:

$$\frac{\partial g_j}{\partial d_k} = \frac{\partial g_j}{\partial y_{i-1}} \frac{\partial y_{i-1}}{\partial d_k} + \frac{\partial g_j}{\partial y_i} \frac{\partial y_i}{\partial d_k} + \frac{\partial g_j}{\partial y_{i+1}} \frac{\partial y_{i+1}}{\partial d_k}. \quad (3.74)$$

As mentioned above the basis function $N_i^3(u)$ are defined only over $u \in [u_{i-1}, u_{i+3}]$. For $u = x_l$ only four partial derivatives ($\partial y_l / \partial d_k = \partial s(x_l) / \partial d_k$) will not vanish:

$$\frac{\partial s(u)}{\partial d_{i-2}} = \frac{(u_{i+1} \Leftrightarrow u)^3}{(u_{i+1} \Leftrightarrow u_{i-2})(u_{i+1} \Leftrightarrow u_{i-1})(u_{i+1} \Leftrightarrow u_i)},$$

$$\begin{aligned}
\frac{\partial s(u)}{\partial d_{i-1}} &= \frac{(u_{i+1} \Leftrightarrow u)^2 (u \Leftrightarrow u_{i-2})}{(u_{i+1} \Leftrightarrow u_{i-2})(u_{i+1} \Leftrightarrow u_{i-1})(u_{i+1} \Leftrightarrow u_i)} \\
&\quad + \frac{u_{i+2} \Leftrightarrow u}{u_{i+2} \Leftrightarrow u_{i-1}} \left(\frac{u \Leftrightarrow u_{i-1}}{u_{i+1} \Leftrightarrow u_{i-1}} \frac{u_{i+1} \Leftrightarrow u}{u_{i+1} \Leftrightarrow u_i} + \frac{u_{i+2} \Leftrightarrow u}{u_{i+2} \Leftrightarrow u_i} \frac{u \Leftrightarrow u_i}{u_{i+1} \Leftrightarrow u_i} \right), \\
\frac{\partial s(u)}{\partial d_i} &= \frac{(u \Leftrightarrow u_i)^2 (u_{i+3} \Leftrightarrow u)}{(u_{i+3} \Leftrightarrow u_i)(u_{i+2} \Leftrightarrow u_i)(u_{i+1} \Leftrightarrow u_i)} \\
&\quad + \frac{u \Leftrightarrow u_{i-1}}{u_{i+2} \Leftrightarrow u_{i-1}} \left(\frac{u \Leftrightarrow u_{i-1}}{u_{i+1} \Leftrightarrow u_{i-1}} \frac{u_{i+1} \Leftrightarrow u}{u_{i+1} \Leftrightarrow u_i} + \frac{u_{i+2} \Leftrightarrow u}{u_{i+2} \Leftrightarrow u_i} \frac{u \Leftrightarrow u_i}{u_{i+1} \Leftrightarrow u_i} \right), \\
\frac{\partial s(u)}{\partial d_{i+1}} &= \frac{(u \Leftrightarrow u_i)^3}{(u_{i+3} \Leftrightarrow u_i)(u_{i+2} \Leftrightarrow u_i)(u_{i+1} \Leftrightarrow u_i)}, \\
&\quad \forall u \in [u_i, u_{i+1}), \tag{3.75}
\end{aligned}$$

where

$$d_k \in \{d_1, d_2, \dots, d_{L+1}\}, d_0 \text{ and } d_{L+2} \text{ are fixed.}$$

Keeping in mind that the x -coordinates of the nodes and the node sequence is constant during one optimization slope, it can be seen that all expressions in Eq. 3.75 are constant. For an efficient algorithm it is possible to calculate these expressions once before the optimization slope is started. Then the gradient calculation is reduced to the determination of the derivatives $\partial g_j / \partial y_l$ and the scalar product (Eq. 3.74) during the optimization slope takes place.

Chapter 4

Damage Mechanics

Material deterioration is an irreversible process; during this damage process the entropy is increasing.

At a microscale level damage is caused by the accumulated deterioration due to microstresses in the neighborhood of defects, interfaces and by breaking of bonds. On a meso-scale level, the level of the so called representative volume element, damage is connected with the growth of microcracks and microvoids which initiate the final macroscopic crack. At a macroscale it is the growth of this macroscopic crack. The two first stages may be studied by the use of a damage variable. The third stage is usually studied applying fracture mechanics (e.g. *Paris law Eq. 2.1*).

4.1 Introduction to Damage Mechanics

Kachanov was the first, who introduced in 1958 a continuous damage variable describing creep of a metal under uniaxial loading [48]. This concept was taken up again in the seventies especially in France (*Chaboche & Lemaitre*), in Sweden (*Hult*), in England (*Leckie*) and Japan (*Murakami*). The concept was extended to ductile failure and to fatigue. Nowadays the *Gurson* model has achieved a wide application particular for ductile failure. There are only a few papers concerning a description of fatigue with this damage mechanics concept. Most of them are dealing with LCF, in this case there is ductile damage [20, 21, 94, 95]. HCF is more interesting for shape optimization because most engineering parts are designed for a long or infinite lifetime. In HCF there is quasi brittle damage [56, 57]. This means the structure behavior is elastic at a mesoscale, but at a microscale highly localized there is some weakness of the material (inclusions, defects)

with elasto-plastic behavior carrying damage.

After a short introduction in the damage mechanics concept the main interest will be concentrated on the modellization of this quasi brittle behavior.

4.1.1 Introduction of a Damage Variable

Definition of a Representative Volume Element

Continuum mechanics deals with quantities defined for the mathematical point. From a physical point of view this means some kind of homogenization in a certain volume. This Representative Volume Element (RVE) must be small enough to avoid smoothing of high gradients and large enough to represent an average of the microprocesses. Certainly the size of the RVE will depend on the chosen material. Below, the magnitude of the characteristic length for a RVE (proposed as a quader) is given for some materials:

- metals & ceramics: $(0.1mm)^3$,
- polymers & composites: $(1mm)^3$,
- wood: $(10mm)^3$ and
- concrete: $(100mm)^3$.

Definition of an Isotropic Damage Variable

Consider a damaged part with a RVE in point M orientated by a plane with normal \vec{n} and abscissa x (see Fig. 4.1). δS is the area of intersection of the considered plane with the RVE. δS_{Dx} is the effective area of intersections of all microcracks and microcavities in δS . The damage value $D(M, \vec{n}, x)$ attached to the point M , the direction \vec{n} and the abscissa x is defined as:

$$D(M, \vec{n}, x) = \frac{\delta S_{Dx}}{\delta S}. \quad (4.1)$$

The failure of the RVE will be caused by the most damaged intersection area:

$$D(M, \vec{n}) = \max_x D(M, \vec{n}, x) = \frac{\delta S_D}{\delta S}, \quad (4.2)$$

where

δS_D : is the most damaged intersection area.

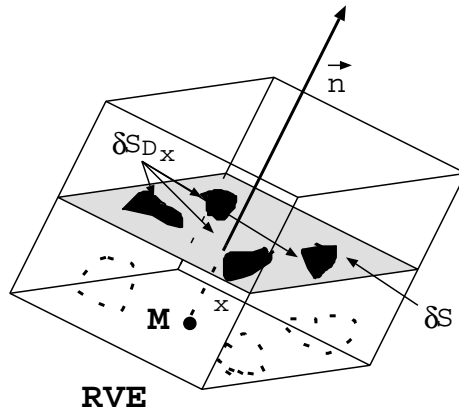


Figure 4.1: Definition of the damage variable

From the above definition it is found that

$$0 \leq D \leq 1. \quad (4.3)$$

$D = 0$ means the material in the RVE is undamaged. $D = 1$ means the RVE is broken into two parts.

Eq. 4.2 can be used as definition for D in a general case. If microcracks and cavities are uniformly distributed the damage variable will not depend on the orientation of \vec{n} . This is the case of isotropic damage. We will restrict ourselves to the case of isotropic damage in this work. Only some remarks will be outlined for anisotropic damage in 4.4.1.

4.1.2 Concept of Effective Stress

The introduced damage variable leads directly to the concept of effective stress. Let us first consider the case of uniaxial tension: For an isotropic damaged material the cross section is no longer S but becomes $S \Leftrightarrow S_D$. So the usual stress:

$$\sigma = \frac{F}{S} \quad \text{is replaced by the effective stress:} \quad \tilde{\sigma} = \frac{F}{S \Leftrightarrow S_D} = \frac{\sigma}{1 \Leftrightarrow D}. \quad (4.4)$$

It is obvious that

$$\tilde{\sigma} \geq \sigma. \quad (4.5)$$

For the virgin material $\tilde{\sigma} = \sigma$ and in the moment of fracture $\tilde{\sigma} \rightarrow \infty$.

In the case of multiaxial isotropic damage neither δS nor δS_D depend on the orientation \vec{n} so the whole effective stress tensor can be written as:

$$\tilde{\sigma} = \frac{\sigma}{1 \Leftrightarrow D}. \quad (4.6)$$

The damaged intersection area δS_D has to be taken as effective area. For example it should take into account the concentration of microstresses (δS_D has to be taken smaller

than the area of the intersections of the microcracks, see [56]), or in a tension compression test in the phase of compression δS_D is reduced or even zero, because the microcracks are closed in compression. Often a crack closure parameter is introduced in this case:

$$\delta \tilde{S}_D = \begin{cases} \delta S_D & \text{if } \sigma \geq 0, \\ h\delta S_D, & 0 \geq h \geq 1 \quad \text{else.} \end{cases} \quad (4.7)$$

where

h : is the crack closure parameter.

4.1.3 Strain Equivalence Principle

We like to avoid the micromechanical analysis for each type of defect and each type of damage mechanism. Therefore, a thermodynamical description is used on a mesoscale postulating the following principle (*Lemaitre 1971*):

“Any strain constitutive equation for a damaged material may be derived in the same way as for a virgin material except that the usual stress is replaced by the effective stress”.

This statement is a principle because it has been proved only in some particular cases of damage by the use of homogenization techniques.

It is a local approach. This means on a microscale, that the strains in a microvolume element do not depend on the neighboring microvolume element containing a microcrack.

4.2 Thermodynamical Description

In this section two potentials are introduced within the framework of “State Kinetic Coupling Theory” [58].

It is an important and difficult problem to do the right choice for the explicit formulation of the two potentials particular for the potential of dissipation. Thermodynamics will give some general guidelines and some restriction, but only basic experiments and micromechanics can determine details.

4.2.1 State Potential

To characterize the material, a state potential is introduced. Here, the specific Helmholtz free energy (ψ) is chosen which is a scalar function of all the state variables (V_I). ψ is a convex function of the state variables mentioned below. In the case of thermoelasticity it is additionally a concave function in temperature T containing the origin. The link between the state variables and the associated variables (A_I) is given by the state laws:

$$A_I = \frac{\partial \rho \psi}{\partial V_I}. \quad (4.8)$$

with

ρ : is the density.

In the following table the state variables and the linked associated variables (or dual variables) are given for isothermal elasto-plastic behavior with hardening and damage:

	STATE VARIABLES	ASSOCIATED VARIABLES
ELASTICITY	$\boldsymbol{\varepsilon}$ (deformation)	$\boldsymbol{\sigma}$ (stress)
PLASTICITY	$\boldsymbol{\varepsilon}^p$ (plastic strain)	$-\boldsymbol{\sigma}$ (stress)
ISOTROPIC HARDENING	r (accumulated plastic strain)	R (isotropic strain hardening)
KINEMATIC HARDENING	$\boldsymbol{\alpha}$ (back strain tensor)	\mathbf{X} (kinematic hardening, back stress)
DEGENERATION	D (damage)	$\Leftrightarrow Y$ (damage energy release rate)

Remark: In ψ instead of $\boldsymbol{\varepsilon}$ and $\boldsymbol{\varepsilon}^p$ only the difference of both ($\boldsymbol{\varepsilon}^e = \boldsymbol{\varepsilon} \Leftrightarrow \boldsymbol{\varepsilon}^p$) is needed to describe the deformation state. With Eq. 4.8 and the chain rule it is found that the associated variable to $\boldsymbol{\varepsilon}^p$ is therefore $\Leftrightarrow \boldsymbol{\sigma}$.

It is usual to divide the state variables into observables and internal variables. In the considered case the strain tensor is an observable, all other state variables cannot be

measured directly, so they are internal variables. A second observable in the case of thermoelasticity is the temperature (T).

To determine the explicit expression for ψ it is necessary to know the state coupling. A state coupling exists between two mechanisms I and J corresponding to the state variables V_I and V_J if a variation of V_I implies a modification of A_J (and vice versa). Since $A_J = \partial\rho\psi/\partial V_J$ a state coupling exists if:

$$\frac{\partial A_J}{\partial V_I} = \frac{\partial^2 \rho\psi}{\partial V_I \partial V_J} \neq 0. \quad (4.9)$$

If there is no coupling between I and J the potential can be split into two additive terms:

$$\psi(\mathbf{V}) = \psi_1(V_I, \mathbf{V}_K) + \psi_2(V_J, \mathbf{V}_K), \quad (4.10)$$

with: $K = 1..N$ and $K \neq I, K \neq J$.

For example as the development of slips has no influence on the interaction between the atoms, the elastic behavior is not coupled with the plastic behavior:

$$\frac{\partial^2 \psi}{\partial \boldsymbol{\varepsilon}^e \partial r} = 0 \quad \text{and} \quad \frac{\partial^2 \psi}{\partial \boldsymbol{\varepsilon}^e \partial \boldsymbol{\alpha}} = 0. \quad (4.11)$$

The development of decohesion certainly has an influence on the interaction between the atoms. The elastic behavior is coupled with the damage:

$$\frac{\partial^2 \psi}{\partial \boldsymbol{\varepsilon}^e \partial D} \neq 0. \quad (4.12)$$

The following table gives an impression of the couplings (1) and uncouplings (0) for a 2024 aluminium alloy [58]:

	$\boldsymbol{\varepsilon}-\boldsymbol{\varepsilon}^p$	$\boldsymbol{\alpha}$	r	D
$\boldsymbol{\varepsilon} \leftrightarrow \boldsymbol{\varepsilon}^p$	-	0	0	1
$\boldsymbol{\alpha}$	0	-	0	0
r	0	0	-	0
D	1	0	0	-

From the table above and the drawn considerations the following general expression for the Helmholtz free energy is derived:

$$\psi = \psi_1(\boldsymbol{\varepsilon}^e, D) + \psi_2(\boldsymbol{\alpha}) + \psi_3(r). \quad (4.13)$$

If we assume linear elasticity and small deformations Eq. 4.13 can be rewritten in a more precise form:

$$\psi = \frac{1}{\rho} \left[\frac{1}{2} a_{ijkl} \varepsilon_{ij}^e \varepsilon_{kl}^e \right] (1 \Leftrightarrow D) + \text{terms for plasticity} \quad (4.14)$$

where

a_{ijkl} : is the fourth order elasticity stiffness tensor.

With the further assumptions of homogeneous isotropic material and classical expressions for isotropic and kinematic hardening the following expression is deduced:

$$\psi = \frac{1}{\rho} \left[\frac{E}{2} \left[\frac{\varepsilon_{ij}^e \varepsilon_{ij}^e}{1 + \nu} + \frac{\nu \varepsilon_{kk}^e{}^2}{(1 + \nu)(1 \Leftrightarrow 2\nu)} \right] (1 \Leftrightarrow D) + R_\infty \left[r + \frac{1}{b} e^{-br} \right] + \frac{X_\infty \gamma}{3} \alpha_{ij} \alpha_{ij} \right] \quad (4.15)$$

where

$b, R_\infty, \gamma, X_\infty$: are the material parameters for isotropic and kinematic hardening.

As a proof for the formulation of ψ the state law (Eq. 4.8) is used e.g. to derive the law of elasticity:

$$\sigma_{ij} = \rho \frac{\partial \psi}{\partial \varepsilon_{ij}^e} = E(1 \Leftrightarrow D) \left[\frac{\varepsilon_{ij}^e}{1 + \nu} + \frac{\nu \varepsilon_{kk}^e \delta_{ij}}{(1 + \nu)(1 \Leftrightarrow 2\nu)} \right], \quad (4.16)$$

or:

$$\varepsilon_{ij}^e = \frac{1 + \nu}{E} \tilde{\sigma}_{ij} \Leftrightarrow \frac{\nu}{E} \tilde{\sigma}_{kk} \delta_{ij}. \quad (4.17)$$

The associated variable ($\Leftrightarrow Y$) to the damage variable (D) is derived in the same way:

$$\Leftrightarrow Y = \rho \frac{\partial \psi}{\partial D} = \Leftrightarrow \frac{E}{2} \left[\frac{\varepsilon_{ij}^e \varepsilon_{ij}^e}{1 + \nu} + \frac{\nu \varepsilon_{kk}^e{}^2}{(1 + \nu)(1 \Leftrightarrow 2\nu)} \right]. \quad (4.18)$$

Y is called the strain energy density release rate. This name is justified by the following considerations:

w_e is the elastic strain energy density. With the help of Eq. 4.14 and under consideration that $D = \text{const.}$, w_e is derived as:

$$w_e = \int \sigma_{ij} d\varepsilon_{ij}^e = \frac{1}{2} a_{ijkl} \varepsilon_{ij}^e \varepsilon_{kl}^e (1 \Leftrightarrow D) = Y(1 \Leftrightarrow D). \quad (4.19)$$

Now, the loss in elastic strain energy for constant stress is calculated:

$$d\sigma_{ij} = 0 = a_{ijkl} [(1 \Leftrightarrow D) d\varepsilon_{kl}^e \Leftrightarrow \varepsilon_{kl}^e dD]. \quad (4.20)$$

Eq. 4.20 is transformed to:

$$d\varepsilon_{kl}^e = \varepsilon_{kl}^e \frac{dD}{1 \Leftrightarrow D}. \quad (4.21)$$

Formulation of the increment of elastic strain energy density with the restriction to constant stress gives:

$$dw_e|_{\sigma=const} = \sigma_{ij} d\varepsilon_{ij}^e = \sigma_{ij} \varepsilon_{ij}^e \frac{dD}{1 \Leftrightarrow D} = a_{ijkl} \varepsilon_{ij}^e (1 \Leftrightarrow D) \varepsilon_{kl}^e \frac{dD}{1 \Leftrightarrow D}. \quad (4.22)$$

or:

$$\left. \frac{dw_e}{dD} \right|_{\sigma=const} = a_{ijkl} \varepsilon_{ij}^e \varepsilon_{kl}^e. \quad (4.23)$$

So, in conclusion:

$$Y = \frac{1}{2} \left. \frac{dw_e}{dD} \right|_{\sigma=const}. \quad (4.24)$$

It can be seen from Eq. 4.24 that Y is determined by the loss of stiffness of a RVE in which the damage occurred.

An important conclusion of state coupling theory is, that the internal variables which are difficult or even impossible to measure directly, can now be determined by measuring the observables. For example the damage variable (D) can be measured by determining the effective decreasing Young's modulus ($\tilde{E} = (1 \Leftrightarrow D)E$, see Fig. 4.3) instead of the difficult and time intensive microscopic observations.

4.2.2 Potential of Dissipation

To complete the constitutive equations, the evolution laws of the internal variables must be added to the state laws. The theory of thermodynamics of irreversible processes gives a guideline to obtain the evolution laws.

To satisfy the second principle of thermodynamics we start with the *Clausius* \Leftrightarrow *Duhem* inequality:

$$\sigma_{ij} \dot{\varepsilon}_{ij} \Leftrightarrow \rho(\dot{\psi} + s\dot{T} \Leftrightarrow q_i \frac{T_{,i}}{T}) \geq 0, \quad (4.25)$$

where

\mathbf{q} : is the heat flux vector associated to the temperature gradient ($T_{,i}$).

We restrict ourselves to isothermal processes.

The rate of the Helmholtz free energy is attained by differentiation with respect to the state variables:

$$\dot{\psi} = \frac{\partial \psi}{\partial \varepsilon_{ij}^e} \dot{\varepsilon}_{ij}^e + \frac{\partial \psi}{\partial r} \dot{r} + \frac{\partial \psi}{\partial \alpha_{ij}} \dot{\alpha}_{ij} + \frac{\partial \psi}{\partial D} \dot{D}. \quad (4.26)$$

Introducing the associated variables and $\dot{\varepsilon}_{ij} = \dot{\varepsilon}_{ij}^e + \dot{\varepsilon}_{ij}^p$ leads to:

$$\text{tr}(\boldsymbol{\sigma} \dot{\boldsymbol{\varepsilon}}^p) \Leftrightarrow R \dot{r} \Leftrightarrow \text{tr}(\mathbf{X} \dot{\boldsymbol{\alpha}}) + Y \dot{D} \geq 0, \quad (4.27)$$

or in a short form:

$$\mathbf{B} \dot{\mathbf{U}} \geq 0, \quad (4.28)$$

where

$\dot{\mathbf{U}}$: is the vector of flux variables ($\dot{\boldsymbol{\varepsilon}}^p, \dot{r}, \dot{\boldsymbol{\alpha}}, \dot{D}$) and
 \mathbf{B} : is the vector of force variables ($\boldsymbol{\sigma}, R, \mathbf{X}, Y$).

The product in Eq. 4.28 is positive if a pseudo potential of dissipation ϕ with some properties of convexity is introduced [99]. The flux variables are derived by differentiation of this potential:

$$\dot{\mathbf{U}} = \frac{\partial \phi}{\partial \mathbf{B}}. \quad (4.29)$$

For isothermal processes the plastic dissipation is negligible, so the following expression results:

$$Y \dot{D} \geq 0. \quad (4.30)$$

Y is a positive quadratic function, so the damage rate \dot{D} must be a nonnegative function. This means, it can only be used to describe material deterioration and not be applied to describe a recovery of strength of the material.

The potential of dissipation is introduced as function of the force variables. Nevertheless the state variables can be introduced as parameters in this function:

$$\phi = \phi(\mathbf{B}, \mathbf{V}). \quad (4.31)$$

There is a kinetic coupling of mechanism I on J if a variation of V_I leads to an modification of the rate of U_J :

$$\text{with: } \dot{U}_J = \frac{\partial \phi}{\partial B_J} \quad \text{there is a coupling if: } \frac{\partial \dot{U}_J}{\partial V_I} \neq 0. \quad (4.32)$$

If ϕ is out of \mathcal{C}^2 this is equivalent to:

$$\frac{\partial^2 \phi}{\partial B_J \partial V_I} \neq 0. \quad (4.33)$$

The kinetic coupling for an aluminium alloy 2024 [58] can be found in the table below (This table summarizes the kinetic couplings for most engineering materials.):

on\of	$\boldsymbol{\varepsilon}^e$	$\boldsymbol{\varepsilon}^p$	$\boldsymbol{\alpha}$	r	D
$\boldsymbol{\varepsilon}^p$	0	0	0	0	1
$\boldsymbol{\alpha}$	0	0	0	0	1
r	0	0	0	0	1
D	0	0	0	0	0

There is a kinetic coupling from damage on the mechanism of plasticity assumed, as it is well known that with increasing material degeneration the yield stress is decreasing and the plastic strain rate is increasing. The coupling is done by replacing the stress by the effective stress in the potential of dissipation.

As an example, the potential of dissipation for time-independent plasticity coupled with damage is given below:

$$\phi = \phi_p(\boldsymbol{\sigma}, \mathbf{X}, R, D) + \phi_D(Y) = \phi_P(\tilde{\boldsymbol{\sigma}}, \mathbf{X}, R) + \phi_D(Y). \quad (4.34)$$

If the von Mises criterion is used for definition of the yield surface (the kinetic coupling is found to act also only on the deviatoric part of the stress tensor) together with kinematic and isotropic hardening, the following classical expression is found for the first part of the potential of dissipation:

$$\phi_P = \left(\tilde{\boldsymbol{\sigma}}^D \Leftrightarrow \mathbf{X}^D \right)_{eq} \Leftrightarrow R \Leftrightarrow \sigma_y. \quad (4.35)$$

The flux variables are derived using the normality rule:

$$\dot{\varepsilon}_{ij}^p = \dot{\lambda} \frac{\partial f}{\partial \sigma_{ij}} = \frac{3}{2} \frac{\tilde{\sigma}_{ij}^D \Leftrightarrow X_{ij}^D}{(\boldsymbol{\sigma} \Leftrightarrow \mathbf{X})_{eq}} \frac{\dot{\lambda}}{1 \Leftrightarrow D}, \quad (4.36)$$

$$\Leftrightarrow \dot{\boldsymbol{\alpha}} = \dot{\lambda} \frac{\partial f}{\partial \mathbf{X}}, \quad (4.37)$$

$$\Leftrightarrow \dot{r} = \dot{\lambda} \frac{\partial f}{\partial R} = \Leftrightarrow \dot{1}, \quad (4.38)$$

where

- f : is the yield function (here associated plasticity is assumed $\Rightarrow \phi_P = f$) and
- λ : is the plastic multiplier.

An identity is found by introducing the accumulated plastic strain, defined by its flux:

$$\dot{p} = \left(\frac{2}{3} \dot{\varepsilon}_{ij}^p \dot{\varepsilon}_{ij}^p \right)^{\frac{1}{2}}, \quad (4.39)$$

with Eq. 4.36 we obtain:

$$\dot{p} = (1 \Leftrightarrow D) \dot{\lambda}. \quad (4.40)$$

Like Hooke's law for elasticity or Prandtl-Reuss's law in plasticity, a general expression for the potential of dissipation for almost all materials is desired to model damage evolution. This expression must include the following properties:

- The considerations above show that the main causal variable for damage is the strain energy release rate (Y). In Y triaxiality which has a large influence on damage behavior will be considered (see next subsection).

Remark: For notch problems, which were covered in the beginning of Chapter 3, we have seen that the point with maximum stress is located in most cases on the notch surface. In the here considered 2D case, $R_V \equiv 1$ for the notch surface on a mesoscale as can be seen in Section 4.2.3.

- Damage is always connected with irreversible straining (accumulated plastic strain Eq. 4.40) either on a meso- or a microlevel. This is already taken into account by the plastic multiplier:

$$\dot{D} = \dot{\lambda} \frac{\partial f_D}{\partial Y} = (1 \Leftrightarrow D) \frac{\partial f_D}{\partial Y} \dot{p}. \quad (4.41)$$

The accumulated plastic strain rate \dot{p} is always greater than zero. Thus, the irreversibility of damage is guaranteed.

- It can be shown that (see [56]) the flux of D is proportional to Y in a general meaning (In A.2 a micromechanical model for fatigue crack growth using a homogenization technique is found):

$$\dot{D} \sim Y \quad \Rightarrow \quad \phi_D \sim Y^2. \quad (4.42)$$

- Experiments often show, that damage occurs if the point of σ_u is passed in an uniaxial tension test (ε_{pD}). In multiaxial loading this threshold has to be transferred to a threshold in accumulated plastic strain (p_D). This is inserted into the model introducing a step function:

$$\Theta(p \Leftrightarrow p_D) = \begin{cases} 0 & \text{if } p < p_D \text{ and} \\ 1 & \text{if } p \geq p_D. \end{cases} \quad (4.43)$$

In conclusion the following expression is deduced:

$$\phi_D \sim Y^2 \Theta(p \Leftrightarrow p_D). \quad (4.44)$$

In addition the factor $[2S(1 \Leftrightarrow D)]^{-1}$ is introduced. S , is called damage strength, it is a material constant. The introduction of $(1 \Leftrightarrow D)^{-1}$ is necessary, because experiments show a nondecreasing damage rate if \dot{p} and Y are constant. Combining the last considerations, the following expression results:

$$\phi_D = \frac{Y^2}{2S(1 \Leftrightarrow D)} \Theta(p \Leftrightarrow p_D) \quad \rightarrow \quad \dot{D} = \frac{Y}{S} \dot{p} \Theta(p \Leftrightarrow p_D). \quad (4.45)$$

4.2.3 Triaxiality and Damage Equivalent Stress

In this section according to the equivalent stress in plasticity a damage equivalent stress is formulated with the help of a triaxiality function.

At first w_e is split into two parts: the shear energy and the hydrostatic energy, corresponding to the deviatoric and the spherical part of the stress and strain tensors:

$$\sigma_{ij} = \sigma_{ij}^D + \sigma^H \delta_{ij} \quad \text{and} \quad \varepsilon_{ij}^e = \varepsilon_{ij}^{eD} + \varepsilon^{eH} \delta_{ij}, \quad (4.46)$$

where

$$\sigma^H = \frac{1}{3} \sigma_{kk} \quad \text{and} \quad \varepsilon^{eH} = \frac{1}{3} \varepsilon_{kk}^e,$$

and

$$w_e = \int \sigma_{ij} d\varepsilon_{ij}^e = \int \sigma_{ij}^D d\varepsilon_{ij}^{eD} + \int \delta_{ij} \delta_{ij} \sigma^H d\varepsilon^{eH}. \quad (4.47)$$

Hooke's law coupled with damage is also split in the deviatoric and the hydrostatic parts:

$$\varepsilon_{ij}^{eD} = \frac{1 + \nu}{E} \frac{\sigma_{ij}^D}{1 \Leftrightarrow D} \quad \text{and} \quad \varepsilon_{ij}^{eH} = \frac{1 \Leftrightarrow 2\nu}{E} \frac{\sigma^H}{1 \Leftrightarrow D}. \quad (4.48)$$

Inserting Eq. 4.48 in Eq. 4.47 leads to:

$$w_e = \frac{1}{2} \left(\frac{1 + \nu}{E} \frac{\sigma_{ij}^D \sigma_{ij}^D}{1 \Leftrightarrow D} + 3 \frac{1 \Leftrightarrow 2\nu}{E} \frac{\sigma^{H^2}}{1 \Leftrightarrow D} \right) \quad (4.49)$$

With the von Mises equivalent stress defined as:

$$\sigma_{eq} = \left(\frac{3}{2} \sigma_{ij}^D \sigma_{ij}^D \right)^{\frac{1}{2}}. \quad (4.50)$$

the following formula is derived for Y :

$$Y = \frac{w_e}{1 \Leftrightarrow D} = \frac{\sigma_{eq}^2}{2E(1 \Leftrightarrow D)^2} \left[\frac{2}{3} (1 + \nu) + 3(1 \Leftrightarrow 2\nu) \left(\frac{\sigma^H}{\sigma_{eq}} \right)^2 \right], \quad (4.51)$$

where

$$\frac{\sigma^H}{\sigma_{eq}}: \text{triaxiality ratio.}$$

The term in square brackets is called triaxiality function (R_V):

$$R_V = \frac{2}{3} (1 + \nu) + 3(1 \Leftrightarrow 2\nu) \left(\frac{\sigma^H}{\sigma_{eq}} \right)^2. \quad (4.52)$$

So, Eq. 4.51 can be rewritten in a short form:

$$Y = \frac{\tilde{\sigma}_{eq}^2}{2E} R_V. \quad (4.53)$$

Similar to the plastic equivalent stress a damage equivalent stress is now defined. It is a one-dimensional stress (σ^*) which causes for the same value of damage the same elastic strain energy as the three dimensional state of stress.

For the one-dimensional case there is:

$$[\sigma^*] = \begin{bmatrix} \sigma^* & 0 & 0 \\ 0 & 0 & 0 \\ 0 & 0 & 0 \end{bmatrix}, \quad \sigma^H = \frac{1}{3}\sigma^* \quad \text{and} \quad [\sigma^D] = \begin{bmatrix} \frac{2}{3}\sigma^* & 0 & 0 \\ 0 & \Leftrightarrow\frac{1}{3}\sigma^* & 0 \\ 0 & 0 & \Leftrightarrow\frac{1}{3}\sigma^* \end{bmatrix}. \quad (4.54)$$

The elastic strain energy is for this one-dimensional case:

$$w_e = \frac{\sigma^{*2}}{2E(1 \Leftrightarrow D)}. \quad (4.55)$$

Requiring the equality of strain energy density of the one-dimensional case (Eq. 4.55) and the three dimensional case (Eq. 4.51 and Eq. 4.53) determines the damage equivalent stress in the following form:

$$\sigma^* = \sigma_{eq} R_V^{\frac{1}{2}}. \quad (4.56)$$

The damage equivalent stress differs from the von Mises equivalent stress by the triaxiality function. Plasticity is connected with slips which are caused by shear stresses. There is no dependency on hydrostatic stresses observed. Damage is connected with debonding which is influenced by hydrostatic stress or triaxiality ratio ("triaxiality makes material brittle").

Triaxiality on the Notch Surface in 2D:

In Chapter 3 it was remarked, that for the considered notch problems the point of maximum stress is on the notch surface. On the free boundary of the notch surface there is only a one-dimensional state of stress tangential to the boundary in the 2D plane stress case. If an orthogonal coordinate system parallel to the direction of principal stress is chosen, only $\sigma_2 = \sigma_t$ does not vanish.

Introducing this in Eq. 4.52 determines the triaxiality function $R_V \equiv 1$ for all points on the free boundary.

In conclusion: For the 2D case it is outlined, that on a mesoscale:

$$\sigma_{eq} = \sigma^* \quad \forall \mathbf{X} \in \cdot, *. \quad (4.57)$$

4.3 Modelling Fatigue

Eq. 4.41 states a direct proportionality of the damage rate and the rate of accumulated plastic strain. This means, without plasticity there is no damage accumulation.

In Chapter 2 we found, that for HCF the structure will stay elastic on a macroscale and even on the mesoscale (=scale of the RVE).

Certainly there is a damage accumulation in HCF. The mentioned problem can be solved using a two scale model.

4.3.1 Two Scale Model

The fatigue model considered here was worked out by *Lemaitre* [55, 56, 57]. *Lemaitre* supposes a two scale model: an elastic matrix material with weaker inclusions suffering damage in it.

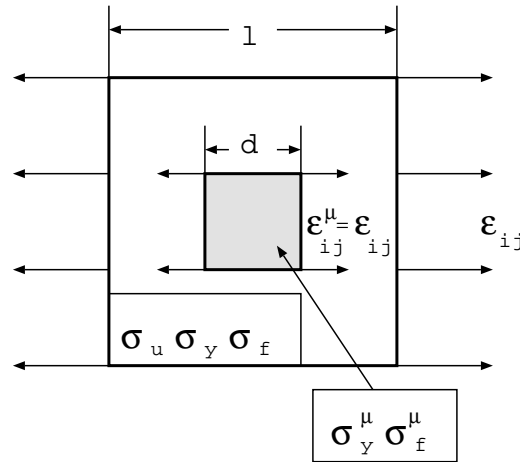


Figure 4.2: Two scale RVE.

The matrix material is characterized by its yield stress (σ_y), its ultimate stress (σ_u) and its fatigue limit ($\sigma_f < \sigma_y$).

The behavior of the inclusions is assumed elastic-perfect plastic with a yield stress (σ_y^μ , the superscript μ will always denote that the variable belongs to the inclusion.) set to the fatigue limit of the origin material ($\sigma_y^\mu = \sigma_f$).

The assumption of the simple elastic-perfect plastic behavior of the inclusions is justified, because damage always occurs after strain hardening has finished. Nevertheless in [55] the description of modelling the stress strain curve stepwise elastic-perfect plastic is given. In *Lemaitre's* work only the inclusions can suffer damage. This feature will be modified further on (see Section 4.3.4).

Below the fatigue limit of the material no damage occurs. In another assumption the fatigue limit of the inclusions is reduced in the same proportion as for the matrix material:

$$\frac{\sigma_f^\mu}{\sigma_y^\mu} = \frac{\sigma_f}{\sigma_y} \quad \Rightarrow \quad \sigma_f^\mu = \sigma_f \frac{\sigma_f}{\sigma_y}. \quad (4.58)$$

Lin-Taylor's strain compatibility hypothesis [91] - matrix and inclusion are equally strained - gives the bridge between the behavior of the matrix and the inclusion.

If the accumulated plastic strain has crossed its threshold, the kinetic damage law for the inclusion is:

$$\dot{D} = \frac{Y^\mu}{S} \dot{p}^\mu. \quad (4.59)$$

Damage accumulation of the inclusions will be solved numerically in Section 4.3.4. Here, with some reasonable approximations the microscopic functions Y^μ and \dot{p}^μ can be expressed as functions of variables at mesoscale. This will help to give some arguments for the discussion of the final results.

According to Lin-Taylor's hypothesis we assume the same strain rate for the inclusion and the matrix:

$$\dot{\boldsymbol{\varepsilon}} = \dot{\boldsymbol{\varepsilon}}^\mu. \quad (4.60)$$

The elastic strain of the inclusion can be neglected in comparison to the plastic strain. With this approximation the following relation is derived:

$$\dot{p}^\mu = \left(\frac{2}{3} \dot{\boldsymbol{\varepsilon}}^{p\mu} \dot{\boldsymbol{\varepsilon}}^{p\mu} \right)^{\frac{1}{2}} = \left(\frac{2}{3} \dot{\boldsymbol{\varepsilon}}^{\mu D} \dot{\boldsymbol{\varepsilon}}^{\mu D} \right)^{\frac{1}{2}} = \left(\frac{2}{3} \dot{\boldsymbol{\varepsilon}}^{D} \dot{\boldsymbol{\varepsilon}}^{D} \right)^{\frac{1}{2}} = \dot{\boldsymbol{\varepsilon}}_{eq}. \quad (4.61)$$

The strain energy density release rate for the inclusion can be rewritten with the help of the yield criterion formulated at the microscale:

$$\frac{\sigma_{eq}^\mu}{1 \Leftrightarrow D} = \sigma_y^\mu = \sigma_f \quad (4.62)$$

and the microscopic triaxiality function:

$$R_V^\mu = \frac{2}{3}(1 + \nu) + 3(1 \Leftrightarrow 2\nu) \left(\frac{\sigma_H^\mu}{\sigma_{eq}^\mu} \right)^2. \quad (4.63)$$

With respect to the last two equations the following expression is derived for the strain energy release rate (see Eq. 4.53):

$$Y^\mu = \frac{\sigma_f^2}{2E} \frac{2}{3}(1 + \nu) + 3(1 \Leftrightarrow 2\nu) \left(\frac{\sigma_H^\mu}{\sigma_{eq}^\mu} \right)^2. \quad (4.64)$$

The hydrostatic part of the stress tensor is related to the hydrostatic part of the elastic strain tensor at microscale by the following expression:

$$\sigma_H^\mu = \frac{E(1 \Leftrightarrow D)}{1 \Leftrightarrow 2\nu} \boldsymbol{\varepsilon}_H^{e\mu}. \quad (4.65)$$

$$\boldsymbol{\varepsilon}_H^{e\mu} = \boldsymbol{\varepsilon}_H \quad \text{since} \quad \boldsymbol{\varepsilon}^{e\mu} + \boldsymbol{\varepsilon}^{p\mu} = \boldsymbol{\varepsilon} \quad \text{and} \quad \text{tr}(\boldsymbol{\varepsilon}^{p\mu}) = 0.$$

Lemaitre supposes pure elasticity at mesoscale:

$$\boldsymbol{\varepsilon}_H = \frac{1 \Leftrightarrow 2\nu}{E} \sigma_H. \quad (4.66)$$

So, the following expressions result:

$$\sigma_H^\mu = (1 \Leftrightarrow D)\sigma_H \quad \text{and} \quad \frac{\sigma_H^\mu}{\sigma_{eq}^\mu} = \frac{\sigma_H}{\sigma_y}. \quad (4.67)$$

Finally, the following expression is found for the damage rate at microscale:

$$\dot{D}^\mu = \frac{\sigma_f^2}{2ES} \left[\frac{2}{3}(1 + \nu) + 3(1 \Leftrightarrow 2\nu) \left(\frac{\sigma_H}{\sigma_f} \right)^2 \right] \dot{\varepsilon}_{eq}. \quad (4.68)$$

4.3.2 Damage Threshold and Critical Damage

In this section a damage threshold (p_D) (see Section 4.2.2) is defined by comparison of the energy stored in a fatigue test with the energy of a one-dimensional tension test. If we look in the schematic tension diagram (Fig. 4.3), we notice a decreasing Young's modulus after the point of ultimate stress is passed, because damage takes place.

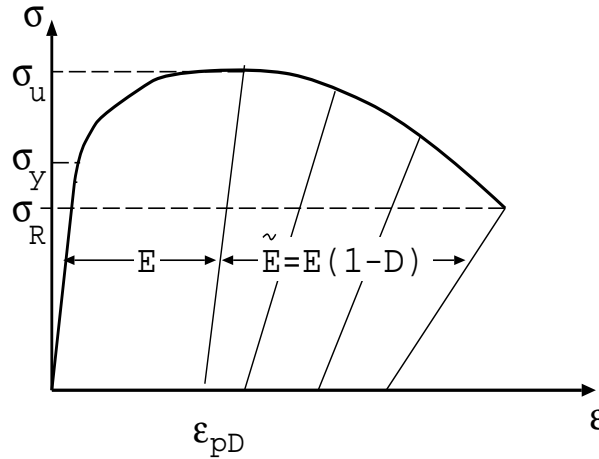


Figure 4.3: Schematic stress-strain diagram with unloadings

In a rough approximation the dissipative energy is:

$$w_D = (\sigma_u \Leftrightarrow \sigma_f)\varepsilon_{pD}. \quad (4.69)$$

This energy is compared with the energy stored in the inclusions. In the absence of damage the second principle of thermodynamics states, that the energy dissipated in heat is: $\sigma_f^\mu p^\mu$.

So, the stored energy is:

$$w_s = \int \sigma_{ij} d\varepsilon_{ij}^p \Leftrightarrow \sigma_f^\mu p^\mu. \quad (4.70)$$

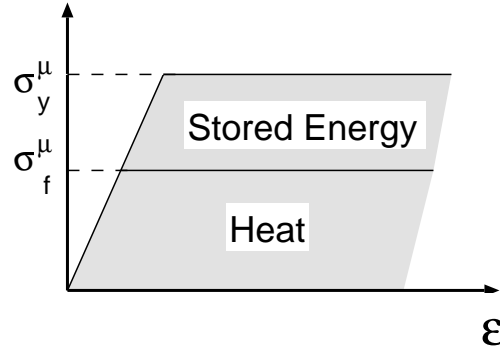


Figure 4.4: Energy stored in the inclusions.

Here only perfect plasticity is considered:

$$w_s = (\sigma_f \leftrightarrow \sigma_f^\mu) p^\mu. \quad (4.71)$$

Comparing Eq. 4.71 and Eq. 4.69 determines the threshold:

$$p_D^\mu = \frac{\sigma_u \leftrightarrow \sigma_f}{\sigma_y^\mu \leftrightarrow \sigma_f^\mu} \varepsilon_{pD} = \frac{\sigma_u \leftrightarrow \sigma_f}{\sigma_f \leftrightarrow \sigma_f^\mu} \varepsilon_{pD}. \quad (4.72)$$

The critical damage value corresponds to an instability. Often it can be related to the energy dissipated during the damage process:

$$\int_{D=0}^{D_C^\mu} Y^\mu dD^\mu = \text{constant at failure.} \quad (4.73)$$

Assuming a proportional loading (R_V^μ is constant in that case, see Appendix A.1) leads to:

$$\int_{D=0}^{D_C^\mu} Y dD^\mu = \int_{D=0}^{D_C^\mu} \frac{\sigma_f^2 R_V^\mu}{2E} dD^\mu = \frac{\sigma_f^2 R_V^\mu}{2E} D_C^\mu. \quad (4.74)$$

Again the uniaxial tension test is taken as reference:

$$\frac{\sigma_f^2 R_V^\mu}{2E} D_C^\mu = \frac{\sigma_u^2}{2E} D_{1C}. \quad (4.75)$$

D_{1C} : Critical damage value (one-dimensional reference).

Transforming Eq. 4.75 leads to the following expression for the critical damage value:

$$D_C^\mu = \frac{\sigma_u^2}{\sigma_f^2 R_V^\mu} D_{1C} \leq 1. \quad (4.76)$$

This critical damage is derived for microscale, but in Appendix A.3 it is shown that this corresponds to failure of the mesoelement.

4.3.3 Constitutive Equations

Collecting the equations of the last two subsections gives the set of constitutive equations which have to be solved in numerical analysis on a microscale:

$$\begin{aligned}
 \varepsilon_{ij}^\mu &= \varepsilon_{ij}^{e\mu} + \varepsilon_{ij}^{p\mu}, \\
 \varepsilon_{ij}^{e\mu} &= \frac{1 + \nu}{E} \frac{\sigma_{ij}^\mu}{1 \Leftrightarrow D} \Leftrightarrow \frac{\nu}{E} \frac{\sigma_{kk}^\mu}{1 \Leftrightarrow D} \delta_{ij}, \\
 \varepsilon_{ij}^{p\mu} &= \begin{cases} \frac{3}{2} \frac{\bar{\sigma}_{ij}^{\mu D}}{\sigma_f} \dot{p}^\mu & \text{if: } f = 0 \wedge \dot{f} = 0, \\ 0 & \text{else,} \end{cases} \\
 \dot{D}^\mu &= \begin{cases} \frac{\sigma_f^2}{2ES} R_V^\mu \dot{p}^\mu & \text{if: } p^\mu \geq p_D^\mu \wedge f = 0 \wedge \dot{f} = 0, \\ 0 & \text{else.} \end{cases}
 \end{aligned} \tag{4.77}$$

4.3.4 Numerical Procedure

In [57] *Lemaitre & Doghri* have developed a fully implicit integration scheme with explicitly updated unknowns. This scheme is described below. The input are the strains computed first in an elastic FE structure analysis. They use this scheme and a special jump-in procedure in a postprocessor. Here it is also used for optimization but with a recoupling to the whole structure.

Integration Scheme

All variables are known for the time-step ${}^k t$. The task is to find the update for the time-step ${}^{k+1} t$:

$${}^{k+1} t = {}^k t + \Delta^k t. \tag{4.78}$$

The superscript $k + 1$ is omitted. All variables without subscript belong to $k + 1$. All variables except the fatigue limit σ_f belong to microscale, the superscript μ is also omitted in this section, because the scheme can be used more generally, not only for fatigue [56]. A tensorial notation is used.

We start with an elastic predictor step:

$$\tilde{\sigma}_{ij} = \frac{E}{1 + \nu} \left[\frac{\nu}{1 \Leftrightarrow 2\nu} \varepsilon_{ll} \delta_{ij} + \varepsilon_{ij} \Leftrightarrow \varepsilon_{ij}^{k,p} \right]. \quad (4.79)$$

All other ‘‘plastic’’ variables are equal to their values at ${}^k t$. If the elastic predictor satisfies the yield condition $f \leq 0$, the elastic predictor step was correct and the computation is going on with the next time increment. If the yield condition is violated $f > 0$, a plastic correction step is necessary. Therefore the rate equations (Eq. 4.77) are discretized in an incremental form. This leads to a fully implicit integration scheme with unconditional stability [70] and explicit expressions for the plastic corrections. The solution for the time-step ${}^{k+1} t$ has to fulfill the following relations:

$$\begin{aligned} f &= \tilde{\sigma}_{eq} \Leftrightarrow \sigma_f = 0, \\ \tilde{\sigma}_{ij} &= \frac{E}{1 + \nu} \left[\frac{\nu}{1 \Leftrightarrow 2\nu} \varepsilon_{ll} \delta_{ij} + \varepsilon_{ij} \Leftrightarrow \varepsilon_{ij}^{k,p} \Leftrightarrow \Delta \varepsilon_{ij}^p \right], \\ \Delta \varepsilon_{ij}^p &= N_{ij} \Delta p \quad \text{with} \quad N_{ij} = \frac{3}{2} \frac{\tilde{\sigma}_{ij}^D}{\tilde{\sigma}_{eq}} \quad \text{and} \\ \Delta D &= \frac{Y}{S} \Delta p \end{aligned} \quad (4.80)$$

with

$$\Delta X = X_{n+1} \Leftrightarrow X_n.$$

If $\Delta \varepsilon^p$ in the second equation of 4.80 is replaced using the third equation the problem is reduced to the two nonlinear primary equations with the two unknowns $\tilde{\sigma}$ and p :

$$f = \tilde{\sigma}_{eq} \Leftrightarrow \sigma_f = 0 \quad (4.81)$$

and

$$h_{ij} = \tilde{\sigma}_{ij} \Leftrightarrow \frac{E}{1 + \nu} \left[\frac{\nu}{1 \Leftrightarrow 2\nu} \varepsilon_{ll} \delta_{ij} + \varepsilon_{ij} \Leftrightarrow \varepsilon_{ij}^{k,p} \Leftrightarrow N_{ij} \Delta p \right] = 0. \quad (4.82)$$

This nonlinear equation system is solved iteratively by Newton’s method. For each iteration s there are the following equations:

$$f + \frac{\partial f}{\partial \tilde{\sigma}_{ij}} C_{ij}^{\tilde{\sigma}} = 0 \quad \text{and} \quad h_{ij} + \frac{\partial h_{ij}}{\partial \tilde{\sigma}_{pq}} C_{pq}^{\tilde{\sigma}} + \frac{\partial h_{ij}}{\partial p} C^p = 0 \quad (4.83)$$

f , \mathbf{h} and their partial derivatives are taken at the time step ${}^{k+1} t$ and at the iteration s . The corrections of the effective stress and the accumulated plastic strain are defined by:

$$C_{ij}^{\tilde{\sigma}} = {}^{s+1} \tilde{\sigma}_{ij} \Leftrightarrow {}^s \tilde{\sigma}_{ij} \quad \text{and} \quad C^p = {}^{s+1} p \Leftrightarrow {}^s p. \quad (4.84)$$

The starting iteration ($s = 0$) corresponds to the elastic predictor. After some analysis [55] the following explicit expressions are derived for the corrections:

$$C^p = \frac{2(1 + \nu)(f \Leftrightarrow N_{ij} h_{ij})}{3E} \quad \text{and} \quad (4.85)$$

$$C_{ij}^{\tilde{\sigma}} = \Leftrightarrow \frac{2}{3} (f \Leftrightarrow N_{qp} h_{qp}) N_{ij} \Leftrightarrow \frac{h_{ij} + \frac{E \Delta p}{\sigma_{eq}(1+\nu)} N_{qp} h_{qp} N_{ij}}{1 + \frac{3}{2} \frac{E}{\sigma_{eq}(1+\nu)} \Delta p}. \quad (4.86)$$

The procedure is working adaptive: if a solution is not found, the time increment is bisected.

Once p and $\tilde{\sigma}$ are found, ϵ^p and D are calculated from their discretized constitutive equations. The stress components are given by $\sigma_{ij} = (1 \Leftrightarrow D) \tilde{\sigma}_{ij}$.

Jump-In Cycles Procedure

In fatigue, particular in HCF, there is a large number of periodic cycles, so computation step by step becomes impossible because of CPU-time. Therefore in [55, 56] a jump-in procedure is described. It is working in two steps:

a.) Before damage growth: ($p^\mu \leq p_D^\mu$)

A calculation is performed until a stabilized cycle N_s is reached. δp^μ is the increment in plastic strain for this cycle. It is assumed, that the increment in plastic strain is linear over the next ΔN cycles. With ΔN determined in the following way:

$$\Delta N = \frac{\Delta p^\mu}{\delta p^\mu}, \quad (4.87)$$

with

Δp^μ : a given value which determines the accuracy.

A jump of ΔN in cycles is done and the accumulated plastic strain is updated:

$$p^\mu(N_s + \Delta N) = p^\mu(N_s) + \Delta N \delta p^\mu. \quad (4.88)$$

This procedure is repeated until damage growth starts.

b.) With damage growth ($p^\mu \geq p_D^\mu$):

The calculation is performed with a constant damage ($\dot{D}^\mu = 0$) until a stabilized cycle is reached. A fully coupled elasto-plastic and damage calculation is performed for the considered microelement for the next cycle. δp^μ and δD^μ are the increments of accumulated plastic strain and damage for this stabilized cycle. It is assumed, that during the next ΔN cycles there is a linear accumulation in damage and accumulated plastic strain. ΔN is now determined by a value for Δp^μ as well as a value for ΔD^μ :

$$\Delta N = \min \left\{ \frac{\Delta p^\mu}{\delta p^\mu}, \frac{\Delta D^\mu}{\delta D^\mu} \right\}. \quad (4.89)$$

A jump of cycles is performed and damage and accumulated plastic strain are updated:

$$p^\mu(N_s+1+\Delta N) = p^\mu(N_s+1) + \Delta N \delta p^\mu \quad \text{and} \quad D^\mu(N_s+1+\Delta N) = D^\mu(N_s+1) + \Delta N \delta D^\mu. \quad (4.90)$$

The procedure is repeated until the chosen number of cycles is reached or the part is broken.

A guess for Δp and ΔD performing accurate results is given in [55]:

$$\Delta D^\mu = \frac{D_{1c}}{50} \quad \text{and} \quad \Delta p^\mu = \frac{S}{Y^\mu} \Delta D^\mu. \quad (4.91)$$

Coupling

In [56] *Lemaitre* distinguishes three kinds of coupling between the damage and the stress-strain field of the structure:

- **Uncoupled Analysis**

In a first step the stress and the strain field are computed. Then the point(s) with highest damage equivalent stress (σ^*) are determined.

As long as the loading is proportional (Definition in A.1), these point(s) will have the highest damage equivalent stress during the whole loading history. For a non-proportional loading the highest loaded point is not necessarily connected with the highest damage. A point less loaded but for a longer time above the threshold can become more damaged and therefore more dangerous than the highest loaded point. At last the kinetic damage law on a micro- or mesolevel (Eq. 4.77) is integrated for all these critical points. There is no coupling of damage to the stress-strain field. For strain controlled conditions, it can be shown [56] that the uncoupled analysis gives a lower bound on lifetime.

- **Fully Coupled Analysis**

For ductile and creep damage, often a large part of the structure is damaged. Then, for a good accuracy, at least for a substructure, the coupling between the damage and the strain field must be considered. This makes the calculation more complex, but it is the only way to proceed. There are the same problems with convergence of iterations and with CPU-time as for classical elastoplastic analysis.

A fully coupled elasto-plastic damage integration algorithm is described in [9].

- **Locally Coupled Analysis**

Quite often damage is highly localized. This means, the damaged volume is small

in comparison to the whole structure and even to the RVE. Therefore an uncoupled analysis on a macroscale which considers only a local coupling is performed.

The method of locally coupled analysis is particularly recommended [56] for brittle and fatigue damage. There is only a coupling on microscale. This means, after the primary structure analysis, there is no longer any boundary value problem. The stress-strain field will stay constant during lifetime on a mesoscale and only on microscale a reduction of Cauchy stress is observed.

It can be shown, that if the point of critical damage is reached also the mesoelement will break down (see Section A.3).

If a locally coupled analysis is carried out to model fatigue behavior for the considered problems and there is a proportional loading, the minimization of maximum damage will always give the same results as the static optimization. This can be understood by the following considerations:

With some minor simplifications we have derived Eq 4.68. In this equation the damage increment is only dependent on the hydrostatic stress and the (elastic on the mesoscale) strain increment. For the here considered 2-D case the following expression results for a coordinate system orientated in the directions of principal stresses ($\hat{\sigma}_1, \hat{\sigma}_2$:

$$\dot{D}^\mu = \frac{\sigma_f^2}{ES} \left[\frac{2}{3}(1 + \nu) + 3(1 \Leftrightarrow 2\nu) \left(\frac{\sigma_2}{\sigma_f} \right)^2 \right] \frac{(1 + \nu^2)^{\frac{1}{2}}}{E} |\dot{\sigma}_2| \quad (4.92)$$

Minimization of the von Mises equivalent stress in the case of static optimization means minimization of the tangential stress σ_t . In 2D on a mesoscale $\sigma_t = \sigma_2$. Therefore, static minimization means also minimization of the second principal stress and thus minimization of the damage increment!

The locally coupled analysis is summarized in Fig. 4.6.a. For this work the procedure was modified because of two reasons:

At first it is typical for an optimized part, that a large part of the structure is equally loaded (See Fig. B.4.a and compare with B.4.c). Therefore, not only one element will be damaged, but at least almost the whole region along the free boundary.

Second, a stress redistribution is observed during lifetime with the mentioned photoelastic experiments (See Fig. B.4.b and B.4.d).

The locally coupled analysis supposes that there is no coupling of the damage of the microelement to the mesoelement except that failure of the microelement will cause the breakdown of the mesoelement. In this case the stress redistribution will be observed only on microscale. The stress redistribution found implies a damage at mesoscale before the fail down of the part. Here we have load driven experiments. If a region is damaged, it will not carry as much load as before. A consequence is that the region around the damaged elements has to carry more load now. Certainly it will give the best results to do a fully coupled analysis. But this is very time intensive, so an alternative was searched. The locally coupled analysis was taken and extended in the following way (See Fig. 4.6.b):

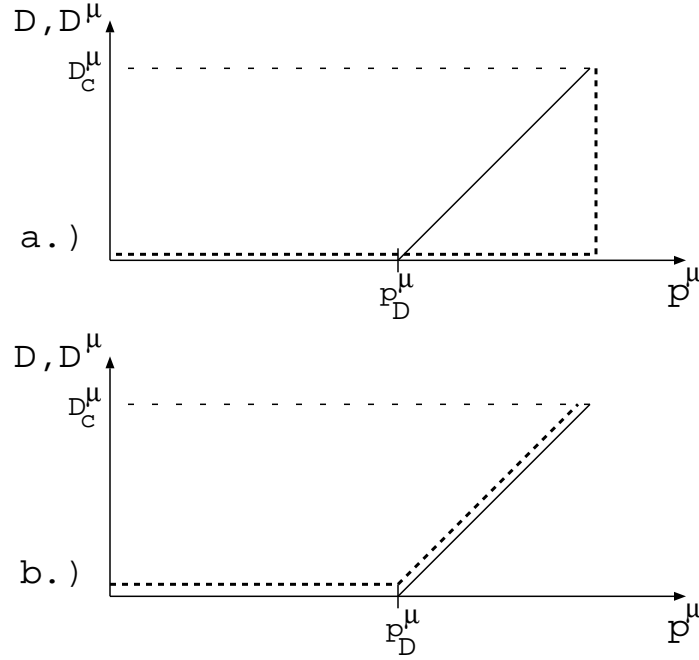


Figure 4.5: Solid line: damage at microlevel, dashed line: damage at mesolevel. a.) Locally coupled: coupling between micro- and mesoscale only in the point of critical damage; b.) Modified locally coupled: direct transfer of the microscopically determined damage to the mesoscale.

• Modified Locally Coupled Analysis

At first a structure analysis is made and the element with highest damage equivalent stress is determined. This element will control the jump-in cycles procedure. Then a damage analysis is carried out at first for this element and a first jump of cycles is fulfilled. The damage analysis is then carried out for all other elements in a substructure with an appropriate jump of cycles. After this first jump is done with all elements the accumulated plastic strains and the damage variables are updated. In a first approximation due to the fact that the fail down of the inclusion causes the fail down of the whole mesoelement the microscopic determined value of the damage variable (Eq. 4.77) is transferred directly to the mesoscale:

$$D = D^\mu \quad \text{update every jump-in cycles.} \quad (4.93)$$

If damage has taken place at least in one element a new structure analysis is carried out after every jump-in cycles for the whole structure with modified Young's modulus where necessary. The modification of the Young's modulus corresponds to the usage of the strain equivalence principle. Therefore we have to adopt the modified Hooke's law (in difference to the work of *Lemaitre*):

$$\varepsilon_{ij}^e = \frac{\sigma_{ij}(1 + \nu)}{(1 \Leftrightarrow D)E} \Leftrightarrow \frac{\nu \sigma_{kk}}{(1 \Leftrightarrow D)E} \delta_{ij} \quad \text{with} \quad D = D^\mu. \quad (4.94)$$

This procedure is repeated until the desired number of cycles is reached or the part has broken [36].

For optimization a third iteration slope is put around all. This means very time intensive calculation. This is one of the numerical problems discussed in the next chapter.

4.4 Further Developments

4.4.1 Anisotropic Damage

The assumption that damage is isotropic is realistic in many cases, especially under proportional loading when the directions of principal stresses remain constant.

As was shown in Section 2.1 almost all fatigue microcracks (state I) appear under 45° because they are shear stress controlled. Therefore, the assumption of isotropic damage is not really fulfilled but only a first simple approximation.

The most simple way to model anisotropic damage is to assume that damage will only occur in the plane perpendicular to the highest principal stress (*Lecki, Hayhurst, 1973*).

$$[\tilde{\sigma}] = \begin{bmatrix} \sigma_1 & 0 & 0 \\ 0 & \sigma_2 & 0 \\ 0 & 0 & \frac{\sigma_3}{1-D} \end{bmatrix}, \quad (4.95)$$

$$\sigma_1 < \sigma_2 < \sigma_3.$$

Murakami has developed an approach based on geometrical considerations with a second order damage tensor.

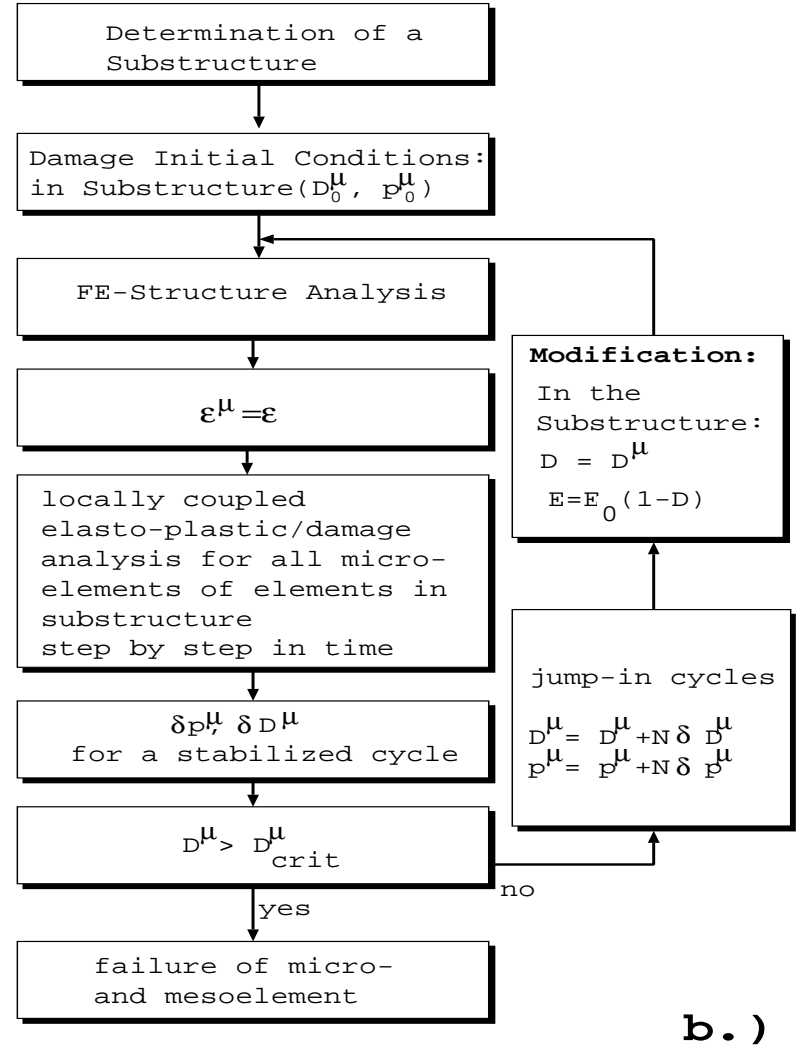
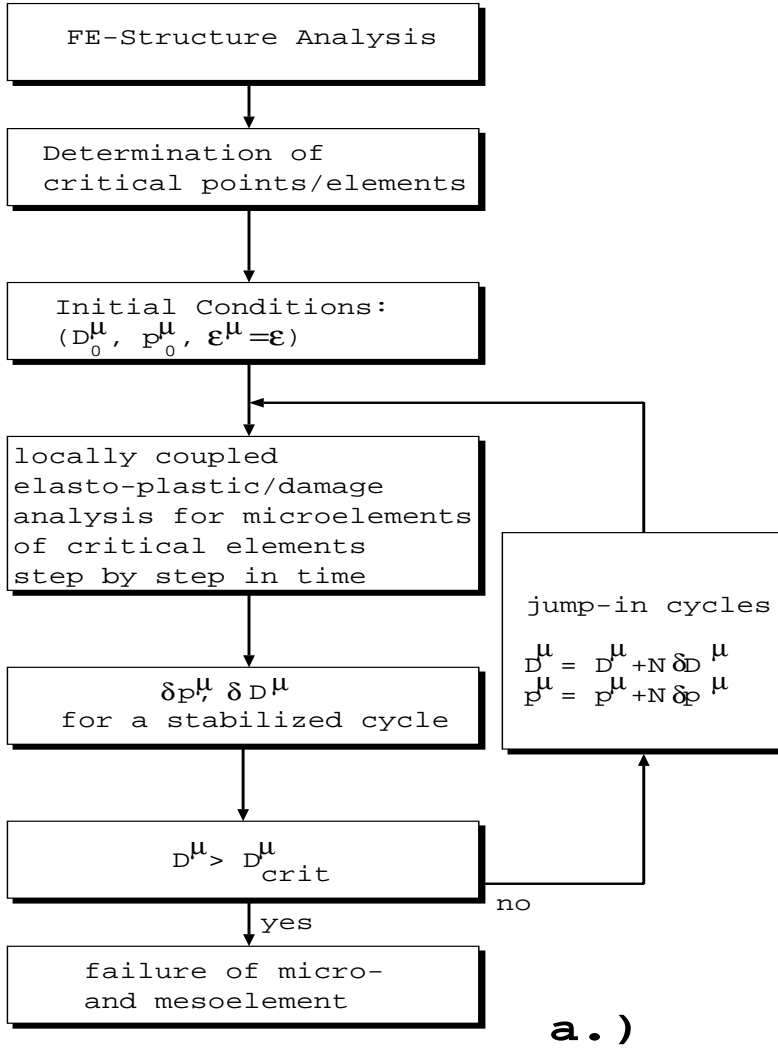
In his model, not only the effective cross section is decreasing during loading, but also the orientation of that cross section. Assuming that the shape of the considered cross section is not changing (this leads to the case of orthotropic damage) we can write according to the isotropic case:

$$(\mathbf{1} \Leftrightarrow \mathbf{D})\vec{n}\delta S = \vec{n}\delta\tilde{S}, \quad (4.96)$$

with

$\mathbf{1}$: second order identity tensor, \mathbf{D} : second order damage tensor.

Figure 4.6: Damage analysis a.) locally coupled b.) modified locally coupled



When the principal directions of stress and damage coincide, the following expression is valid:

$$[\tilde{\sigma}] = \begin{bmatrix} \frac{\sigma_1}{1-D_1} & 0 & 0 \\ 0 & \frac{\sigma_2}{1-D_2} & 0 \\ 0 & 0 & \frac{\sigma_3}{1-D_3} \end{bmatrix}. \quad (4.97)$$

Chaboche and *Lemaitre* have introduced a fourth order damage tensor on the basis of the concept of effective stress connected with the strain equivalence principle.

To describe these concepts in detail is out of the scope of this work, more informations are found in [56, 57].

4.4.2 Deterministic/Probabilistic Theory

As far as described, damage mechanics is a deterministic theory. As we have seen in Section 2.2.5 scattering in lifetime results and a size effect are inherent features of fatigue behavior. These effects are well described by the statistical K_f -hypotheses (see Chapter 1, weakest-link model) but cannot be determined with the introduced damage mechanics model.

There is the possibility to include these features into the CDM concept. Instead of to give every element a certain initial value of accumulated strain p_0 and initial damage D_0 these values can be assumed statistically distributed. The introduction of such statistical features is actual research work in CDM.

Chapter 5

Numerical Tools and Results

In contrast to the work of *Fanni* [31], who describes the whole dynamic fatigue behavior using the fatigue notch factor with only a single static structure analysis, here for one damage analysis several structure analyses are carried out.

Besides this, damage growth is very stress sensitive.

Therefore, not only a fast but also a very accurate structure analysis is required. At the beginning of this chapter, a very simple but effective error indicator is described. It is used to build up adequate FE-meshes.

In order to save CPU-time, a successive strategy is used during optimization, and B-splines instead of node-coordinates describe the free boundary, and a substructure is introduced. Using these tools introduced in the first part of this chapter, a static optimization is carried out first to show that the procedure works. After some damage analysis showing the difference between local and modified coupling, optimization is carried out with respect to damage at the end of this chapter.

5.1 Simple Error Indicator

On the basis of the heuristic error estimator published by *Zienkiewicz* and *Zhu* [100] a simple error indicator is introduced, and according to the results, a local and/or global h refinement is realized.

The *Zienkiewicz & Zhu* error estimator is recommended in [2], particularly for linear displacement elements. In [74] it is shown that for linear displacement elements this heuristic error estimator is equivalent to the residual error estimator formulated by *Babuska* and *Rheinboldt* [6].

If \mathbf{u} denotes the correct solution of the boundary value problem (Eq. 3.5) and the resulting correct stress field is $\boldsymbol{\sigma}$, the errors are defined by:

$$\begin{aligned} \mathbf{e} &= \mathbf{u} \Leftrightarrow \hat{\mathbf{u}} && \text{the error in displacement and} \\ \mathbf{e}_\sigma &= \boldsymbol{\sigma} \Leftrightarrow \hat{\boldsymbol{\sigma}} && \text{the error in stress.} \end{aligned} \quad (5.1)$$

The approximated solution is marked by the hat.

This is a pointwise definition of the errors. It is more convenient to adopt an integral measure, e.g. the energy norm:

$$\|\mathbf{e}\| = \left(\int_{\Omega} \mathbf{e}^T \mathbf{B}^T \mathbf{D} \mathbf{B} \mathbf{e} d\Omega \right)^{\frac{1}{2}} = \left(\int_{\Omega} \mathbf{e}_\sigma^T \mathbf{D}^{-1} \mathbf{B} \mathbf{e}_\sigma d\Omega \right)^{\frac{1}{2}} \quad (5.2)$$

If the L_2 norm is adopted, the error in stress is:

$$\|\mathbf{e}_\sigma\|_{L_2} = \left(\int_{\Omega} \mathbf{e}_\sigma^T \mathbf{e}_\sigma d\Omega \right)^{\frac{1}{2}} \quad (5.3)$$

A relative error is defined by the following expression:

$$\eta = \frac{\|\mathbf{e}\|}{\|\mathbf{u}\|} \cdot 100\%. \quad (5.4)$$

A seldom used - but very relevant - measure is the *stress error in absolute terms* [100]. By the use of the L_2 norm it can be defined for a subdomain $\tilde{\Omega}$:

$$\Delta\sigma = \left(\frac{\|\mathbf{e}_\sigma\|_{L_2}^2}{\tilde{\Omega}} \right)^{\frac{1}{2}} \quad (5.5)$$

Here, we define as error indicator a relative error on the basis of the last equation:

$$e_\sigma^r = \frac{\Delta\sigma}{\max_{i=1..nel} \sigma_{eq}} \quad (5.6)$$

This measure will be used for an adaptive mesh refinement.

For the application of the derived indicator we have to determine the correct solution ($\boldsymbol{\sigma}$): The introduced displacement method works with linear shape functions. This means, the strains and also the stresses ($\hat{\boldsymbol{\sigma}}$) stay constant within the elements and show a discontinuity at the element boundaries (see Fig. 5.1). Obviously an improved approximation for the correct stress is achieved [100] by interpolating the averaged nodal stresses maintaining the equilibrium with the shape functions.

$$\boldsymbol{\sigma}^* = \mathbf{N} \bar{\boldsymbol{\sigma}} \quad \text{with} \quad \int_{\Omega} \mathbf{N}^T (\boldsymbol{\sigma}^* \Leftrightarrow \hat{\boldsymbol{\sigma}}). \quad (5.7)$$

Therefore, $\boldsymbol{\sigma}^*$ is used as a guess for the correct solution. With this approximation the stress error is determined as follows:

$$\mathbf{e}_\sigma \approx \boldsymbol{\sigma}^* \Leftrightarrow \hat{\boldsymbol{\sigma}} \quad (5.8)$$

With this strategy a relative stress error is calculated for every element.

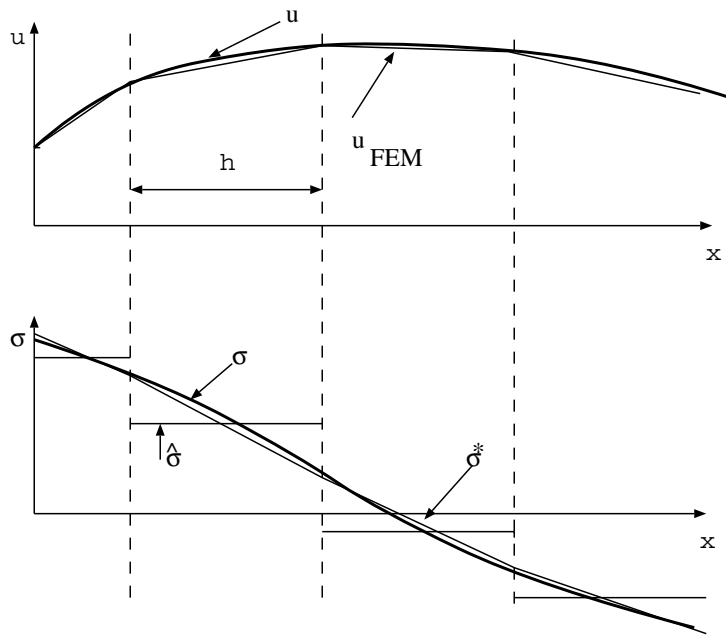


Figure 5.1: Approximation of error in stress for a one-dimensional problem with linear displacement elements.

5.2 Substructuring and Mesh Refinement

A substructure (Ω_S) is introduced around the free boundary to save CPU-time. In the second part of the paragraph, several techniques of mesh refinement are introduced to reduce the error in the calculation of the stress-strain field.

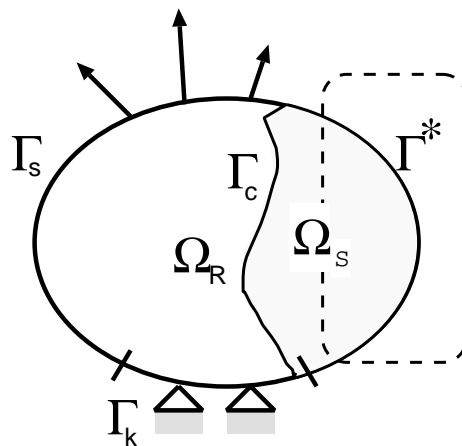


Figure 5.2: Definition of a substructure: $\Omega = \Omega_R \cup \Omega_S \wedge \Omega_R \cap \Omega_S = \emptyset$.

5.2.1 Substructuring

During the optimization of the considered problem, almost the whole structure remains unchanged. By introducing a substructure (Ω_S), almost the whole stiffness matrix will not change during the optimization procedure and only the part belonging to the substructure must be updated. A second reason for the introduction of a substructure is the damage calculation. Damage accumulation is very stress sensitive. This means, only points with high stress concentration will become damaged. Therefore, it is not necessary to carry out a damage calculation for the whole structure. It is sufficient to do so in the substructure or even in some *layers* of the substructure.

During optimization, due to the movement of the free boundary, often the FE-mesh is destroyed. It is adequate to rebuild the mesh only in Ω_S in this case.

Two kinds of substructuring were tested:

Automatic Net Generation

The used automatic front contour mesh generator [17, 47] allows to specify three kinds of boundaries:

- straight lines,
- circular curves and
- nodewise defined boundaries.

The common boundary (Γ_c , see Fig. 5.2) - i.e.the boundary between the substructure and the rest of the structure - is always determined nodewise. During the optimization procedure the free boundary is also determined nodewise.

The automatic mesh generation is controlled by the choice of the element size at every corner. If a boundary is given nodewise, there is no possibility to influence the mesh generation in this place. Therefore it has been observed that during the optimization process often poor meshes are built (large and small triangles beside each other) with this automatic mesh generation. The automatic mesh generator was finally used only for the remaining structure (Ω_R) with some local mesh refinement if necessary.

Adaptive Substructuring

For the special notch problem considered here (see Section 5.4), an adaptive substructure technique was also generated. With this substructure technique it is possible to refine the mesh of the substructure layer by layer and to introduce more layers if necessary (See Fig. 5.3). During optimization the free boundary will move. The nodes in the substructure

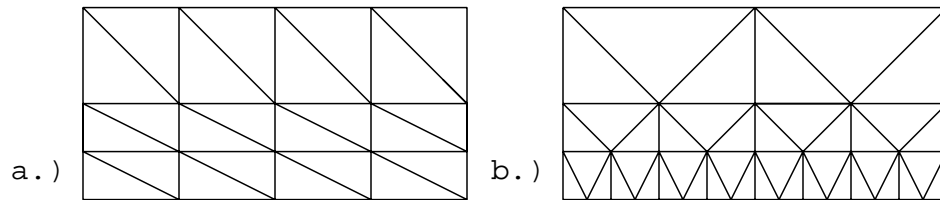


Figure 5.3: Substructure with three layers a.) without b.) with refinement from layer to layer. It is also possible to refine the mesh by introducing new layers.

will move according to this movement as described in [31].

This adaptive substructuring was used for optimization. With this procedure it was always possible to get results in the structure analysis with an error $e_{\sigma}^r < 5\%$. Two examples for the used substructured meshes are shown in Fig. 5.11.

5.2.2 Mesh Refinement

A threshold for the stress error is determined and four levels (see Fig. 5.4) are used for local mesh refinement. Besides this local mesh refinement, a global mesh refinement

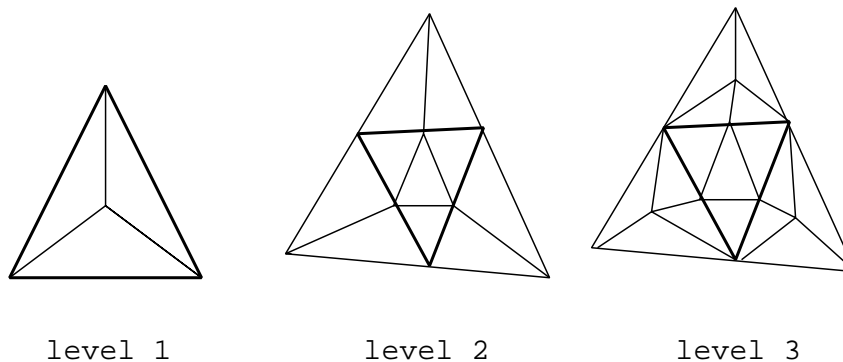


Figure 5.4: Three levels of compatible local mesh refinement

(quartering every triangle) was done if necessary. If the substructure technique was used, this local mesh refinement was only adopted in the remaining structure.

5.3 Successive Strategies

These strategies are particularly valuable in case node coordinates are used as design variables. Two successive strategies were tested: First, the mesh was refined during optimization. At the beginning just a rough approximation was used. This enables the nodes on the free boundary to make great movements without deterioration of the mesh. If a remarkable reduction of the cost function cannot be achieved any more, the whole mesh, or at least the mesh in the substructure, was refined for further improvement. Second, not all nodes on the free boundary are used as design variables the whole time. At the beginning only a small number (e.g. every third) was taken and the nodes between the design nodes were interpolated during the optimization process [31]. The amount of CPU-time saved using the second strategy was small. It was tested, but not used for the displayed optimization results [44].

5.4 Numerical Example

As a numerical example the notched tension bar was chosen. In Fig. 5.5 the problem is demonstrated. It is sufficient to discretize a fourth of the part because of the inherent symmetry. The adequate support and the variation domain can also be found in Fig. 5.5. During optimization the measurement of the damage constants was not finished for 30CrNiMo8. Therefore, the material data chosen for optimization are::

- **Linear Elasticity**
Young's modulus $E = 200000MPa$; Poisson's ratio $\nu = 0.3$;

- **Plasticity**
fatigue limit $\sigma_f = 180MPa$; yield stress $\sigma_y = 260MPa$;
ultimate stress $\sigma_u = 700MPa$;

- **Damage**
damage constant $S = 7MPa$; damage threshold $\varepsilon_{pD} = 10\%$;

The material data are found in [56] for stainless steel ($T = 20^0C$).

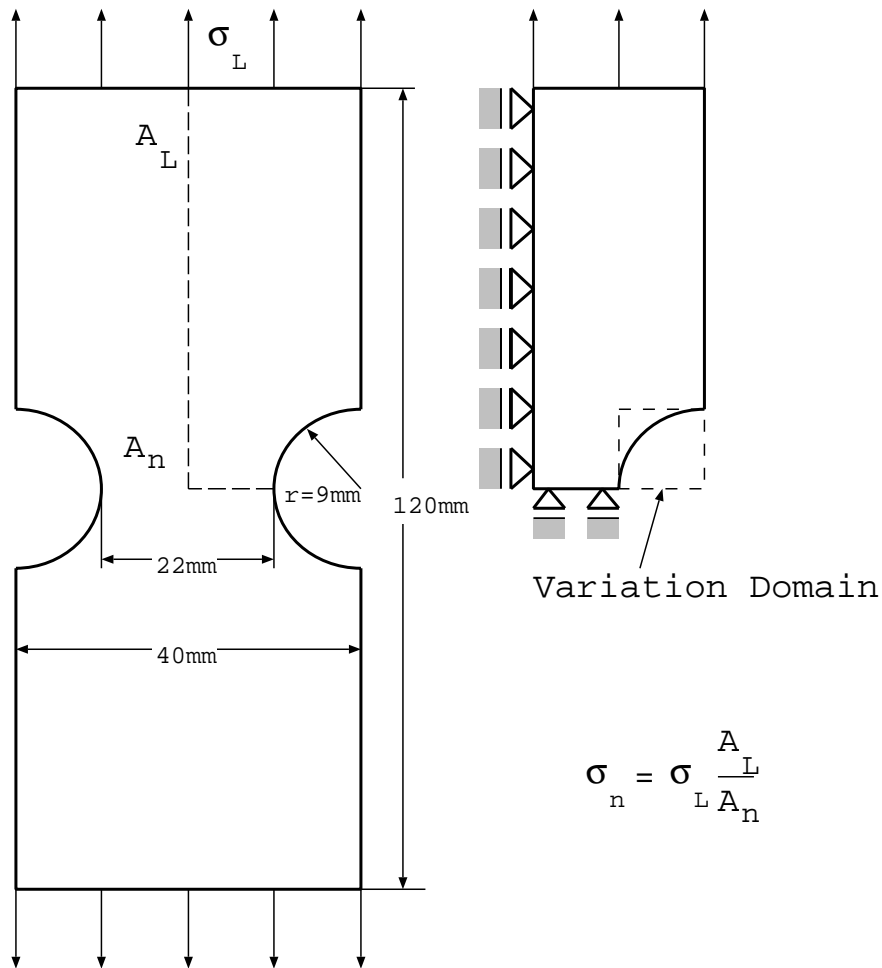


Figure 5.5: The notched tension bar.

5.5 Statically Optimized Shape

As a starting point the optimization procedure was tested for static optimization. This means minimization of maximum von Mises stress at the free boundary.

The circular notch was chosen as a start shape if node coordinates were used.

If the free boundary was described by B-splines, a straight line was chosen between the fixed points, because of the linear precision property of the B-spline (see Section 3.3.2).

The static optimization was carried out without substructuring.

5.5.1 Numerical Results

For the first and second displayed result, node coordinates were used as design variables. A successive strategy was applied, at last 31 nodes were used. Besides the constraints

in variation domain, the distance constraint and the concave constraint were used in the first example (Fig. 5.6). The start geometry was the circular notch.

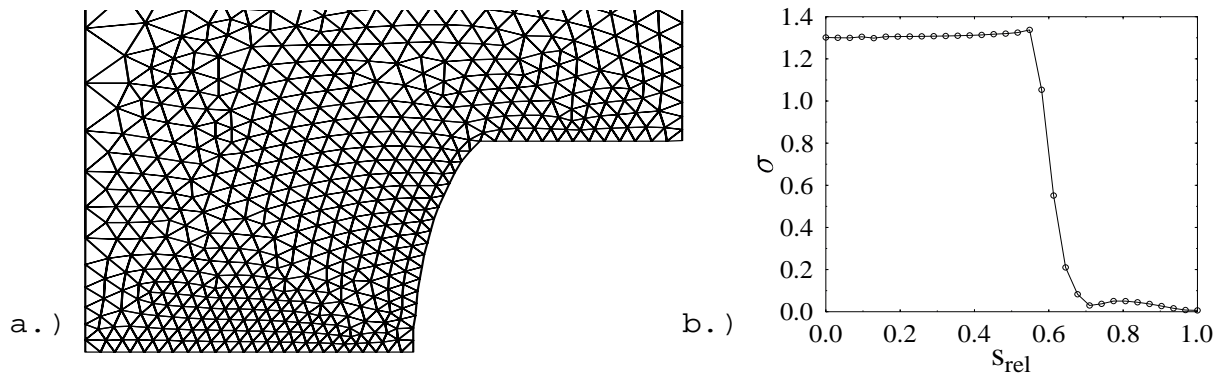


Figure 5.6: Static optimum shape: a.) mesh at the end of optimization b.) normalized von Mises equivalent stress ($\sigma = \frac{\sigma_{eq}}{\sigma_n}$) along the optimized boundary.

The next example (Fig. 5.7) was optimized with just the same features. In addition the curvature constraint was mentioned ($r_{min} = 3mm$). The third (Fig. 5.8) and fourth

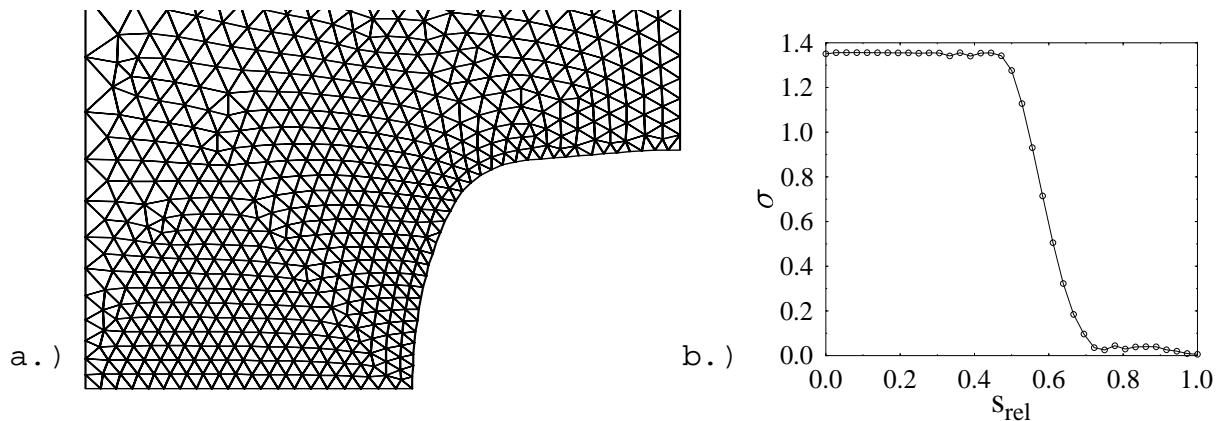


Figure 5.7: Static optimum shape with curvature constraint: a.) mesh at the end of optimization b.) normalized von Mises equivalent stress along the optimized boundary.

example (Fig. 5.9) use B-splines to approximate the free boundary. In the fourth example the curvature is additionally used. In both cases the distance constraint was certainly shut off.

5.5.2 Discussion

There is a close agreement of the optimization results with the results of *Fanni* [30, 31]. If the curvature constraint is used, the stress is somewhat higher and the distance of

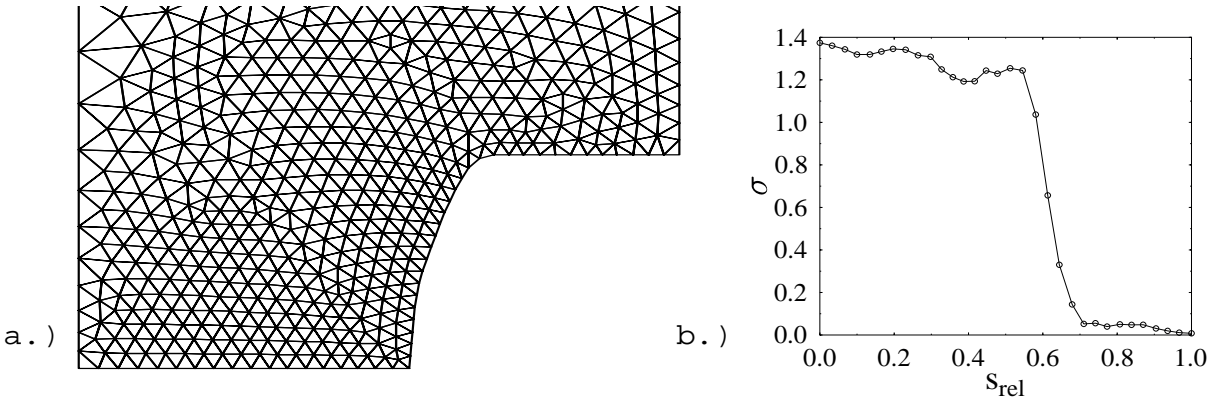


Figure 5.8: Static optimum shape (de Boor-ordinates as design variables): a.) mesh at the end of optimization b.) normalized von Mises equivalent stress along the optimized boundary.

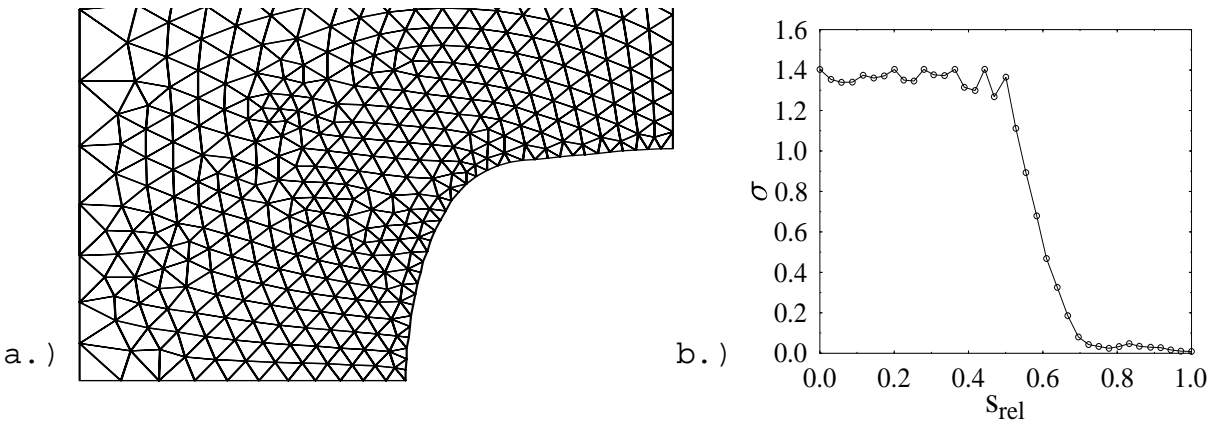


Figure 5.9: Static optimum shape with curvature constraint (de Boor-ordinates as design variables): a.) mesh at the end of optimization b.) normalized von Mises equivalent stress along the optimized boundary.

constant stress is a little bit shortened down (compare, for instance, Fig. 5.6.b and Fig. 5.7.b). The stress concentration factor ($K_t = \frac{\sigma_{max}}{\sigma_n}$) increases from $K_t = 1.31$ to $K_t = 1.35$ in case that node coordinates are used as design variables and from $K_t = 1.37$ to $K_t = 1.4$, if the de Boor-ordinates are used.

If B-splines are used to describe the free boundary the stress is no longer constant but shows little oscillations. This is due to the interpolation of the node coordinates. Similar results have been derived if, instead of all node coordinates, only some are used as design variables and the position of the others is interpolated after every optimization step. Nevertheless, the B-spline approximation (maximum ten design variables) will be used in the case of time intensive (!) damage optimization. With a maximum increase of less than 3% in stress, the achieved accuracy is within the tolerated stress error and therefore sufficient.

5.6 Damage Analysis

Before the described damage concept was used for optimization, some damage analyses were carried out. At first, the algorithm is tested in this section. After this, a comparison is made between the damage accumulation in a part with circularly notched shape and a statically optimized notched part.

5.6.1 Testing the Algorithm

Damage accumulation as described in Chapter 4 is very stress sensitive. This means a small error in the stress-strain field calculation will produce any result in damage calculation. Therefore it is very important to have a very accurate FE-simulation which means a very fine mesh because of the chosen linear displacement setup. For all meshes used in damage analysis only an error less than 5% was tolerated. At first the mesh dependency of the lifetime was studied.

Mesh Dependency with Respect to Global Mesh Refinement

The mesh dependency of lifetime with respect to global mesh refinement was examined for the circular notch with a load of $\sigma_L = 80 MPa$. The fundamental mesh (777 elements, $e_\sigma^r = 5.16\%$) and the second globally refined mesh (3108 elements, $e_\sigma^r = 3.77\%$) are shown in Fig. 5.10.

A third mesh was obtained by a second global refinement (12432 elements).

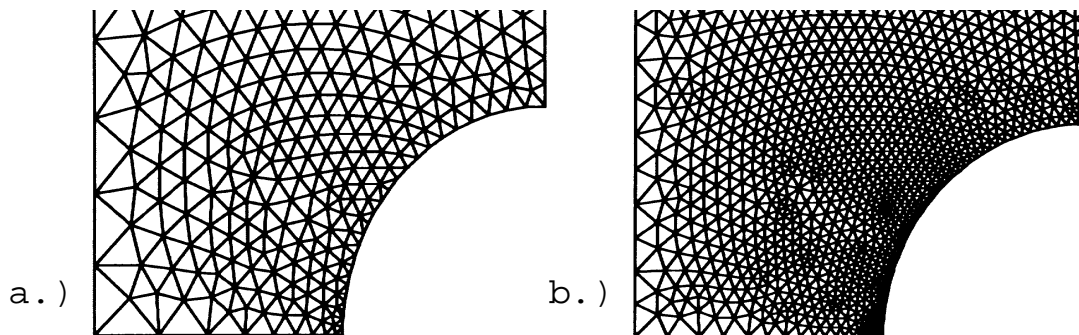


Figure 5.10: a.) Fundamental net (777 elements) and b.) first global refinement (3108 elements)

N_0 is connected with the number of cycles until the first element is damaged ($D_i > 0$).

N_R determines the number of cycles until the first element reaches the critical damage value ($D_C = 1$). The results for the three meshes are summarized in the table below:

	mesh 1	mesh 2	mesh 3
N_0	1358	1390	1402
N_R	34715	35144	33946

The greatest difference is 3.4%. This is within the desired accuracy and certainly tolerable.

Mesh Dependency with Respect to Local Mesh Refinement

In a second test the two first meshes of the previous subsection were chosen and the most damaged element was divided into three parts (=local net refinement level 1). Now, the damage in these three new elements is compared at the end of the lifetime of the part:

	D_1	D_2	D_3
mesh 1	0.989	0.765	0.764
mesh 2	0.985	0.896	0.896

The maximum difference is 9% for the “good” (second) mesh. This effect is of an order which cannot be neglected. The mesh dependency of damage calculations is well known. It is a present research topic to overcome this problem with nonlocal approaches introducing a kind of structural length. It was out of the scope of this work to go into detail here, but it was found [93] that the effect of mesh dependency is smaller if the desired value of accumulated damage is set down. In fatigue for most material the structure will fail at a damage value $D_C < 1$. For the considered material $D_C = 0.2$ was found [56]. This improves the result significantly.

Mesh Dependency and Coupling

The second mesh was also analyzed with the same loading but just locally coupled. The result was the expected same number of cycles in damage initiation ($N_0 = 1396$) and the

increased number in cycles until rupture ($N_R = 42058$).

Besides this, once more the most damaged element of the two meshes of Fig. 5.10 were divided into three parts. It is remarkable that in the case of a locally coupled analysis (D in the table has the meaning of D^μ in this case) the mesh dependency becomes worse:

	D_1	D_2	D_3
mesh 1	0.989	0.534	0.534
mesh 2	0.985	0.616	0.616

5.6.2 Comparison of Circularly Notched and Statically Optimized Part

In Fig. 5.11 the meshes of the circularly notched part and the statically optimized part including a substructure are shown. The mesh of the statically optimized part was also used as start geometry for the damage optimization described in the next section. It was necessary to double the nodes on the free boundary (65 nodes) to achieve a stress error $e_\sigma^r < 5\%$ in this case.

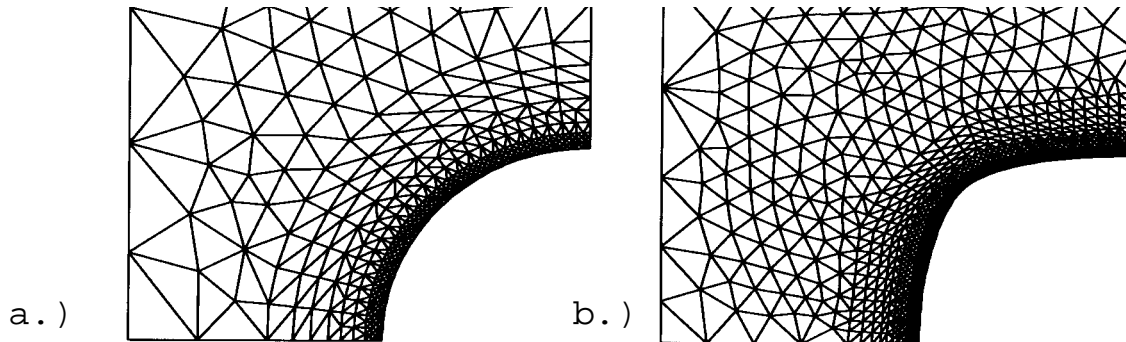
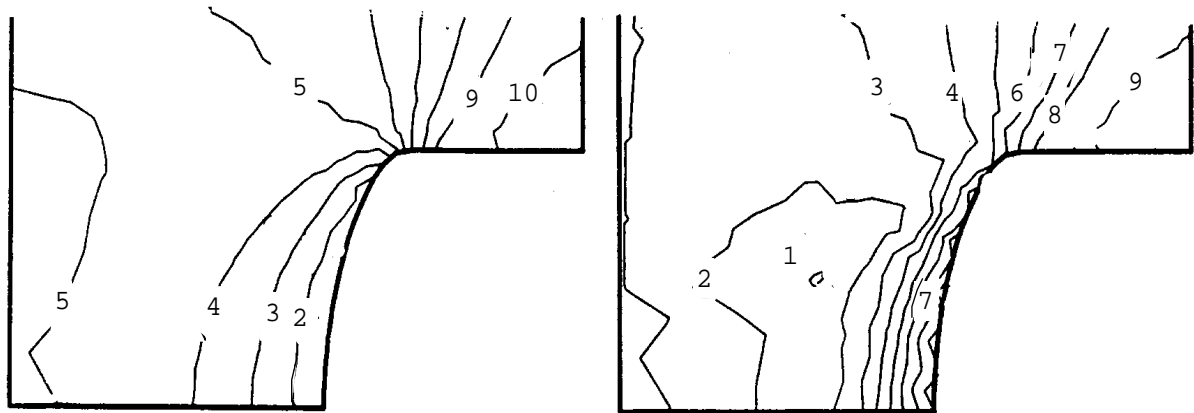


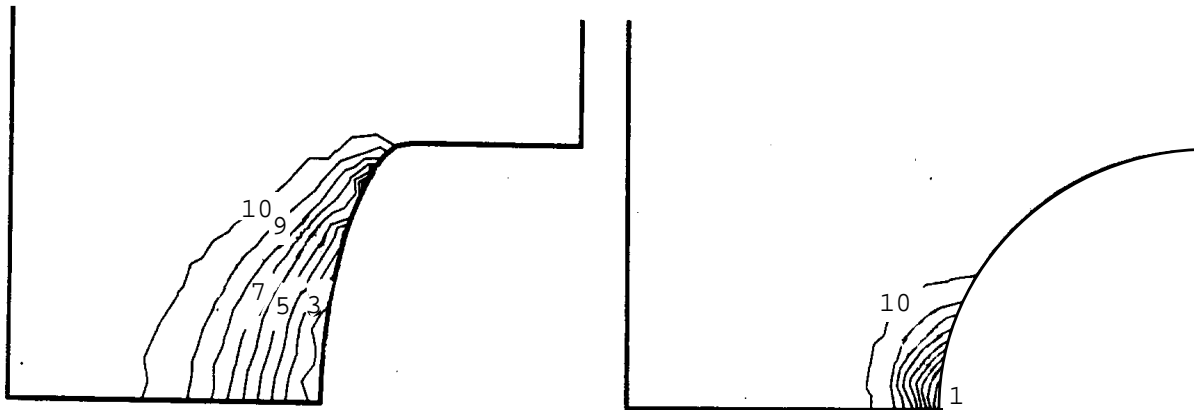
Figure 5.11: Meshes of a.) circularly notched ($r = 9mm$) and b.) statically optimized shape.

In Figure 5.12 the stress redistribution for a statically optimized part is shown. In Figure 5.13 (left) damage is almost constant along the free boundary until the separation point is reached. It is widely spread out for this statically optimized part. Damage is highly concentrated if the circularly notched part is considered.



1: 259 MPa 2: 231 MPa 3: 204 MPa 4: 176 MPa 5: 148 MPa
 6: 120 MPa 7: 92.5 MPa 8: 64.7 MPa 9: 36.9 MPa 10: 9.1 MPa

Figure 5.12: Stress before damage accumulation: $N = 1$ (left) and after $N = 30157$ cycles (right).



1: .97 2: .86 3: .76 4: .65 5: .55 1: .67 2: .59 3: .52 4: .45 5: .38
 6: 0.44 7: .34 8: .23 9: .13 10: .02 6: .30 7: .23 8: .16 9: .09 10: .02

Figure 5.13: Damage after $N = 30157$ cycles, $\sigma_L = 105MPa$ for a statically optimized part (left) and damage after $N = 27010$ cycles, $\sigma_L = 84.5MPa$ for a circularly notched part.

5.6.3 Discussion

With the modified algorithm, the stress redistribution observed experimentally is well modelled. The introduced coupling reduces the effect of mesh dependency.

Damage is highly concentrated in the case of the circular notch and widely spread out in the case of the statically optimized shape.

5.7 Dynamically Optimized Shape

For damage analysis only small errors in the stress-strain field can be tolerated, and therefore a very fine mesh is required allowing only small movements of the free boundary before a remeshing is needed. The damage analyses of the circularly and the statically optimized shape have shown that the damage optimized shape will be at least close to the statically optimized shape. Therefore, for the damage optimization the statically optimized shape (with curvature constraint and B-spline description) was used as start geometry. The substructure technique was adopted and the number of nodes on the free boundary was doubled. The von Mises equivalent stress along the free boundary of this “statically optimized” part is shown in Fig. 5.14. In Figure 5.15 the von Mises stress

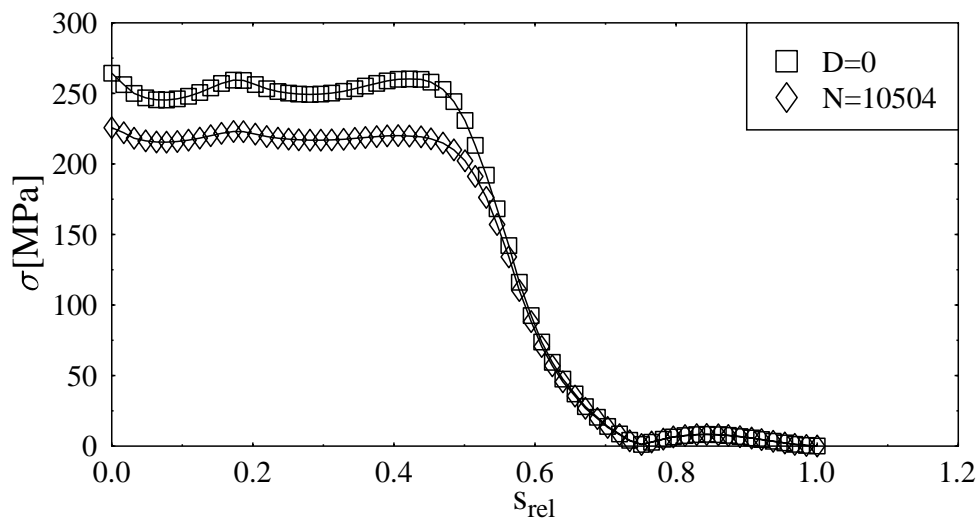


Figure 5.14: Von Mises stress along the free boundary, before damage takes place and after $N = 10504$ cycles (stress redistribution!).

along the free boundary of the statically optimized part is compared with the circularly notched part.

In Figure 5.16 the damage along the free boundary of the statically optimized and the circularly notched part are shown.

Besides the maximum von Mises stress, now two new cost functions were chosen:

- Maximum damage itself at a certain number of cycles was chosen as new cost func-

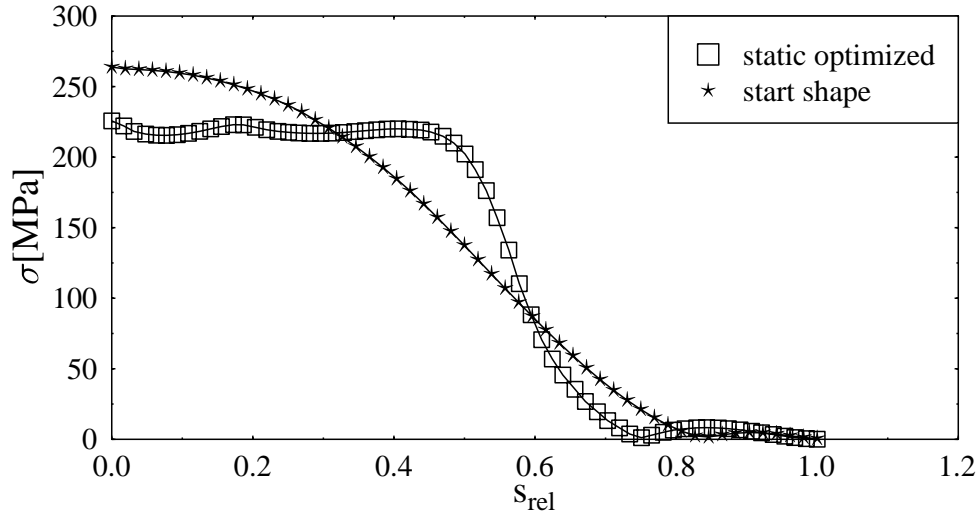


Figure 5.15: Von Mises stress along the free boundary after $N = 10504$ cycles. Comparison of the circularly notched and the statically optimized structure.

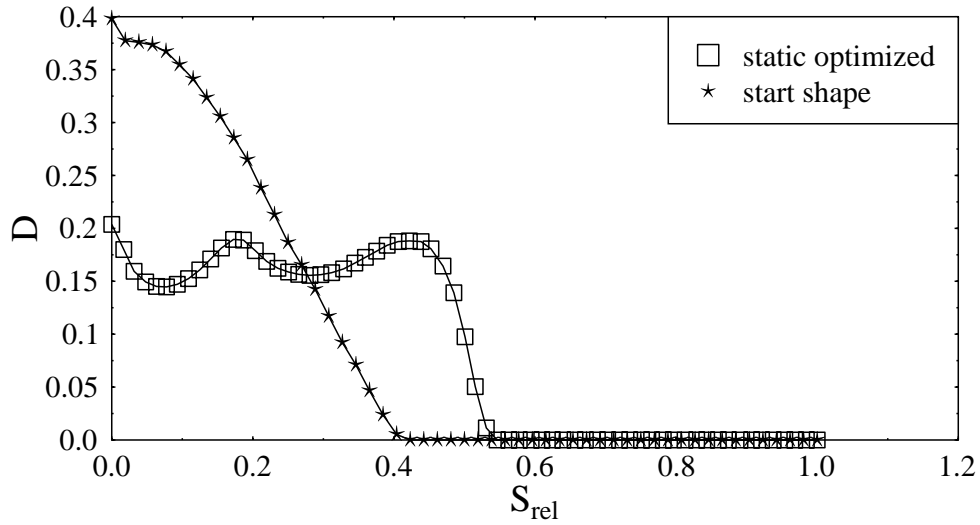


Figure 5.16: Damage along the free boundary after $N = 10504$ cycles. Comparison of the circularly notched and the statically optimized structure.

tion. In the discretised formulation we obtain:

$$f_2(\mathbf{t}) = \max_{i=1..m} D \Big|_{N^*=const} . \quad (5.9)$$

- Damage increment is controlled by the increment of accumulated plastic strain and the effective damage equivalent stress. Therefore, before damage occurs, the maxi-

imum damage equivalent stress was chosen as second new cost function.

$$f_3(\mathbf{t}) = \max_{i=1..m} \sigma^*. \quad (5.10)$$

In both cases we have to consider minimax problems. These problems are handled as described in Section 3.2.2 for minimization of maximum von Mises stress.

5.7.1 Damage Optimization

For a load of $\sigma_L = 100 \text{ MPa}$ the number of cycles until failure ($D = D_C$) of the statically optimized part were calculated. This number ($N^* = 10504$) was fixed and maximum damage along the free boundary was minimized.

In Figure 5.17 the von Mises stress along the free boundary of the damage optimized part is compared with the von Mises stress of the statically optimized part.

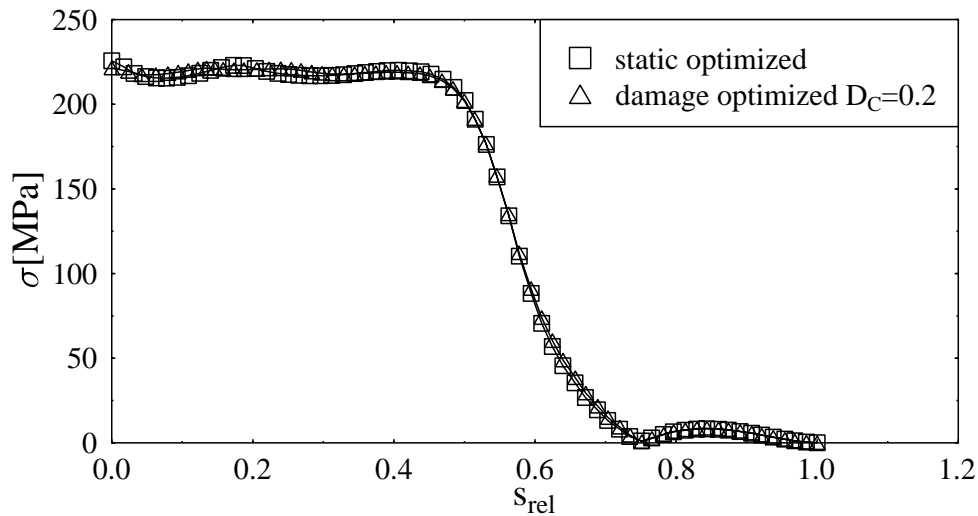


Figure 5.17: Von Mises stress along the free boundary after $N = 10504$ cycles. Comparison of the statically optimized and the damage optimized structure.

In Figure 5.18 the damage along the free boundary of the statically and the damage optimized part are shown.

The oscillation in damage along the free boundary of the statically optimized part is reduced by damage optimization. In von Mises stress there is almost no difference between the two shapes.

The damage optimum was found after 6 iterations; a remeshing was not necessary.

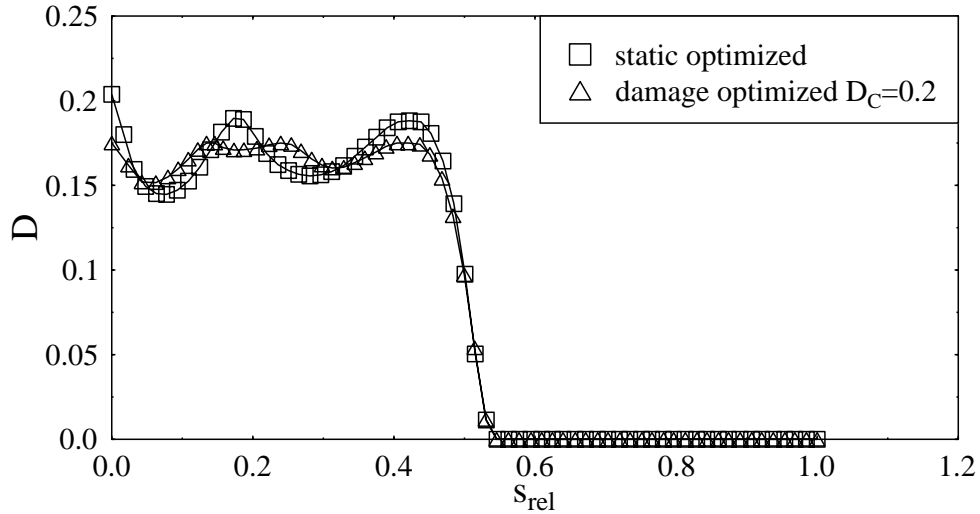


Figure 5.18: Damage along the free boundary after $N = 10504$ cycles. Comparison of the statically optimized and the damage optimized structure.

5.7.2 Damage Equivalent Stress

Damage evolution is controlled by damage equivalent stress. In fatigue, damage equivalent stress at microscale determines the damage evolution. The damage equivalent stress differs from the von Mises equivalent stress by the square root of the triaxiality function. On a mesoscale there is no difference between the von Mises stress and the damage equivalent stress, because $R_V \equiv 1$ on the free boundary (see Section 4.2.3). The microscopic damage equivalent stress may differ, because of incompressibility during plasticity of the material [55, 56].

The maximum damage equivalent stress was determined before damage evolution has started. The cost function which was minimized was this maximum damage equivalent stress. After optimization, the σ^* part was loaded once again with $\sigma_L = 100\text{MPa}$ for $N = 10504$ cycles in order to compare the stress and damage distribution with the optimization results of the first new approach.

In Fig. 5.19 the von Mises stress of the statically optimized part is compared with the von Mises stress along the σ^* -optimized part.

In Figure 5.20 the damage along the free boundary of the statically and the σ^* -optimized part are shown.

The optimum was achieved after one remeshing and 8 iterations.

The results of the σ^* -optimization are very close to the results of the damage optimization

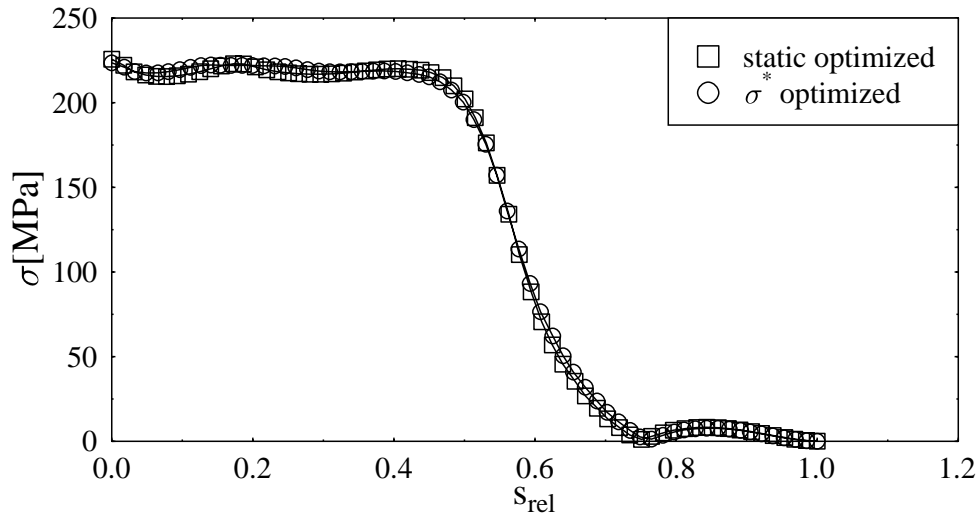


Figure 5.19: Von Mises stress along the free boundary after $N = 10504$ cycles. Comparison of the statically optimized and the σ^* -optimized structure.

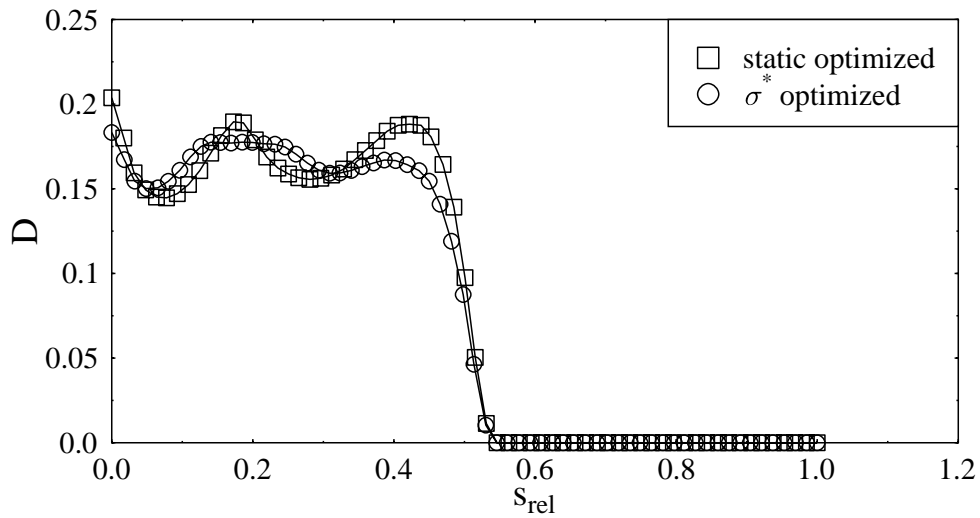


Figure 5.20: Damage along the free boundary after $N = 10504$ cycles. Comparison of the statically optimized and the σ^* -optimized structure.

in the last subsection. Again, almost no difference in von Mises equivalent stress can be found, and the oscillation in damage is reduced.

5.7.3 Discussion

The oscillation in damage of the statically optimized part was remarkably reduced by optimization with the two new cost functions.

The following reasons can be responsible for this:

- The now modelled stress redistribution,
- triaxiality at microscale or
- numerical approximation problems.

The stress redistribution is considered if damage itself is minimized. σ^* is minimized before damage takes place. Both new cost functions lead to very close results, therefore the observed effect cannot be due to stress redistribution.

The negligible effect of stress redistribution can be understood, if one notices, that damage evolution is controlled by the **effective** damage equivalent stress. During stress redistribution the effective stress is stays high because of the quotient ($1 \Leftrightarrow D$).

The following considerations will help to clarify, whether the oscillations are due to numerical problems or to triaxiality at microscale.

There is a slight, appropriate oscillation in the von Mises stress of the statically optimized part (see Fig. 5.14). If a B-spline description of the free boundary is used, slight oscillations in von Mises stress are always observed [31]. The observed oscillations in stress are about 6%, which is normally negligible. In this work, because of the stress sensitivity of the damage analysis, only errors in stress $e_\sigma^* < 5\%$ are tolerated.

The structure analysis of the statical optimization was carried out with “only” 31 design nodes on the free boundary. The doubling of the nodes - necessary for the desired stress accuracy - was not considered in the static optimization procedure.

Therefore, the statically optimized part was statically optimized a second time but with the refined, substructured mesh. In Fig. 5.21 the von Mises stress along the free boundary of the part that has been statically optimized twice is compared with the von Mises stress of the “statically optimized” part.

It is remarkable that the damage oscillation in Fig. 5.22 is reduced in the same manner as if the two new cost functions are used.

In conclusion, the influence of triaxiality is negligible in this case. This was already mentioned for 2D in Section 4.3.4 by replacing the microscopic variables in the case of the uncoupled analysis.

Finally, it can be concluded that the optimization results of the statical, the damage and

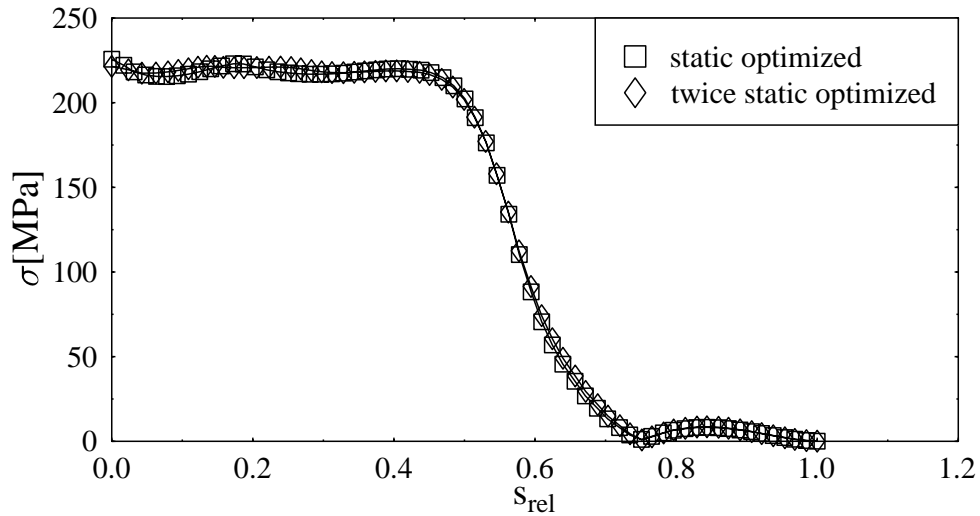


Figure 5.21: Von Mises stress along the free boundary after $N = 10504$ cycles. Comparison of the statically optimized and the structure that was statically optimized twice.

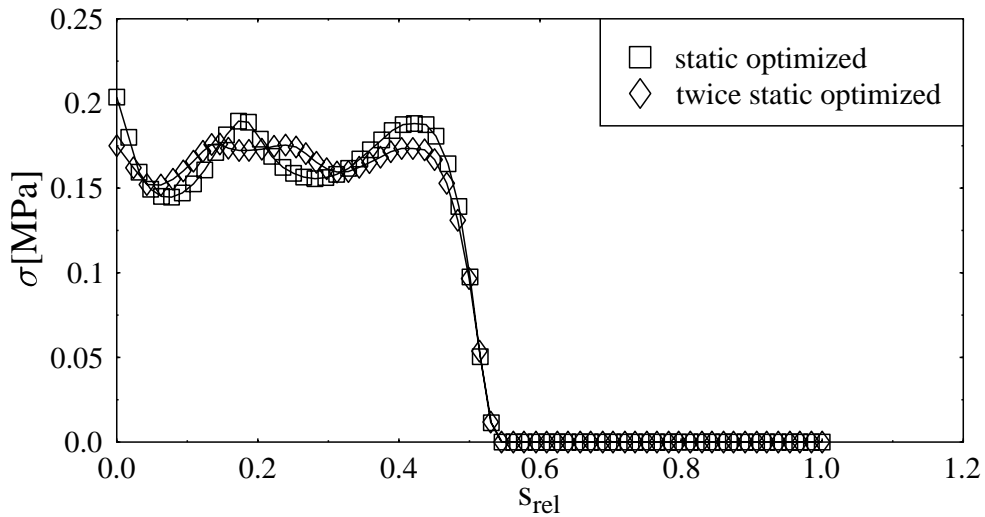


Figure 5.22: Von Mises stress along the free boundary after $N = 10504$ cycles. Comparison of the statically optimized and the structure that was statically optimized twice.

the σ^* optimization are really close. This is also demonstrated in the S-N-diagram (Fig. 5.23).

For a practical use there is no difference and a static optimization is recommended. The situation may change for 3D problems, because triaxiality becomes more important. In this case, the importance of stress redistribution has to be checked also. Maybe a static

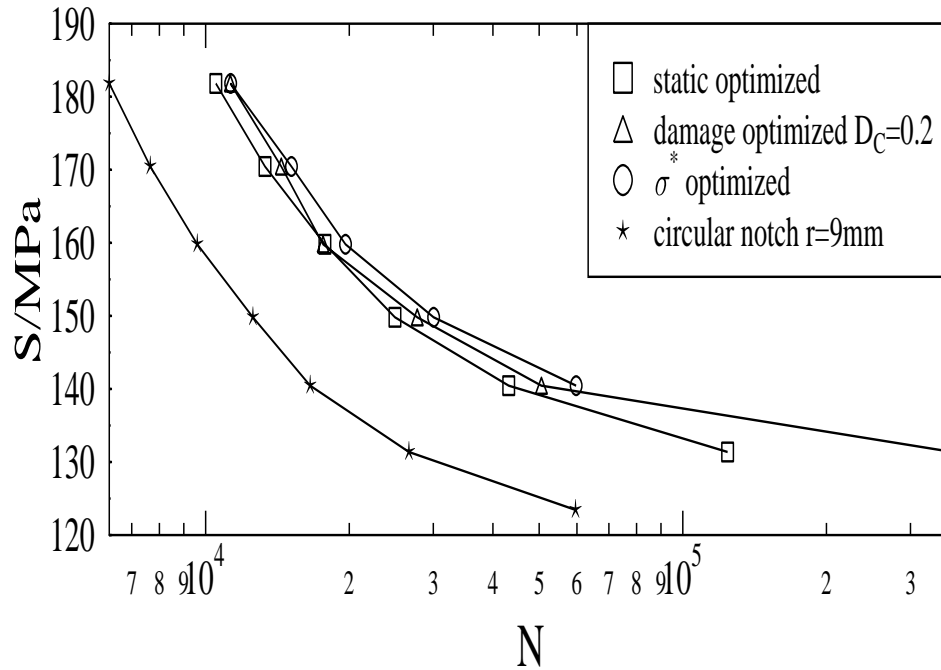


Figure 5.23: S-N Diagram for parts with statically optimized, damage equivalent stress minimized and damage minimized shape.

optimization with σ^* instead of the von Mises equivalent stress (considering the triaxiality) is sufficient.

The new concept becomes particularly valuable if nonproportional loadings have to be considered. In this case, the point of failure and the point with maximum stress may differ. In the case of nonproportional loadings a less loaded point (but for a longer time above the threshold) can cause the failure of the structure and we therefore expect totally different optimization results.

Chapter 6

Experimental Investigations

All experiments were carried out with a 1000kN SCHENCK hydraulic pulser. It is an inherent feature of lifetime tests (especially for low loads near the fatigue limit) that there is a great scatter in results. In order to minimize this scatter, all influencing factors were tried to be held constant (e.g. manufacturing process, residual stresses, surface roughness). The effect of designing the free boundary was thus extracted.

The determination of the material properties was carried out at the same time as the numerical optimization. For static optimization the material properties (E , ν) are almost the same, therefore only very small differences in comparison to the stainless steel are expected.

Here, the principal determination of the damage constants is studied. And the CDM model is compared with experimental results for smooth specimens.

The damage constant will differ significantly for different materials. A damage optimization with the material properties determined here will be published in [37].

6.1 Material Properties

The material used for the experiments was a high strength steel 30CrNiMo8. This material was chosen, because it shows a very homogeneous texture (see Fig. 6.1) and is also often used in industry for large, highly loaded machine parts.

All specimens used in the experiments are out of the same manufacturing process (Charge: 263160/92). The material was directly supplied by the manufacturer THYSSEN STAHL AG.

Figure 6.1: Micrograph of 30CrNiMo8. No difference was found in texture for longitudinal and transversal intersections.

The chemical composition is:

Ingredients	C	Si	Mn	P	S	Cr	Mo
Weightpercent	0.33	0.18	0.53	0.024	0.002	2.08	0.35
Ingredients	Ni	V	W	Al	B	Co	Cu
Weightpercent	2.1	<0.01	0.02	0.021	<0.0004	0.025	0.08

6.1.1 Preparation of the Specimens

There was a hardening at 860⁰C (oil cooled) and after this a tempering at 600⁰C for two hours (air cooled).

By this hardening process 333 ± 5 HRB were reached.

After manufacturing and polishing the specified parts (Geometries see Fig. 6.2), residual stresses were minimized by annealing at 570⁰C for three hours in vacuum.

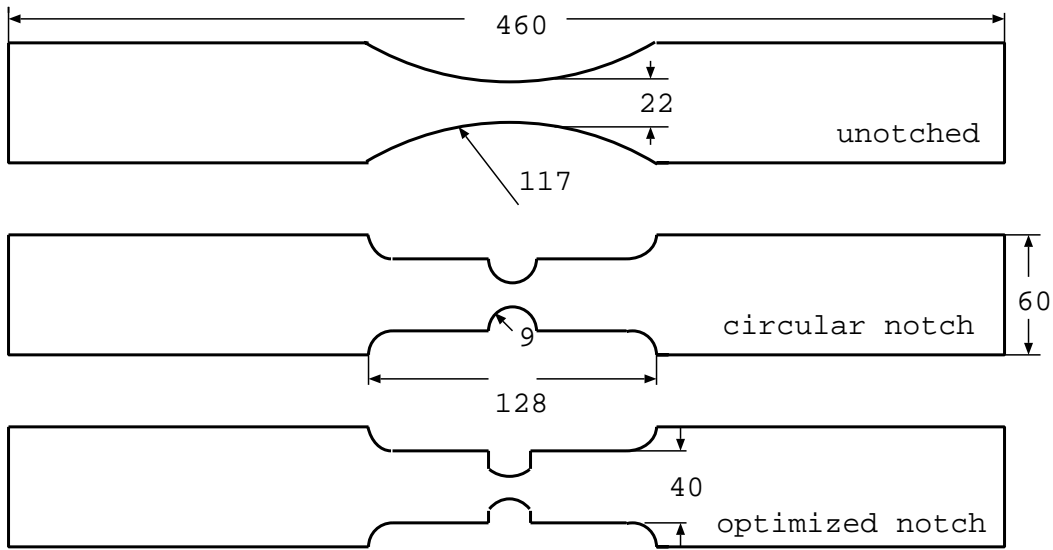


Figure 6.2: Geometry of the used specimens, sizing in mm.

6.1.2 Material Constants

The following material parameters are necessarily measured (see Appendix B for detailed experimental results) to use the continuum damage mechanics approach:

- **Elasticity**

Young's modulus ($E = 216291 \pm 4620 \text{ MPa}$) and Poisson's ratio ($\nu = 0.3$)

- **Plasticity**

Fatigue limit ($\sigma_f = 484 \text{ MPa}$), yield stress ($\sigma_y = 865.9 \pm 18.4 \text{ MPa}$) and ultimate stress ($\sigma_u = 1020.6 \pm 14.2 \text{ MPa}$)

- **Inclusion**

Perfect plasticity ($\sigma_y^u = \sigma_f$)

- **Damage** Damage constant ($S = 58$), plastic strain threshold ($p_D = 21$) and critical damage ($D_C = 0.2$)

The given values are mean values. The easiest test to determine the damage constant is the tension test with unloadings. Fig. 6.3 shows such a single tension test. The values measured by such tension tests ($S \approx 2$) differ significantly from the value in the table. The explanation is an inhomogeneous plastification found in materials like the considered

30 CrNiMo8 [24]. In this case, strain driven VLCF-tests are recommended. In Appendix B, some hystereses and the p-D-diagram for such a strain driven tension test ($\Delta\varepsilon = 1.2\%$, $f = 0.2Hz$, $N_B = 1744$) are shown. The mentioned VLCF measurements [69] show a

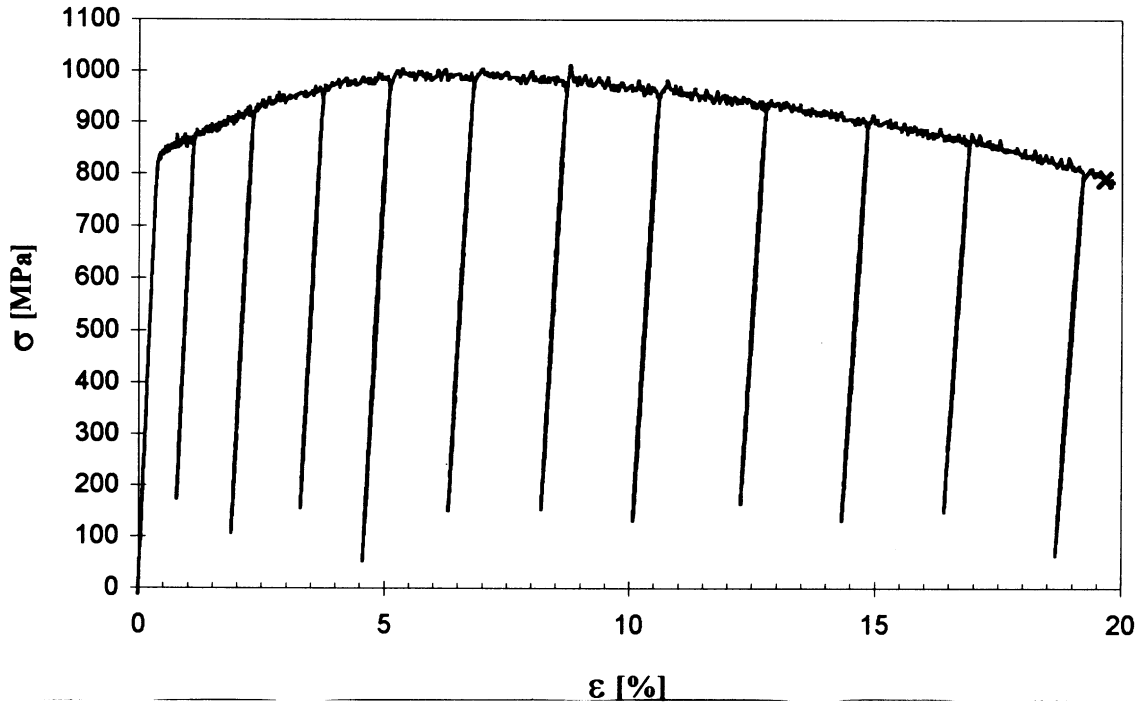


Figure 6.3: Tension test with unloadings. Strains are measured with a SCHENCK DSA 25/20 strain clip.

crack closure parameter $h = 0.5$ for the considered material. Crack closure has not been implemented into the algorithm until now.

6.2 Photoelastic Experiments

One of the main characteristics of the damage mechanics concept is the proposed stress redistribution.

A stress redistribution during fatigue life is found experimentally by the use of photoelasticity. A reflexion method was used, therefore the specimens were covered by a photoelastic sheet ($PS \Leftrightarrow 1$, $h_c = 1mm$, Measurements Group). The stress-optic law provides a relation between the retardation of a loaded photoelastic material and the principal stresses. Using a reflexion method, it is assumed that specimen and coating are equally strained. In this case the stress-optic law can be rewritten in the following form:

$$\varepsilon_1^c \Leftrightarrow \varepsilon_2^c = \varepsilon_1 \Leftrightarrow \varepsilon_2 = \frac{1 + \nu}{E} \frac{f_\sigma}{2h_c} \frac{\delta}{\lambda}, \quad (6.1)$$

with

$$\begin{aligned} f_\sigma = \frac{\lambda}{C}: & \text{ the material fringe value,} \\ \delta: & \text{ the retardation and} \\ h_c: & \text{ the thickness of the coating.} \end{aligned}$$

There was no need to get the directions of principal strains, so circularly polarized light was used. This means the isochromates (lines of equal principal strain difference) are not disturbed by the isoclines (lines of equal principal strain direction). The whole set-up is demonstrated in Fig. 6.2. By polarizing the light, retarding it at the $\lambda/4$ -plates and according to the stress-optic laws and interfering it at the analyzer, the following equation is derived for the amplitude of the electric field [98]:

$$E(t) = \sqrt{2}E_0 \cos(\omega t \Leftrightarrow 2\alpha) \sin\left(\frac{\Delta}{2}\right), \quad (6.2)$$

with

Δ : the retardation in radians.

The intensity of the emerging light is observed:

$$I(t) = 2E_0^2 \cos^2(\omega t \Leftrightarrow 2\alpha) \sin^2\left(\frac{\Delta}{2}\right). \quad (6.3)$$

Time averaging eliminates the high frequency term. Eq. 6.3 shows in particular that the intensity is zero if

$$\frac{\Delta}{2} = n\pi, \quad (6.4)$$

with

n: fringe order.

In the experiment a white-light source is used. Therefore in almost any place Eq. 6.4 is satisfied for a special wavelength:

$$\Delta = nk\delta, \quad (6.5)$$

with

λ : wavelength, $k = \frac{2\pi}{\lambda}$: wave propagation factor.

and the complementary color is observed in the pattern.

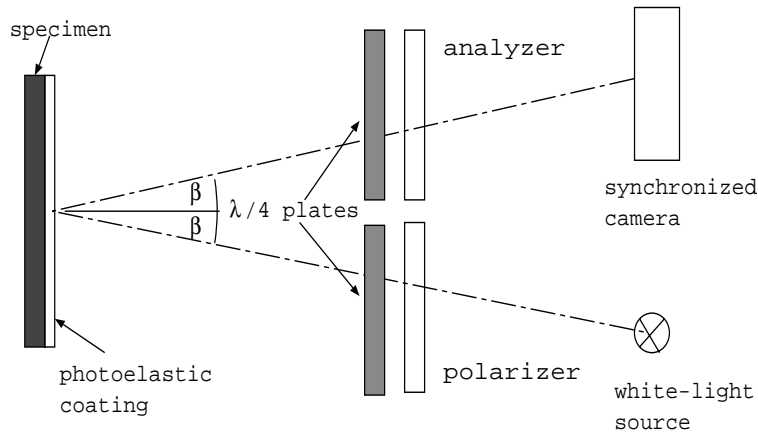


Figure 6.4: Photoelastic experiments: reflexion method with white circular polarized light, dark field: polarizer and analyzer are crossed.

6.2.1 Camera Synchronization

In this case the major interest was to get at least a qualitativ impression of the stress/strain distribution and redistribution during the fatigue test without disturbing the experiment.

For this purpose the camera (NIKON F-801) had to be synchronized to the actual signal of the hydraulic pulser.

Some standard techniques for dynamic recording can be found in [98]. For the discussed application a simple and inexpensive alternative was developed.

The synchronization of the camera was achieved by the following procedure: In a primary experiment the delay of camera and electronic was measured by taking a photo of a display which was driven from a counter measuring the time after the start signal for the photo was given. A constant delay can be found for every adjustment of the camera with a tolerance of less than $\Delta t_1 = \pm 1ms$. The synchronization is now achieved by adding a second delay so that the next point of maximum load is reached:

$$\Delta t_2 = \frac{1}{f} \Leftrightarrow \Delta t_1 \quad (6.6)$$

with

f : the load frequency of the fatigue test.

A schematic diagram of the synchronization is found in Fig. 6.5. Certainly, instead of detecting the point of maximum load, any fixed point can be used as start signal if the second delay is determined adequately.

6.2.2 Discussion of the Results

All colored photoelastic figures are collected in Appendix B.3. Eq. 6.1, 6.3 and 6.5 show that the isochromats are colored lines of the same difference of principal strain (See e.g. [97] for the assignment of the principal strain differences to the colors.).

For a quantitative strain-stress field analysis at least two independent measurements are needed, because only the difference of principal strain is detected. Here only one picture at the same time was available. Therefore the analysis of the results is carried out only qualitatively.

If elastic behavior can be assumed the principal strain difference is easily transferred to principal stress difference by the use of Hooke's law. At the free boundary and at points of vertical/horizontal symmetry one principal stress vanishes and the second principal stress can be found directly out of the principal strain difference found in the pattern. From the comparison between Fig. B.4.a and Fig. B.4.c, it is obvious that the stress is constant along the optimized shape between the separation points. This is characteristic for the static optimization result (FSD). It has to be mentioned that the red color along the boundary and the red color in the middle of the part are of different order. This means "high" stress along the free boundary and low stress in the middle of the part. In Fig B.4.b and B.4.d it is not allowed any more to determine the stress directly from the visualized strain patterns. These figures have to be analyzed more carefully. In B.4.d there are several orders in strain along almost the whole free boundary. In B.4.b there is also higher straining now, but more localized at the root of the notch. This high straining is not connected with high stresses. It is worth mentioning that in the middle of the part the low strain has vanished. As a transformation of the strain to the stress with Hooke's law is still allowed in the middle of the part, this means the stress has increased here, whereas at the boundary there is a large straining without almost any stress. This is well explained by the CDM-concept. The large straining without carrying load is a result of the high damage accumulation in this region.

This stress redistribution is found really early during lifetime. The number of cycles at failure was $N_B = 20901$ e.g. in the case of the circularly notched part, the number of cycles at first stress redistribution seen in the photoelastic experiments was $N_0 = 13000$ (Fig. B.4.b was taken after $N = 14659$ cycles).

6.3 Lifetime Tests

First a comparison of experimental results and the numerical calculation is shown for unnotched specimens. Afterwards the lifetimes of the different shapes are experimentally compared using an engineering statistical standard method.

6.3.1 Comparison of Experimental and Numerical Results

In Fig. 6.6, the numerical (CDM-approach) and experimental results are compared. In the figure we find one curve for the start of damage evolution (N_o), one curve for the breakdown calculated by the original *Lemaitre*-algorithm and one curve calculated by the modified algorithm. Using the modified algorithm the lifetimes are always shorter, because of the damage accompanied by larger straining at mesoscale. However, the difference to the original algorithm is small. The start of damage evolution was not observed during experiments - this would be valuable for the next term. Therefore, only the number of cycles at breakdown are compared. The experimental data is well approximated by the calculation.

Scattering of results is an inherent feature of all lifetime tests, even if a careful specimen preparation has been carried out. Therefore a statistical analysis of the results is necessary if the lifetimes of different shapes are compared.

6.3.2 Statistical Analysis of Results

A standard concept to analyze lifetime tests in a statistical manner is the so-called $\arcsin \sqrt{p}$ -transformation. In [22] a comparison of several techniques analyzing fatigue data is found. The mentioned transformation was chosen, because it provides reasonable results for the S-N-diagram with only few experiments on every load level. Usually one assumes a straight line for the S-N-diagram in the area of time strength. This straight line buckles horizontally at the fatigue strength ($N = 2 \cdot 10^6 \Leftrightarrow 10^7$, $N_B = 2 \cdot 10^6$ was chosen for determination of the fatigue strength, here.). Both areas can be analyzed separately by the $\arcsin \sqrt{p}$ -transformation. The statistical analysis for the experiments in the area of time strength is briefly described, here. A description of the analogous procedure in statistical fatigue limit determination is found in [60].

Let n be the number of specimens broken at one load level. These n results are ordered with increasing lifetime. The crack probability assigned to every test result is:

$$P = \frac{i}{n} \cdot 100\% \quad \text{if } i < n \quad \text{and} \quad P = \left(1 \Leftrightarrow \frac{1}{2n}\right) \cdot 100\% \quad \text{if } i = n. \quad (6.7)$$

The transformation is used to determine the lifetime for an arbitrary crack probability:

$$\lg N_B = a_t + b_t \arcsin \sqrt{P}. \quad (6.8)$$

The experimental results are fitted by the usual least square method.

In order to connect the results of a specified crack probability to a straight line, the original Wöhler (see Eq. 2.4) approach was chosen:

$$\lg N_B(P) = a \Leftrightarrow b\sigma(P). \quad (6.9)$$

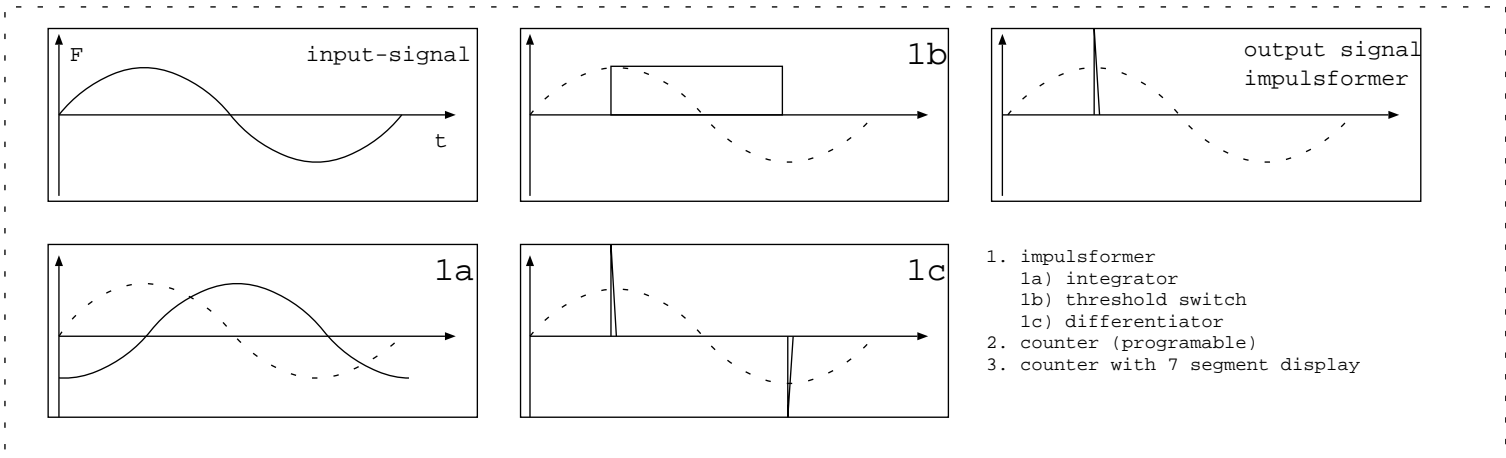
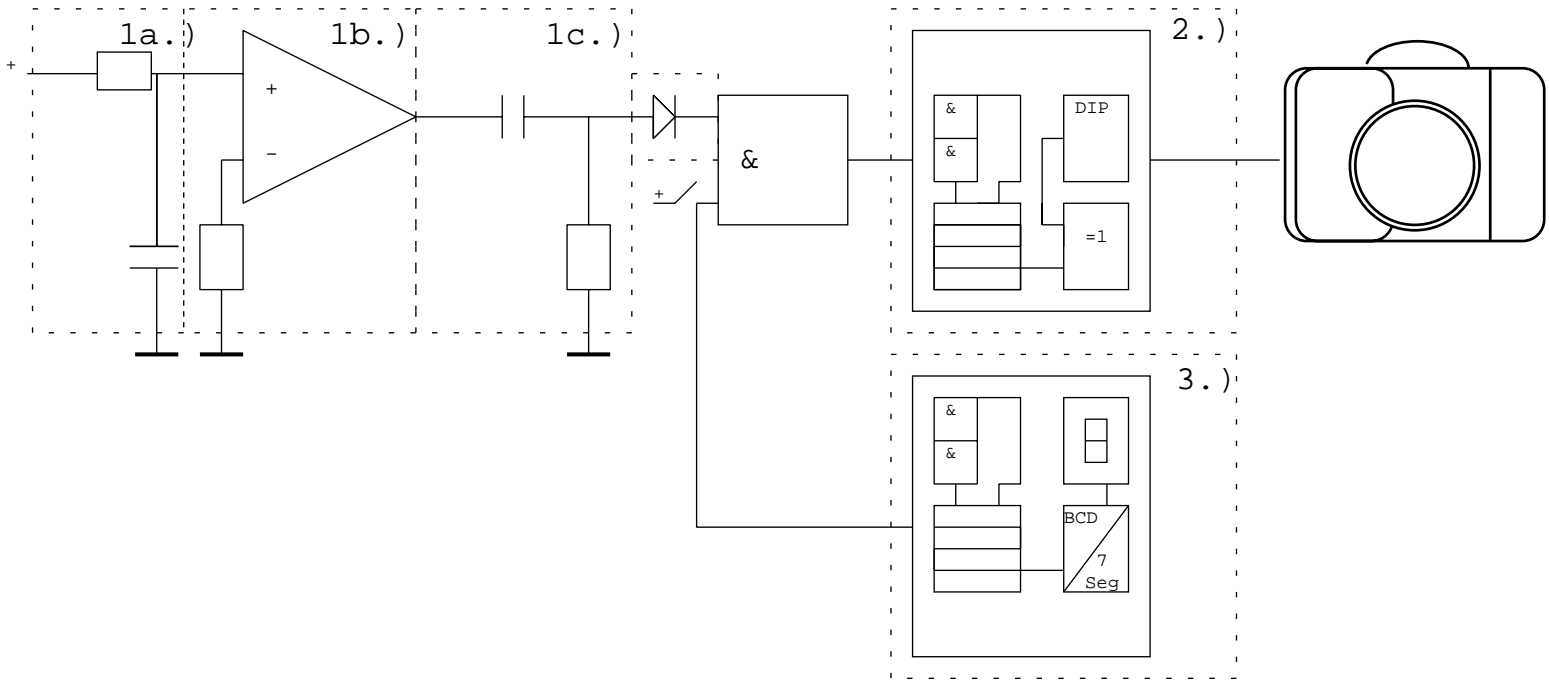
The regression line is found by a second least square fitting.

It is recommended to use at least 3-4 load levels with at least 5-7 specimens at each level. This means at least 20 tests for one S-N-diagram.

6.3.3 Experimental Comparison of Different Shapes

Fig. 6.7 shows $S \Leftrightarrow N$ -diagrams for 50% crack probability. The lifetime for a part with optimized shape is remarkably increased in comparison to a circularly notched part for any load level. In Appendix B.2.2 the data of the single tests is collected.

Figure 6.5: Synchronization of the camera.



- 1. impulsformer
- 1a) integrator
- 1b) threshold switch
- 1c) differentiator
- 2. counter (programmable)
- 3. counter with 7 segment display

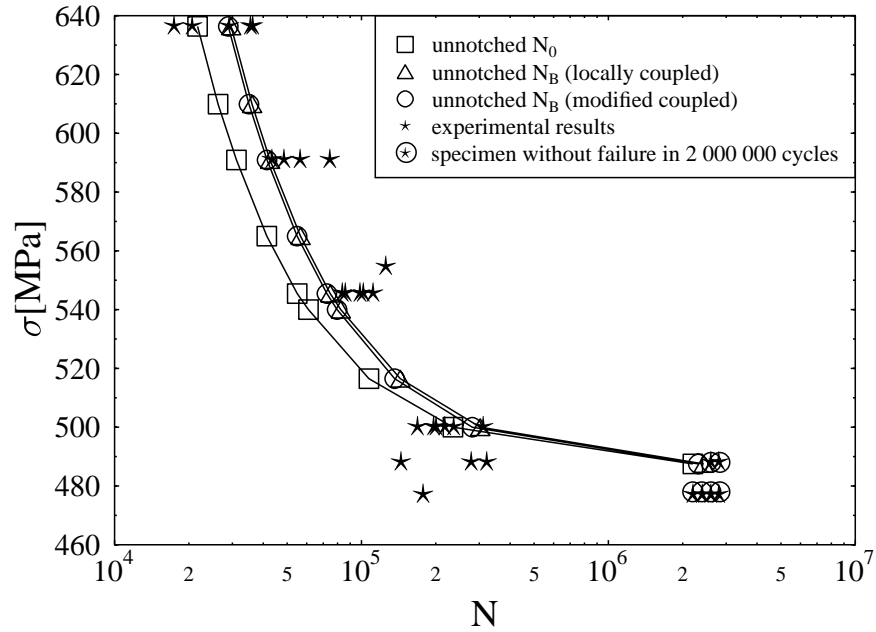


Figure 6.6: S-N-diagrams for unnotched specimens. Comparison of experimental and numerical (CDM-approach) results.

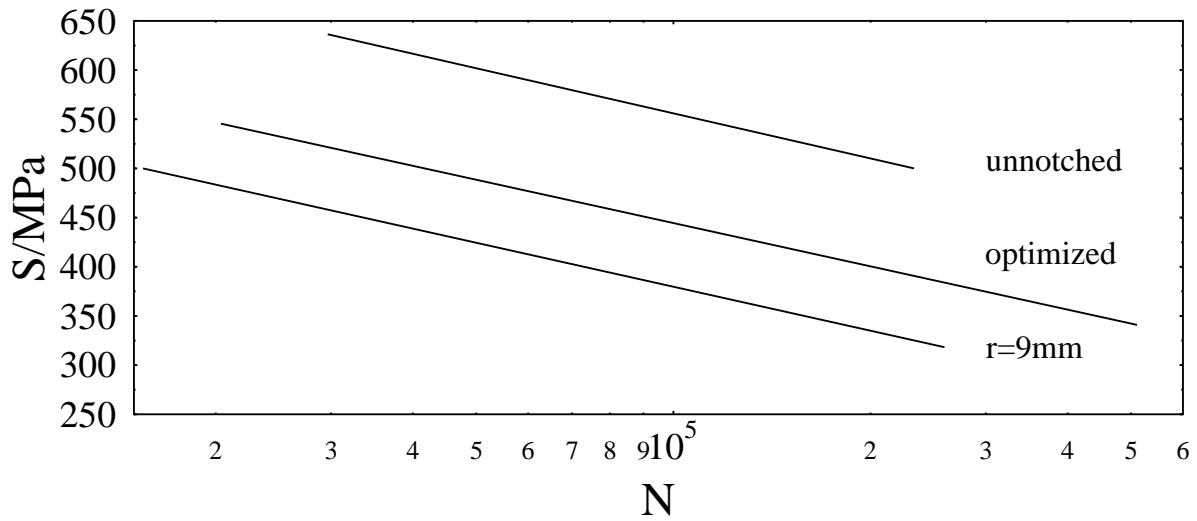


Figure 6.7: S-N-diagrams for 50 % crack probability.

Chapter 7

Conclusion

The usually used engineering lifetime determination with fatigue notch factors provides only poor results if the loading situation is complex. Problems with e.g. changing load levels are mentioned. In addition, in photoelastic experiments a stress redistribution was observed during fatigue life. This stress redistribution has not been taken into account for shape optimization of dynamically loaded parts failing by fatigue until now.

The concepts of Continuum Damage Mechanics were used to model this stress redistribution. With these concepts, a discretization in time considering changing loading and material conditions is possible.

Damage evolution is connected with plasticity. Especially in high cycle fatigue there is no plasticity on a macroscale. This problem is overcome by introducing a two-scale model to characterize fatigue behavior. Elastic behavior on a macroscale and elasto-plastic behavior on a microscale are assumed. Damage is connected with breaking of atomic bonds, plasticity with slips. This means, besides the deviatoric part of the stress tensor, also the hydrostatic part influences damage evolution. This is taken into account by the introduction of a triaxiality function.

In contrast to *Lemaitre's* work not only the microelement is damaged. Here, the damage of the microelement is directly transferred to the mesoelement which is represented by the finite element. This direct transfer is encouraged by the initial conditions $D = D^\mu = 0$ (initial damage is zero for micro- and mesoelement) and by the final conditions (failure of the microelement causes failure of the whole mesoelement). The feature may be modified according to further experimental studies.

For dynamical shape optimization, the minimization of damage at a certain number of cycles and the minimization of damage equivalent stress (before damage evolution starts) were chosen as new cost functions.

For optimization, there are two differences in comparison to the minimization of von Mises

equivalent stress (=static optimization), if proportional loadings are considered:

- Triaxiality at microscale and
- Stress redistribution.

The considered numerical example shows that both effects are negligible in this case. The numerical results of the three cost functions: minimizing maximum von Mises stress, minimizing maximum damage equivalent stress and minimizing maximum damage at the free boundary are very close.

For 3D-problems the influence of triaxiality may arise.

The highly concentrated damage for the circularly notched part is widely spread out for the optimized parts. The damage is almost constant along the free boundary between the separation points. Small oscillations in damage along the shape are due to the B-spline approximation of the free boundary.

Completely different optimization results are expected for nonproportional loadings. The described concept is - in principle - also adoptable in this case.

The lifetime tests show that the CDM-approach fits the experimental data very well. Statistically analyzed lifetime experiments for circularly notched, unnotched specimens and specimens with optimized shape show a remarkably increased lifetime of the optimized parts.

Appendix A

Damage Mechanics

A.1 Proportional Loading

A loading on a particular structure (Ω) is considered to be proportional if the stress field can be written as a product of a tensor depending only on the considered point (M) and a scalar function depending only on time:

$$\boldsymbol{\sigma}(M, t) = \mathbf{S}(M)\tau(t) \quad (\text{A.1})$$

It can easily be shown [56] that in the case of a proportional loading the principal stress directions do not change in time. The triaxiality ratio and also the triaxiality function also remain constant in time.

A.2 Fatigue Crack Growth

On a microscale we consider a distribution of fatigue cracks with area s_i (see Fig. A.2). In a simplest case damage is defined as:

$$D = \frac{\sum_{i=1}^n s_i}{l^2}, \quad (\text{A.2})$$

with the rate:

$$\dot{D} = \frac{\sum_{i=1}^n \dot{s}_i}{l^2}. \quad (\text{A.3})$$

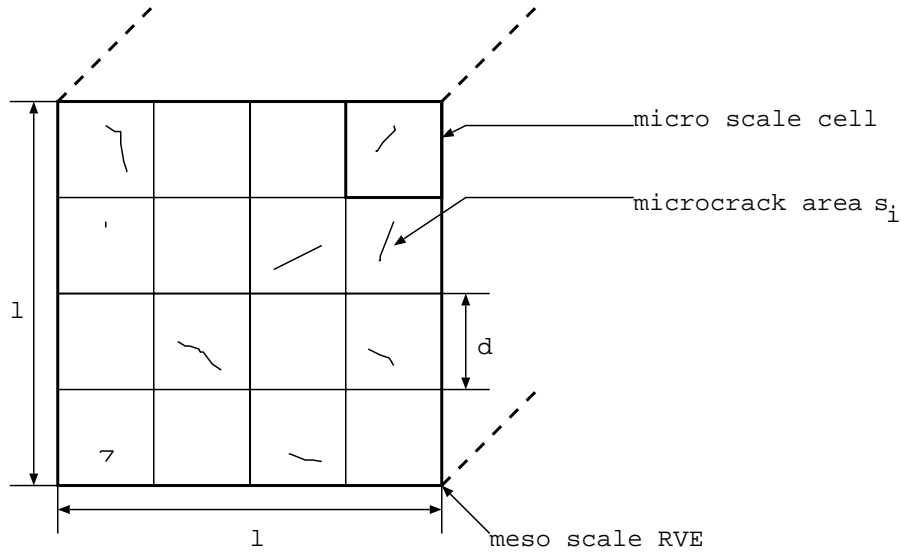


Figure A.1: Micro-meso element for brittle fatigue crack growth

The crack growth of one crack may be expressed as a function of the strain energy release rate of one cell \dot{G}_i by the use of *Paris'* law of fatigue crack growth (see Eq. 2.1). We reduce our considerations to a two-dimensional problem with the crack length $2a$ and the crack increment $\frac{\delta a}{\delta N}$ per cycle. The exponent in Paris law is $m \simeq 4$ for most metallic materials. The crack increment per cycle can be interpreted as the integral of the crack rate over one cycle. Therefore the rate of a is derived by differentiation of Paris law:

$$\dot{a} = mCK^{m-1}\dot{K} \quad (\text{A.4})$$

If we assume that the crack i has the width e_i we get the following expressions for cell i :

$$K = (EG)^{\frac{1}{2}}, \quad \dot{K} = \frac{E^{\frac{1}{2}}}{2}G^{-\frac{1}{2}}\dot{G} \quad \text{and} \quad \dot{s}_i = e_i\dot{a}_i \quad (\text{A.5})$$

where

G : strain energy release rate corresponding to a crack with area s .

So the crack area rate has the following expression:

$$\dot{s}_i = mCe_iE^{\frac{m}{2}}G_i^{\frac{m}{2}-1}\dot{G}_i \quad (\text{A.6})$$

A relation between G_i and Y_i can be found using their relations to the elastic strain energy:

$$G_i = \frac{\partial W_i^e}{\partial s_i} \quad \text{and} \quad Y_i = \Leftrightarrow \frac{\partial w_i^e}{\partial D_i}. \quad (\text{A.7})$$

with

$$W_{ei} = d^3w_{ei}. \quad (\text{A.8})$$

The following expression results:

$$G_i = \Leftrightarrow \frac{1}{2} \frac{\partial(w_i^e d^3)}{\partial D_i} \frac{\partial D_i}{\partial s_i} \quad (\text{A.9})$$

where

$$D_i \simeq \frac{s_i}{d^2}, \quad G_i = Y_i d, \quad \dot{G}_i = \dot{Y}_i d. \quad (\text{A.10})$$

The following expression is obtained by inserting in Eq. A.6:

$$s_i = m C e_i E^{\frac{m}{2}} d^{\frac{m}{2}} Y_i^{\frac{m}{2}-1} \dot{Y}_i \quad (\text{A.11})$$

The damage rate is:

$$\dot{D} = \frac{\sum \dot{s}_i}{l^2} = \frac{m C E^{\frac{m}{2}} d^{\frac{m}{2}}}{l^2} \sum_{i=1}^n e_i Y_i^{\frac{m}{2}-1} \dot{Y}_i. \quad (\text{A.12})$$

With the assumption that all the n cracked cells have the same strain energy density release rate, the homogenized strain energy density release rate for the RVE is:

$$Y = n Y_i \quad \text{and} \quad \dot{Y} = n \dot{Y}_i \quad (\text{A.13})$$

and the further assumption that the width is equal for all cracks:

$$\sum_{i=1}^n e_i Y_i^{\frac{m}{2}-1} \dot{Y}_i = n e Y_i^{\frac{m}{2}-1} \dot{Y}_i = e n^{1-\frac{m}{2}} Y^{\frac{m}{2}-1} \dot{Y}, \quad (\text{A.14})$$

$$\dot{D} = \frac{m C E^{\frac{m}{2}} d^{\frac{m}{2}} e}{l^2 n^{\frac{m}{2}-1}} Y^{\frac{m}{2}-1} \dot{Y}. \quad (\text{A.15})$$

It can be seen from Eq. A.15 that for $m \simeq 4$ the damage rate is an increasing function quasi proportional to the strain energy release rate and proportional to its rate \dot{Y} .

A.3 Failure in Micro-Mesoscale

In 4.3.2 it is shown that a microelement will fail, if the damage variable reaches its critical value:

$$D_c^\mu = D_{1c} \frac{\sigma_u^2}{\sigma_y^{\mu^2} R_v^\mu} \leq 1 \quad (\text{A.16})$$

The strain energy release rate at the mesoscale corresponding to a microcrack of surface $\delta A = d^2$ is:

$$G = \Leftrightarrow \left. \frac{\delta W}{\delta A} \right|_{\sigma=const.} \quad (\text{A.17})$$

On the other side $\Leftrightarrow \delta W/2$ is also the energy dissipated in the inclusion by the damaging process at constant stress

$$G(\delta A) = \frac{d^3 \int_0^{D_c} Y dD}{\delta A} \quad (\text{A.18})$$

assuming a constant strain energy release rate (Y_c):

$$G(\delta A) = Y_c D_c d. \quad (\text{A.19})$$

Another relation comes from comparing the energy dissipated in a damage process due to microcrack initiation and the energy dissipated to produce the same crack through brittle fracture mechanics:

$$Y_c D_c d^3 = G_C d^2 \quad (\text{A.20})$$

where

G_C : is the toughness of the material

Comparing relation A.19 and A.20 shows that $G_C = G(\delta A)$. So the criterion for microcrack initiation is also the criterion for crack instability on a mesoscale.

Appendix B

Experimental Results in Detail

The parts were delivered with a circular profile and a length of 460 mm. These parts were numbered with arabic figures. Out of every circular profile part three flat bars were manufactured and numbered “A”, “B” and “C”.

The tension tests and the VLCF tests for the determination of the damage constants were carried out with unnotched axisymmetric specimens. In Fig. B.1 the geometry is shown.

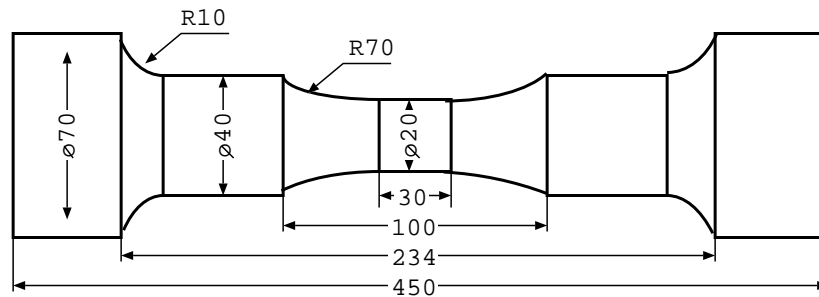


Figure B.1: Geometry of the axisymmetric specimens.

B.1 Tension Tests

specimen	HRB	E/MPa	σ_y/MPa	σ_u/MPa	σ_R/MPa
21B	298	211367	863.6	1018.2	854.5
18A	306	214346	868.2	1018.2	827.3
20C	302	216166	859.1	1009.1	835.0
13A	317	217197	900.1	1048.3	850.7
16A	298	213891	860.2	1020.5	795.3
17A	306	224782	845.1	1010.7	780.3

Mean values/standard deviation:

E/MPa	σ_y/MPa	σ_u/MPa	σ_R/MPa
216291 ± 4620	865.9 ± 18.4	1020.6 ± 14.2	823.6 ± 30.1

The Poisson ratio was not measured. For most metals $\nu = 0.3$ is a “good” choice.

B.2 Fatigue Tests

B.2.1 Damage Constants in VLCF

The damage constants were measured in strain driven VLCF tests. In strain driven tests, often problems with the controlling of the pulser appear (see Fig. B.2). Nevertheless this test is recommended, because of the homogeneous material deterioration.

Because of the controlling problems of the pulser, only the effective Young’s modulus in tension (unloading) are used for analysis. A decreasing of the Young’s modulus is observed after $p_D = 21$ ($p_D = \sum_{i=1}^{N_0} 2\Delta\varepsilon_i^p$). The damage constant is determined as the slope of the $p \Leftrightarrow D$ -diagram (Fig. B.3).

Figure B.2: Strain driven VLCF test. $\Delta\varepsilon = 1.2\%$, $N_B = 1744$, $f = 0.2Hz$.

Figure B.3: Determination of the damage constants in a VLCF test.

B.2.2 Fatigue Tests for Different Shapes

specimen	σ_n/MPa	HRB	N
1A	488	313	144497
34A	488	302	278186
26C	488	302	321487
4A	488	306	swr
26B	477	295	177581
18C	477	313	swr
5C	477	302	swr
4C	477	310	swr

specimen	σ_n/MPa	HRB	N_B
17B	636.36	313	17408
5A	636.36	306	20616
25A	636.36	306	29087
9C	636.36	302	35496
9A	636.36	310	36259
7B	590.91	302	43347
34C	590.91	298	48518
34B	590.91	302	56416
4C	590.91	310	74427
20B	545.45	298	83592
28C	545.45	306	85972
15C	545.45	310	98577
9B	545.45	302	101683
13A	545.45	317	111388
10A	500	306	168576
26A	500	306	195857
8C	500	306	200467
40A	500	295	217480
3C	500	302	236215
11A	500	310	311026

Left table: Determination of the fatigue limit. *swr*: specimen without rupture during $N = 2 \cdot 10^6$ cycles. $\sigma_f = 484MPa$ for 50% crack probability.

Right table: Lifetime test for smooth specimens.

specimen	σ_n/MPa	HRB	N_B
27B	500	306	15520
27C	500	310	15547
44B	454.55	313	23154
3B	454.55	310	25145
27A	454.55	306	31130
1C	409.09	302	40616
2A	409.09	310	47497
1B	409.09	306	49592
43A	409.09	306	64925
28A	363.64	310	75501
24A	363.64	313	90659
36B	363.64	313	108924
3A	363.64	310	129360
6C	318.18	310	145825
39B	318.18	295	156008
35B	318.18	302	184139
35C	318.18	313	599027

specimen	σ_n/MPa	HRB	N_B
33C	545.45	302	17154
8B	545.45	302	17932
31C	545.45	295	19962
38C	545.45	302	20112
44C	545.45	310	23550
32C	500	302	30153
28B	500	302	35775
15A	500	306	37803
12A	500	295	38136
38A	409.09	306	104334
22A	409.09	306	104473
19C	409.09	302	109463
35B	409.09	302	116456
36C	409.09	302	124425
25B	363.64	302	138163
39C	363.64	295	162100
32A	363.64	302	211982
39A	363.64	292	255680
38B	363.64	302	260254
35A	340.91	306	208032
32B	340.91	302	294884
22B	340.91	310	299059
33C	340.91	302	1478323

Left table: Lifetime tests for circularly notched specimens ($r = 9mm$).

Right table: Lifetime tests for statically optimized specimens.

B.3 Photoelastic Pictures

a.)

b.)

c.)

d.)

Figure B.4: Circularly notched part in a.) beginning b.) at the end of the experiment. Statically optimized part c.) in the beginning d.) at the end of the experiment. Load in both cases: $\sigma_n = 454.54MPa$.

Bibliography

- [1] AXELSSON, O. & BARKER, V. A.: *Finite element solution of boundary value problems, theory and computation*. Academic Press, (1984).
- [2] AINSWORTH, M., ZHU, J. Z., CRAIG, A. W. & ZIENKIEWICZ, O. C.: *Analysis of the Zienkiewicz-Zhu a-posteriori error estimator in the finite element method*. Int. Journal for Numerical Methods in Engineering, Vol. 28, pp 2161-2174, (1989).
- [3] ARORA, J. S.: *Introduction to optimum design*. McGraw-Hill, (1989).
- [4] BARREIT, R. & BERRY, M.: *Templates for the solution of linear systems: building blocks for iterative methods*. National Foundation DARPA and others, Internet document, available at: cs.utk.edu (1994).
- [5] BABUSKA, I. & RHEINBOLD, W. C.: *A posteriori error estimates for the finite element method*. Int. J. Numerical Methods in Eng., Vol. 12., pp. 1597-1615, (1978).
- [6] BABUSKA, I., JERINA, K., LI, Y. & SMITH, P.: *Quantitative assessment of the accuracy of constitutive laws for plasticity with an emphasis on cyclic deformation*. MD-Vol. 43/AMD-Vol. 168, Material Estimation for Modern Constitutive Equations, ASME (1993).
- [7] BAIER, H. J.: *Optimization in structural dynamics with applications*. In: Optimization of Large Structural Systems, Vol.II, Ed.: G. I. N. Rozvany, NATO ASI Series, Vol 231, (1993).
- [8] BAUD, R. V.: *Filletprofiles for constant stress*. Product Engng. Bd. 5, No. 4, pp. 133-34, (1934).
- [9] BENALLAL, A.,BILLARDON; R: and DOGHRI, I.: An integration algorithm and the corresponding consistent tangent operator for fully coupled elastoplastic and damage equations. Comm. Appl. Numer. Methods 4, pp. 731-740, (1988).
- [10] BENDSOE, M. P.: *Methods for the Optimization of Structural Topology, Shape and Material*. Springer-Verlag, Berlin, (1995).
- [11] BENDSOE, M. P.: *Composite materials as a basis for generating optimal topologies in shape design*. In: Structural Optimization, Eds.: G. I. N. Rozvany and B. L. Karihaloo, Proceedings of the IUTAM Symposium on structural Optimization, Melbourne, Australia, 9-13 February 1988,pp. 31-37, (1988).

- [12] BENNET, J. A. & BOTKIN, M. E.: *Structural shape optimization with geometric description and adaptive mesh refinement*. AIAA-Journal, VOL. 23(3), pp. 458-464, (1985).
- [13] BLETZINGER, K. U.: *Formoptimierung von Flächentragwerken*. Dissertation Universität Stuttgart, 1990.
- [14] BÖHM, W., Farin, G. & Kahmann, J.: *A survey of curve and surface methods in CAGD*. In: Comp. Aided Geom. Design 1, pp. 1-60, (1984).
- [15] BÖHM J.: *Zur Vorhersage von Dauerschwingfestigkeiten ungekerbter und gekerbter Bauteile unter Berücksichtigung des statistischen Grösseneinflusses*. Dissertation TUMünchen, (1980).
- [16] BÜSSENSCHÜTT, A. & WECK, M.: *Application of basic shape concept to practical shape optimization problems*. In: Proceedings of the First World Congress of Structural and Multidisciplinary Optimization. Eds. G.I.N. Rozvany and N. Ohlhoff, Pergamon Press, Oxford (1995).
- [17] CARMINE, R.: *Ein Kopplungsverfahren von FEM und BEM zur Berechnung ebener Spannungskonzentrationsprobleme*. Dissertation UNI Karlsruhe, (1989).
- [18] CHABOCHE, J.-L.: *Une Loi Différentielle D'Endommagement de Fatigue avec Cumulation non Linéaire*. Revue Française de Mécanique, (1974).
- [19] CHENG, G. & Fu, B.: *Shape optimization of continuum with crack*. In: Structural Optimization, Eds.: G. I. N. Rozvany and B. L. Karihaloo, Proceedings of the IUTAM Symposium on structural Optimization, Melbourne, Australia, 9-13 February 1988, pp. 57-62, (1988).
- [20] CHOW C. L. & WEI, Y.: *Model of continuum damage mechanics for fatigue failure*. Int. J. Frac., VOL. 50, n 4, pp 301-316, (1991).
- [21] CHOW, C. L. & WEI, Y.: *A damage mechanics model of fatigue crack initiation in notched plates*. Theoretical and applied Fracture Mechanics 16, pp 123-133, (1991).
- [22] DENGEL, D.: *Planung und Auswertung von Dauerschwingversuchen bei angestrebter Absicherung der Kennwerte*. In: Verhalten von Stahl bei schwingender Beanspruchung, Ed.: W. Dahl, Verlag Stahleisen m. b. H. Düsseldorf (1978).
- [23] *DUBBEL - Taschenbuch für den Maschinenbau*. Eds.: W. Beitz und K.-H. Küttner, 16. Auflage, Springer Verlag Berlin Heidelberg New York London Paris Tokyo, (1987).
- [24] EIFLER, D.: *Inhomogene Deformationserscheinungen bei Schwingbeanspruchungen eines unterschiedlich wärmebehandelten Stahl des Typs 42 CrMo 4*. Dissertation UNI Karlsruhe, (1981).
- [25] ESCHENAUER, H. A. & THIERAUF, G.: *Discretization methods and structural optimization- procedures and application*. Proceedings of GAMM Seminar, 5.-7.Oct, Siegen, (1988).

- [26] ESCHENAUER, H., A., KOSKI, J. & OSYCKA, A.: *Multicriteria design optimization*. Springer Verlag, (1991).
- [27] ESCHENAUER, H., A. & WEINERT, M.: *Structural optimization techniques as a mathematical tool for finding optimal shapes of complex shell structures*. In: *Non smooth optimization-methods and Application*, Ed.: Giannessi, Gordon and Breach Science Pub., Switzerland, (1992).
- [28] ESPING, B.: *Design optimization as an engineering tool*. In: *Structural Optimization*, Ed.: G. Rozvany, VOL. 10 3/4, (1995).
- [29] ERIKSSON, M.: *Optimization studies on the Volvo 850 front floor*. M. Sc. Thesis at School of Mechanical Engineering, Chalmers Institut of Technology Gothenburg, (1992).
- [30] FANNI M., SCHNACK E.& GRUNWALD J.: *Lifetime maximization through shape optimization of dynamically loaded machine parts*. *Int. J. for Eng. Analysis and Design*, VOL.1, pp. 25-41, (1994).
- [31] FANNI M.: *Formoptimierung dynamisch belasteter Bauteile*. Dissertation UNI Karlsruhe, (1993).
- [32] FARIN, G.: *Curves and surfaces for computer aided geometric design*. 3rd Edition, Academic Press Inc., (1993).
- [33] FORST, N. K., Marsch, K. J. & L.P. POOK: *Metal fatigue*. Oxford (1974).
- [34] FLEURY, C. & BRAIBANT, V: *Structural optimization - a new dual method using mixed variables*. In: *Int. J. Num. Meth. Eng.*, 23, pp. 409-428, (1986).
- [35] FRANCAVILLA, A., RAMACRISHNAN, C. V. & ZIENKIEWICZ, O. C.: *Optimization of shape to minimize stress concentration*. *J. Stress Analysis*, VOL. 10, No. 2, (1975).
- [36] GRUNWALD, J. & SCHNACK, E.: *Models for shape optimization of dynamically loaded machine parts*. *Proceedings of the 1st World Congress in Structural and Multidisciplinary Optimization*, 29.05.-2.06.1995 Goslar (Germany).
- [37] GRUNWALD, J. & SCHNACK, E.: *A fatigue model for shape optimization*. In: *Structural Optimization*, to appear.
- [38] HAFTKA, R. T.: *Structural Shape Optimization*. *Comp. Meth. and Eng.* 57, pp. 91-106, (1986).
- [39] HAFTKA, R. T., GÜRDAL, Z. & KAMAT, M. P.: *Elements of structural optimization*. Dordrecht, Boston, London: Kluwer Academic Publishers, 2nd Edition, (1990).
- [40] HAFTKA, R. T. & GRANDI, R. V.: *Structural shape optimization - a survey*. *Computer methods in applied mechanics and engineering*, VOL. 57, pp. 91-106, (1986).

- [41] HAHN, H. G.: *Methode der finiten Elemente*. Akademische Verlagsgesellschaft Wiesbaden, 2. Auflage, (1975).
- [42] HECKEL, K.: *Wirkung von Kerben bei schwingender Beanspruchung*. In: Verhalten von Stahl bei schwingender Beanspruchung, Ed.: W. Dahl, Verlag Stahleisen m. b. H. Düsseldorf (1978).
- [43] HERZIG, T.: Ein paralleles 3D-Randelementprogramm der Elastostatik für heterogene Rechnerarchitekturen. Dissertation Uni-Karlsruhe (1994).
- [44] HUBER, B.: *Untersuchungen zur Beschleunigung eines Optimierungsverfahrens auf der Basis der Sequentiellen Quadratischen Programmierung*. Diplomarbeit am Institut für technische Mechanik/Festigkeitslehre, Uni Karlsruhe, (1995).
- [45] IANCU, G.: *Spannungskonzentrationsminimierung dreidimensionaler elastischer Kontinua mit der FEM*. Dissertation Universität Karlsruhe, (1990).
- [46] JAECKELS, H.: *Ein probabilistisches Lebensdauermodell für hochbelastete Bauteile*. Forschungsberichte/Reihe 18, Mechnik/Bruchmechanik, VDI-Verlag (1992).
- [47] JIN, H. & WINBERG, N. E.: *Two dimensional mesh generation, adaptive meshing and refinement*. Intern. J. Num. Meth. Eng., Vol. 29, pp. 325-331, (1990).
- [48] KACHANOV, L. M.: *On creep rupture time*. Izv. Acad. Nauk SSSR, Otd. Techn. Nauk, No. 8, pp. 26-31, (1958).
- [49] KACHANOV, L. M.: *Introduction to continuum damage mechanics*. Martinus Nijhoff Dordrecht, The Netherlands, (1986).
- [50] KINCAID, D., R. & OPPE, T.: *Recent vectorization and parallelization of itpack V*. In: Preconditioned Conjugate Gradient Methods, Eds: O. Axelsson & L. Yu. Kolotilina, Springer Verlag, Proceedings Nijmegen 19-21 June, (1989).
- [51] KLESNIL, M., LUKAS, P. & POLAK, J.: *General features of the fatigue process*. In: Cyclic Deformation and Fatigue of Metals, Ed: Matej Bílý, Elsevier Amsterdam-London-New-York-Tokyo (1993).
- [52] KNEPPE, G.: *Direkte Lösungsstrategien zur Gestaltoptimierung von Flächentragwerken*. Dissertation Uni Siegen, VDI-Verlag Düsseldorf, (1986).
- [53] KUHN, H. E. & TUCKER, A. W.: *Nonlinear programming*. In: Neyman, J. (Ed.): Proceedings of the 2nd Berkeley Symposium on Mathematical Statistics and Probability. University of California, pp. 481-492, Berkely, (1951).
- [54] LOCHER, F.: *Einführung in die numerische Mathematik*. Wissenschaftliche Buchgesellschaft Darmstadt, (1978).
- [55] LEMAITRE, J. & DOGHRI, I.: *Damage 90: A postprocessor for crack initiation*. Computer Methods in Applied Mechanics and Engineering, VOL. 115, n 3-4, pp. 197-232, (1994).

- [56] LEMAITRE, J.: *A course on damage mechanics*. Springer Verlag Berlin Heidelberg New York (1992).
- [57] LEMAITRE, J. & CHABOCHE, J.-L.: *Mechanics of solid materials*. Cambridge University Press (1990).
- [58] LEMAITRE, J. & MARQUIS, D.: *Modeling complex behavior of metals by "state-kinetic coupling theory"*. Journal of Engineering Materials and Technology, VOL. 114, pp. 250-254, (1992).
- [59] MACHERAUCH, E. & REICK, W.: *Auswirkungen von Gefüge, Fertigung und Beanspruchung auf das Dauerschwingverhalten*. In: Verhalten von Stahl bei schwingender Beanspruchung, Ed: W. Dahl, Verlag Stahleisen m. b. H. Düsseldorf (1978).
- [60] MACHERAUCH, E.: *Praktikum in Werkstoffkunde*. 10. Auflage, Vieweg Verlag, (1991).
- [61] MAGISTER, R. & POST, P. U.: *Use of structural optimization in the development of pneumatic components*. In: Proceedings of the First World Congress of Structural and Multidisciplinary Optimization. Eds. G.I.N. Rozvany and N. Ohlhoff, Pergamon Press, Oxford (1995).
- [62] MARTIKKA, H.: *Optimum design of locomotive frames using fuzzy goals and FE methods*. In: Structural Optimization, Eds.: S. Hernandez, M. El-Sayed, C.A. Brebbia, Computer aided Optimum Design of Structures IV, Proceedings of OPTI '95, pp. 145-152, (1995).
- [63] MATHIAK, G. & SCHNACK, E.: *An appropriate design model for 3D shape optimization of linear elastic structures*. In: Optimization of Structural Systems and Applications, Ed.: C. A. Brebbia & S. Hernandez, Elsevier Applied Science, London, (1993).
- [64] MATTHECK, C.: *Why they grow, how they grow - the mechanics of trees*. In: Arboricultural Journal 14, pp. 1-17, (1990).
- [65] MAYR, P.: *Grundlagen zum Verhalten bei schwingender Beanspruchung*. In: Verhalten von Stahl bei schwingender Beanspruchung, Ed.: W. Dahl, Verlag Stahleisen m. b. H. Düsseldorf (1978).
- [66] NEUBER, H.: *Theoretical determination of fatigue strength at stress concentration*. Technical Report AFML-TR-68-20, (1968).
- [67] NEUBER, H.: *Der zugbeanspruchte Flachstab mit optimalen Querschnittsbergang*. Rorsch. Ing. Wesen, Bd. 35, Nr. 1, pp.29, (1969).
- [68] NEUBER, H.: *Kerbspannungslehre*. Springer-Verlag, Berlin Heidelberg New York Tokyo, 3. Auflage, (1985).
- [69] NEUMAIER, T.: *Numerische und experimentelle Untersuchungen zur Kerbformoptimierung an Proben aus 30CrNiMo8*. Diplomarbeit am Institut für Technische Mechanik/Festigkeitslehre, Uni Karlsruhe, (1995).

- [70] ORITZ, M. & POPOV, E. P.: *Accuracy and stability of integration algorithms for elastoplastic constitutive equations*. Int. J. Numer. Methods Engrg. 21, pp. 1561-1576, (1985).
- [71] PEDERSEN, P. & LAURSEN, C. L.: *Design for minimum stress concentration by finite element and linear programming*. In: J. of Structural Materials, Vol. 10, No. 4, pp. 375-391, (1983).
- [72] PROFFEN, R.: *Substrukturtechniken für schnelle und genaue Damageanalysen in der Formoptimierung*. Diplomarbeit am Institut für technische Mechanik/Festigkeitslehre, Uni Karlsruhe, (1995).
- [73] RAMM, E. & MAUTE, K.: *Adaptive topology optimization*. In: Structural Optimization, Ed.: G. Rozvany, VOL. 10, pp. 100-112, (1995).
- [74] RANK, E. & ZIENKIEWICZ, O. C.: *A simple error estimator for the finite element method*. Communications in Applied Numerical Mechanics, Vol. 3, pp. 243-250, (1987).
- [75] RASSMUSSEN, J.: *Development of the interactive shape optimization system*. CISM Course on Shape and Layout Optimization of Structural Systems, Udine 16-20 July, (1990).
- [76] RICE, R. C.: *Fatigue design handbook*. Eds.: R. C. Rice, B. N. Leis and D. V. Nelson, Published by: Society of Automotive Engineers, Inc. second edition, (1988).
- [77] ROZVANY, G.I.N., ZHOU, M., BIRKER, T.: *Generalized shape optimization without homogenization*. Structural Optimization, Ed.: G.I.N. Rozvany, Vol. 4, pp. 250-252.
- [78] SAUTER, J.: *A new optimisation method modelled on biological structures*. In: Benchmark, Sept. (1993).
- [79] SCHITTKOWSKI, K.: *NLPQL A fortran subroutine solving constrained nonlinear programming problems*. Annals of Operation Research, 5, 485-500, (1985/86).
- [80] SCHITTKOWSKI, K.: *On the convergence of sequential quadratic programming: a method with an augmented lagrangian line search function*. Math. Operationsforschung u. Statistic; Ser. Optimization Vol. 14, No. 2, pp. 197-216, (1983).
- [81] SCHITTKOWSKI, K.: *The nonlinear programming method of Wilson, Han and Powell with an augmented Lagrangian type line search function, Part 1: Convergence analysis; Part 2: An efficient implementation with linear least squares subproblems*. Numerische Mathematik, Vol. 38, pp. 83-127, (1981).
- [82] SCHNACK E., SPÖRL U. & IANCU G.: *Gradientless shape optimization with FEM*. VDI Forschungsheft 647/88, (1988).
- [83] SCHNACK, E. & IANCU G.: *Shape design of elastostatic structures based on local perturbation analysis*, In: Structural Optimization, 1, 117-125, (1989).

- [84] SCHNACK, E. & SPÖRL, U.: *Oberflächenoptimierung ebener und rotationssymmetrischer elastischer Kontinua mit der FEM*. DFG-Report, (1983).
- [85] SCHNACK, E.: *Ein Iterationsverfahren zur Optimierung von Kerboberflächen*. VDI-Forschungsheft, No. 589, VDI Verlag Düsseldorf, (1978).
- [86] SCHNACK, E.: *Ein Iterationsverfahren zur Optimierung von Spannungskonzentrationen*. Habilitationsschrift, Universität Kaiserslautern, (1977).
- [87] SCHULZE, V.: *Die Auswirkungen kugelgestrahlter Randschichten auf das quasistatische sowie ein und zweistufige zyklische Verformungsverhalten von vergüteten 42 CrMo 4*. Dissertation UNI Karlsruhe, (1993).
- [88] SCHWALBE K. H.: *Bruchmechanik metallischer Werkstoffe*. Carl Hanser Verlag München Wien, (1980).
- [89] SCHUMACHER, A. & ESCHENAUER, H.A.: *Simultaneous shape and layout optimization*. In: Proceedings of WCSMO-1 in Goslar, 28.05-2.06.1995. Ed: N. Olhoff and G.I.N. Rozvany, Pergamon Press 1995.
- [90] SVANBERG, K.: *The method of moving asymptotes - a new method for structural optimization*. In: Int. J. Num. Meth. Engng., Vol. 24, pp. 359-373, (1987).
- [91] TAYLOR, G. I.: *Plastic strain in metals*. J. Inst. Met., pp. 62-307, (1938).
- [92] TEMPLEMAN A. B.: *Entropy-based minimax application in shape-optimal design*. In: (Eds.) Eschenauer, Thierauf: Discretisation methods and structural optimization - procedures and applications, Springer Verlag (1988).
- [93] TENCHEV, R. & SCHNACK, E.: *Material damage propagation and mesh dependence in finite element analyses - case studies*. Preprint 95-4, Institute of Solid Mechanics, Karlsruhe University, (1995).
- [94] WANG, J.: *A continuum damage mechanics model for low-cycle fatigue of metals*. Engineering Fracture Mechanics, Vol. 4, No. 3, pp. 437-441, (1992).
- [95] WANG, J.: *Low cycle fatigue and cycle dependent creep with continuum damage mechanics*. International Journal of Damage Mechanics, Vol. 1, April (1992).
- [96] WIEGHARDT, K.: *Ein Konzept zur interaktiven Formoptimierung kontinuierlicher Strukturen*. Dissertation man Institut für konstruktiven Ingenieurbau, Ruhr Universität Bochum, Mitteilungen Nr. 95-3, (1995).
- [97] WOLF, H.: *Spannungsoptik*. Springer-Verlag, 2. Auflage, (1976).
- [98] ZANDMAN, F., REDNER, S. & DALLY, J. W.: *Photoelastic coatings*. The Iowa State University Press Ames, Iowa and Society for Experimental Stress Analysis Westport, Connecticut (1977).
- [99] ZIEGLER, H.: *Some extremum principles in irreversible thermodynamics*. Progress in Solid Mechanics, Vol. IV, pp. 93-193, (1967).

- [100] ZIENKIEWICZ, O., C.& ZHU: *A simple error estimator and adaptive procedure for practical engineering analysis*. Int. Journal for Numerical Methods in Engineering, VOL. 24, pp. 337-357, (1987).